Skoltech

Skolkovo Institute of Science and Technology

Skolkovo Institute of Science and Technology

HYBRID FUNCTIONAL MATERIALS BASED ON SINGLE-WALLED CARBON NANOTUBES

Doctoral Thesis

by

MIKHAIL O. BULAVSKIY

DOCTORAL PROGRAM IN MATERIALS SCIENCE AND ENGINEERING

Supervisor:

Doctor of Science, Prof. Albert G. Nasibulin

Co-Supervisor:

PhD, Assistant Prof. Fedor S. Fedorov

Moscow – 2023

I hereby declare that the work presented in this thesis was carried out by myself at Skolkovo Institute of Science and Technology, Moscow, except where due acknowledgement is made, and has not been submitted for any other degree.

Mikhail O. Bulavskiy (Candidate)

Prof. Albert G. Nasibulin (Supervisor)

Assistant Prof. Fedor S. Fedorov (Co-Supervisor)

ABSTRACT

Single-walled carbon nanotubes (SWCNTs) is a unique material possessing a great combination of unique physical properties together with chemical stability and possibility to their subsequent functionalization. However, as-synthesized SWCNTs have found limited application due to simultaneous presence of both metallic and semiconducting nanotubes, agglomeration into bundles and presence of end-caps hindering access to internal channels. Hybrid SWCNT-based materials could become a solution overcoming these disadvantages. Namely, adsorption doping with electron donors/acceptors increases electrical conductivity due to the significant Fermi-level shift eliminating Schottky barriers and increasing the concentration of charge carriers. Deposition of conductive polymer possessing pseudocapacitance on SWCNT films could result into high-capacitance flexible material for energy storage in supercapacitors. Mild SWCNT end-cap removal could allow filler penetration into the SWCNT channels with high filling efficiency, ensuring hybrid material desired property.

We implemented these strategies of hybrid SWCNT films production for promising application as functional materials. First, we developed the bilateral SWCNT adsorption doping method with $HAuCl_4$ employing end-cap removal by thermal treatment at 300-400 ºC resulting in equivalent sheet resistance as low as 31 ± 4 Ω sq^{-1} for application as transparent conductive films.

Then, we examined the impact of electrochemical opening of SWCNT channels under cyclic voltammetry protocols onto SWCNT structure and its relation to the filling efficiency by varying treatment upper vertex potential (UVP). We revealed that structural defects introduced through electrochemical treatment follow 3 stages: (i) minor amount of defect along with inefficient opening (UVPs < 1.1 V $vs.$ RHE), (ii) trade-off between an efficient opening and moderate defects number (UVP = 1.1 V $vs.$ RHE), (iii) extensive SWCNT wall destruction (UVPs > 1.1 V $vs.$ RHE). Maximum filling efficiency ~1680 m cm^{-2} of gold nanowires length per unit film area was achieved for the second stage highlighting limiting behavior of structural defects on filling efficiency.

Eventually, we applied electrodeposition of polyaniline (PANI) onto free-standing SWCNT films. We showed that composites' energy storage performance depends on the self-discharge defined by cell configuration. In three-electrode cell (contact through SWCNTs) the highest capacitance retention is observed for thinner SWCNTs possessing higher sheet resistance resulting into gravimetric capacitance of 541 F g^{-1} for SWCNT95/PANI50 composite. In two-electrode cell (contact through PANI) self-discharge is determined by the conductivity of PANI and decreases with the deposited polymer layer thickness increase reaching 175 F g^{-1} for SWCNT90/PANI50 composite. Composites were tested as free-standing flexible symmetric supercapacitors showing good stability during cycling and bending.

Hybrid materials discussed provide an evidence that hybrid SWCNT-based materials significantly improve functional properties of SWCNTs bringing them closer to the application in real devices.

PUBLICATIONS AND AUTHOR CONTRIBUTION

1. A.E. Goldt, O.T. Zaremba, **M.O. Bulavskiy**, F.S. Fedorov, K. V. Larionov, A.P. Tsapenko, Z.I. Popov, P. Sorokin, A.S. Anisimov, H. Inani, J. Kotakoski, K. Mustonen, A.G. Nasibulin, Highly efficient bilateral doping of single-walled carbon nanotubes, J. Mater. Chem. C. 9 (2021) 4514–4521.

The author of the thesis has participated in the data collection related to doping of SWCNT films, characterization of the material and analysis of obtained results. Besides, the author contributed to evaluation of the doping mechanism and writing the original manuscript.

2. V. Panasenko*, **M.O. Bulavskiy***, A.A. Iurchenkova, Y. Aguilar-Martinez, F.S. Fedorov, E.O. Fedorovskaya, B. Mikladal, T. Kallio, A.G. Nasibulin, Flexible supercapacitors based on free-standing polyaniline/single-walled carbon nanotube films, J. Power Sources. 541 (2022) 231691. (* - equally contributed authors).

The most of the research was carried out by the author of the present thesis. The author took part in the characterization and analysis of the results. The author of the thesis contributed to writing the review and editing the manuscript.

3. **M.O. Bulavskiy**, F.S. Fedorov, A.G. Nasibulin, The Effect of Electrochemical Treatment on the Structure of Single-Walled Carbon Nanotubes: Towards Better Filling Efficiency, Submitted to the Surfaces and Interfaces journal.

The research was carried out mainly by the thesis author: conceptualization, methodology, investigation, formal analysis, visualization and writing the manuscript.

ACKNOWLEDGEMENT

I would like to give my sincere and infinite gratitude to my supervisor and head of Laboratory of Nanomaterials Prof. Albert Nasibulin and co-supervisor Prof. Fedor Fedorov for permanent support and assistance during the research, for driving me forwards in the moments of despair. I appreciate your believe in me and thank you for chance to share 4 years of my PhD study in the Laboratory of Nanomaterials. The experience I have got during PhD study cannot be overestimated.

I want to emphasize my exceptional gratitude to my family for mental support. To my mother always believing in my success; to my father discussing thesis research results during numerous nights; to my sister motivating me always move forwards. And especially to my bride, going along with me through all the challenges and difficulties, and inspiring my self-confidence.

I highly appreciate Prof. Dmitry Krasnikov for sharing his enormous experience and Dr. Anastasia Goldt who expanded my knowledge; Dr. Artem Grebenko for blending me into the workflow in the laboratory; Aram, Hassaan, Mikhail, Ignat, Nikita and Javier for making these 4 years of PhD memorable, becoming my second family; Konstantin for teaching me Python that made my data processing effective; and Ayvaz who was working in the laboratory shoulder to shoulder with me at nights. I thank all the members of Laboratory of Nanomaterials for their advices and warm atmosphere in the laboratory.

Additionally, I want to thank all the co-authors of publications for their contribution to the research that forms the basis of this thesis.

TABLE OF CONTENTS

ABBREVIATIONS

BE – binding energy

CNT – carbon nanotube

CP – conducting polymer

CV – cyclic voltammetry

CVD – chemical vapor deposition

DFT – density functional theory

DOS – density of states

EDL – electrical double layer

f-SWCNT – filled single-walled carbon nanotubes

ITO – indium-tin oxide

NWs – nanowires

OCFGs – oxygen containing functional groups

OCP – open-circuit potential

PANI – polyaniline

PANI40 – composites synthesized using 40 deposition cycles

PANI50 – composites synthesized using 50 deposition cycles

PANI60 – composites synthesized using 60 deposition cycles

PANI70 – composites synthesized using 70 deposition cycles

PDMS – poly(dimethylsiloxane)

PMMA – poly(methylmethacrylate)

RBM – radial-breathing mode

RHE – reversible hydrogen electrode

SC – supercapacitor

SEM – scanning electron microscopy

SHE – standard hydrogen electrode

STEM – scanning transmission electron microscopy

SWCNT – single-walled carbon nanotube

SWCNT-DH – SWCNT state after densification and subsequent heating in vacuum

SWCNT-EH – SWCNT state after electrochemical treatment and subsequent heating in vacuum

SWCNT-woFe – iron-free SWCNT film

SWCNT80 – SWCNT films with the transmittance of 80 % at 550 nm

SWCNT90 – SWCNT films with the transmittance of 90 % at 550 nm

SWCNT95 – SWCNT films with the transmittance of 95 % at 550 nm

TEM – transmission electron microscopy

UVP – upper vertex potential

UV-Vis-NIR – ultraviolet-visible-near infrared spectrophotometry

vHs – van Hove singularities

XPS – X-ray photoelectron spectroscopy

INTRODUCTION

Relevance and background of the research topic

Since the moment of the first visual evidence in 1993, single-walled carbon nanotubes (SWCNTs) have been thoroughly studied for 30 years. To these days, comprehensive data of different aspects of SWCNTs physical and chemical properties have been collected by the scientific community on pair with methods of synthesis, purification and separation, and also promising applications[1]. Nevertheless, SWCNTs are still far from the widespread industrial applications. One of its main reasons are the limitations stemming from the nature of the bulk SWCNT material properties.

In particular, during the synthesis a combination of different chiralities of SWCNTs grow simultaneously, resulting in the mixture of SWCNTs possessing semiconducting and metallic type electrical conductivity [2]. In such mixture Schottky barriers forms at the junction of semiconducting and metallic SWCNTs, providing the material with neither purely semiconducting nor metallic properties [3]. It limits their application in fields requiring each of these properties individually (transparent conductive films, transistors). Besides this, agglomeration of SWCNTs into bundles during their synthesis emerging from extreme energy of lateral interaction spoils optoelectrical performance and thermal conductivity of the bulk material when compared to the single SWCNT. It also constrains utilization in such applications as single photon emitters requiring individual nanotubes. In addition, SWCNTs have end-caps that hinder accessibility to the nanotube channel. However, when accessible, these channels could be used as a scaffold for the filling with substances bringing properties that are abnormal for SWCNTs (magnetic, catalytic, *etc.*) [4]. Therefore, modification of the SWCNT-based bulk materials could become an opportunity to improve their properties to overcome challenges on the way to applications [5].

Scientific community proposed and developed various approaches to SWCNT modification that brings unique properties to hybrids driving nanotubes closer to the widespread application [1,5–7]. First, SWCNTs' surface can be chemically modified with various functional groups. This approach mainly addresses disadvantages caused by bundling and may improve SWCNT dispersibility and change their electrical properties. The second approach relies on using SWCNT surface as a substrate for coating with foreign materials. In this case coating brings the desired property to the hybrid without significant changes of intrinsic SWCNT properties, *e.g.* nano-sized catalyst distributed on the SWCNT surface or functional polymer coating of the SWCNTs surface. The third approach is based on the substitution of carbon atoms in the SWCNT structure with heteroatoms, so that heterogeneous nanotubes are formed. Such structural changes significantly alter electronic properties of pristine SWCNT, and may even result in the improved electrocatalytic activity. Next, SWCNT modification approach includes adsorption

doping with electron donor/acceptor materials that reside on the surface (and/or inside SWCNT bundles), although does not form the individual phase. The application such substances significantly improves electronic conductivity of SWCNT-based material. Eventually, filling of SWCNT channels is the most versatile method in terms of resulting hybrid material properties. Hybrid filled SWCNTs may exhibit properties allowing application in nanoelectronics (electronic properties) [1,8–10], data storage (magnetic properties) [11–13], catalysis [14], supercapacitors [15,16], sensors [17] and functional materials in many other areas depending on the filler agent inserted [1].

Applications of SWCNT-based hybrid materials are extremely diverse, hence extensive research has been done to apply them in various fields. For instance, application of SWCNTs in transparent conductive films (TCFs) were thoroughly elaborated in the Laboratory of Nanomaterials of Skolkovo Institute of Science and Technology including synthesis optimization, application of rational design approach, morphology alteration and adsorption doping modification [18–21]. However, the optoelectrical performance are far from ITO that is the commonly used transparent conductor. The efficiency of SWCNT film modification for TCFs still requires improvement. SWCNTs have also been studied as a material for supercapacitors owing to their high specific surface area, but their application is limited by moderate gravimetric capacitance of the material. Hybrid material based on free-standing SWCNT thin film covered with polymers exhibiting pseudocapacitive behavior is a promising alternative that may outperform SWCNTs in terms of the energy stored, while preserving its flexibility for application as a wearable electronics power source. Filling of SWCNTs being one of the most versatile SWCNT modification methods could be significantly hindered by nanotube structural defects [4,22–26]. Disadvantage of conventional SWCNT end-cap removal methods is a formation of multiple wall structural defects during the opening [27–30]. The promising alternative is a controllable electrochemical approach, although is still requires investigation including evaluation of filling efficiency dependence on amount of SWCNT structural changes.

Aim and Objectives

Aim of the thesis research was to investigate scientific foundations for the development of modification protocols of the SWCNT thin films (to be applied in transparent conducting films and as supercapacitors), establish influence of electrochemical treatment on SWCNT structure and filling efficiency, and study obtained materials properties. In order to achieve this aim, the following **objectives** were established:

- To develop a method of bilateral SWCNT film doping with $HAuCl_4$, evaluate efficiency of hybrid material as transparent conductive films and explore its origin.

- To develop the controllable SWCNT electrochemical opening approach and investigate SWCNT structural changes in response to treatment conditions.
- To evaluate filling efficiency of the electrochemically opened SWCNTs using solution filling approach.
- To investigate impact of free-standing SWCNT film thickness and polymer deposition duration on properties of SWCNT/polyaniline composites.
- Evaluate the performance of supercapacitors made of flexible SWCNT/polyaniline composites in three- and two-electrode configuration.

Scientific novelty

In the thesis research we developed a novel and simple method of highly efficient bilateral doping of SWCNT films for optoelectronic properties modification for application of resulting modified SWCNT films as transparent conductive films. The proposed method includes a thermal treatment of SWCNT films for the nanotube caps' opening at optimal temperatures of 300–400 ºC followed by doping with $HAuCl_4$ ethanol solution, thus, providing a feasible penetration of the dopant solution into the inner SWCNT cavity. The application of the proposed method allowed us to obtain transparent conductive SWCNT films with a record equivalent sheet resistance value of $31 \pm 4 \ \Omega \ sq^{-1}$. This value was achieved due to the significant Fermi-level downshift in the case of simultaneous doping from outside and inside of the nanotube confirming stronger doping in comparison to pristine tubes with closed ends. The more significant Fermi-level downshift of cap-opened SWCNTs in comparison to the pristine is confirmed by the open-circuit potential measurements and DFT calculations.

We examined the internal SWCNT channels filling efficiency and its relation with the SWCNT structure changed in the response to the UVP of electrochemical oxidative treatment. Based on cyclic voltammograms and structure evaluation methods applied we conclude that the formation of structural defects introduced through electrochemical treatment formally follows 3 stages. The first stage is characterized by minor amount of wall defect formation along with inefficient end-cap removal and correspond to the electrochemical oxidative treatment at UVPs < 1.1 V *vs.* RHE. As a result, SWCNTs accommodate moderate number of encapsulated NWs, although most of them are shorter than ~30 nm. At the second stage we observe a trade-off between an efficient opening of internal SWCNT channels with moderate level of SWCNT wall defects that happens when UVP = 1.1 V *vs.* RHE is applied. It results into the highest achieved areal density of encapsulated NWs with the greatest average NW length. Therefore, at such conditions SWCNT film demonstrated maximum filling efficiency ~1680 m cm^{-2} of gold nanowires length per unit area of ~87 % transmittance SWCNT film, that is ~10 times higher than filling efficiency of reference sample. The third stage is distinguished by extensive SWCNT wall

destruction due to electrochemical treatment at UVPs > 1.1 V *vs.* RHE, leading to the least efficient filling of SWCNTs approaching that of untreated reference sample.

We examined composite materials based on free-standing transparent SWCNT films and PANI deposited by electrochemical polymerization. We established that weight of the composite material increases linearly with decreasing the SWCNT film transmittance in range from 95 % to 80 % and with increasing the number of deposition cycles in the range from 40 to 70 cycles of polymer electrodeposition. We established SWCNT film thickness effect: the thicker film, the more amorphous and disordered polymer is deposited, even with a small number of deposition cycles. The specific gravimetric capacitance increases as the transmittance of SWCNT film ranges in a row of 80 %, 90 %, and 95 %. The maximum gravimetric capacitance is 541 F g^{-1}, and it has been reached with 50 PANI deposition cycles for SWCNTs with a transmittance of 95 % when a three-electrode cell was used. The films based on SWCNT80 and SWCNT90 show the highest specific capacitance measured in the two-electrode cell reaching values of 130 and 175 F g^{-1}, respectively. Maximum values of specific energy (7 W h kg^{-1}) and specific power (1700–1800 W kg^{-1}) are reached for 80 % transmittance SWCNT template with no dependency on PANI deposition cycle number. The self-discharge process was investigated in two- and three-electrode setups with different cell architectures. In a three-electrode cell, when contact with an electrode is made through SWCNT film, self-discharge is determined by the conductivity of the SWCNT films and decreases with the transmittance increase. In a two-electrode cell, with contact through the PANI layer, self-discharge is determined by the conductivity of the polymer and decreases with an increase of the deposited polymer layer thickness. The difference in the self-discharge mechanism explains the difference in capacity for the different cell architectures applied in research. Synthesized SWCNT composites were tested as free-standing flexible symmetric supercapacitors showing good stability during cycling and bending.

CHAPTER 1. LITERATURE REVIEW

1.1. Methods of synthesis and fabrication of hybrid materials based on SWCNTs

1.1.1. Approaches to filling of SWCNTs

Filled carbon nanotubes are hybrid nanostructures considered to be next generation materials, combining intrinsic properties of host carbon nanotubes with those of encapsulated material [5,7,31]. Since the first reported evidence of multi-walled carbon nanotube internal channel filling in 1993, this topic underwent extensive research [32]. In the case of SWCNTs, it took some time and effort to report the first filling empathizing challenges to synthesize such hybrid materials [33,34]. Over last two decades, vast scope of research was done to develop the SWCNT filling protocols, to investigate their properties, and explore the potential applications [1,6].

Methods of the SWCNT filling are primarily classified into two main groups: *in situ*, *i.e.*, during the nanotube synthesis and post growth *ex situ* filling. The *in situ* methods have an advantage of being one-step process, although only scarce evidence of simultaneous SWCNT synthesis and filling are reported up to now [35,36]. In contrast, the *ex situ* filling usually requires an extra step of opening SWCNT end-caps allowing penetration of a filler material into nanotube's internal channels. Nevertheless, it opens an opportunity to broaden the filler nature to extensive list of organic or inorganic molecules, metal oxides, salts, *etc*. This strong advantage makes the *ex situ* approach rather widespread and commonly used [5,8].

Furthermore, the *ex situ* filling approach can be sub-divided into gas, melt, and solution filling techniques. Although gas and melt filling methods allow high filling efficiency, the list of the filler substances is limited by several factors. Namely, the filler material vaporization/sublimation/melting must happen without decomposition, filling temperatures must be lower than for SWCNT sealing (1000-1200 ºC), and the fillers are to have high vapor pressures or moderate melt surface tension (< 130-170 mN m^{-1}) [5,37]. The alternative solution method is based on the capillary filling of a SWCNT with a solution of the desired substance or its precursor. Since the most solvents have surface tension not exceeding 80 mN m^{-1} then solution filling does not have strict limitations, but the solubility of the filler. Therefore, appropriate selection of the solvent might cover a wide range of the filler substances. The main disadvantage of the solution filling method is the low filling efficiency [5].

The significance of SWCNT structure, particularly functional groups and defects, for liquid penetration into internal channels has been recently highlighted on the basis of molecular dynamics simulations [22–24]. It was shown that structurally perfect and hydrophobic SWCNT channel experience spontaneous imbibition. In particular, water forms a depletion region of low density next to the nanotube wall, where the fluid propagation velocity jump takes place resulting into the high total flow through the

channel. In addition, there is a radial velocity inside of the nanotube directed to the wall that results in the denser water layer neighboring the depletion layer. The structural defects such as channel surface roughness lead to the dramatic decrease of the velocity jump, so that mass flow rate decreases ~2.5 orders of magnitude [23]. In case of the wetting with nonpolar liquid such as decane, the fluid flows through the SWCNT cavity in the potential well close to the wall [24]. So that, disruption of the tube wall would hinder the flow of nonpolar liquids, too. Surprisingly, it was reported that the SWCNT wall opening behaves as a barrier for liquid flow [24] that manifests in the density depletion at such kind of defects [22]. Besides this, oxygen-containing functional groups in the SWCNT structure tend to form hydrogen bonds with liquids [25], while -OH bond specific orientation in the depletion layer plays a governing role in a high liquid flow rate within the nanotube's cavity. Thus, the hydrophobicity and smoothness of the SWCNT channel should be preserved for the efficient SWCNT filling with liquids [23,26], emphasizing importance of structure and surface chemistry control during the opening process [4].

1.1.2. Deposition of PANI onto SWCNTs

CNT/PANI composites are shown to possess both high specific capacitance and power values on top of good cyclic stability [38–40]. There are various methods to synthesize such composites: interphase [41] and single-phase [38,42] chemical synthesis, plasma-induced vapor deposition [43], and electrodeposition [39,44]. However, SCs prepared by interphase and single-phase chemical synthesis still need to employ a binder for electrode fabrication that results in a lower power density of SC [45,46] and often poor mechanical properties [47]. Recent studies indicate the development of flexible SWCNT/PANI composite materials [44,47]. This type of composite material promises good capacitance (around 500 F g^{-1} [48]) when studied in 1 mol L^{-1} H$_2$SO$_4$ aqueous electrolyte. Also, this material demonstrates good specific capacitance up to 236 F g^{-1} in the non-aqueous electrolyte, 1 mol L^{-1} LiClO$_4$ in a mixture of ethylene carbonate (EC), diethyl carbonate (DEC), and dimethylene carbonate (DMC) solution [47].

Considering free-standing CNT films for flexible composites, the electrochemical deposition method enables control over the polymer layer thickness preserving the original 3D structure [49,50]. Because the charge transfer reactions take place at the CNT/electrolyte interface, the nucleation of PANI should occur onto the CNT surface, suggesting uniform layer deposition. Such architecture offers a synthesis of ready-made flexible electrodes without any "dead" weight of a substrate, on which CNTs are usually deposited [39,44,51]. Nevertheless, despite recent progress, the effect of the structure of the SWCNT framework, morphology, and properties of PANI electrodeposited on the SWCNT film, on the capacitive performance of SWCNT/PANI composites have not been well evaluated.

1.2. Opening of SWCNT channels

In case of the *ex situ* SWCNT filling, the opening of the SWCNT internal channels is as important as the filling itself. While typically the as-synthesized SWCNTs exhibit single or both end-caps closed, the effectiveness of the end-caps opening is crucial for the efficient fluid flow into SWCNT channels facilitating f-SWCNT production [4]. The main mechanism of the SWCNT opening is based on the oxidative treatment. The carbon-carbon bonds of the highly curved SWCNT caps experience more strain when compared to the nanotube side-walls due to pentagon-containing cap structure that makes them more chemically reactive [5,6,32]. These structural peculiarities define the easier cap oxidation when compared to the side-walls, resulting in the opening of SWCNT channels.

1.2.1. Conventional opening approaches

The end-cap removal is usually realized with two main approaches: thermal treatment in the oxidative atmosphere (air, O_2, CO_2) [29,52,53] and treatment in inorganic acids [33,54,55]. Both techniques might be effective, although they hardly allow to control the degree of oxidation resulting into SWCNT body modification with the functional groups and formation of structural defects that may lead to the loss of a SWCNT wall structure integrity [27–30]. Moreover, the acid treatment could result in the blocking of opened ends preventing the filling of the channels [28,55]. These side effects of conventional opening approaches usually remain unconsidered in studies devoted f-SWCNT production.

1.2.2. Electrochemical opening method

The promising alternative approach for SWCNT channels opening is an electrochemical oxidation. It was shown that the electrochemical oxidative treatment in the aqueous electrolyte leads to the opening of the internal SWCNT channels [56]. Besides, it was reported that depending on the oxidative corrosion potential the resulting SWCNTs could exist in a closed, end-cap opened or side-wall opened state [57]. Therefore, when carefully employed, electrochemical oxidation opens the opportunity to control the strength of oxidative treatment with varying the oxidation "power" that is an applied electrode potential and vary the dose with changing treatment duration.

1.3. Applications of SWCNTs and hybrids

1.3.1. Transparent conductive films

Transparent conducting films are now in the limelight of modern electronics driven by the expanding field of flexible devices that include displays, touch screens, solar cells, *etc*. [58–60]. Apart

from high transparency and good conductivity, such applications require rather good flexibility of materials to be preferably made under cost-effective fabrication protocols. Commonly applied transparent metal oxides, such as indium-tin oxide (ITO), have several drawbacks, including high refractive index, limited flexibility, restricted chemical robustness, and depleted raw material supply. As a result, ITO is being impugned by alternatives like Ag nanowire mesh [61], PEDOT:PSS [62], graphene [63], reduced graphene oxide [64], and single-walled carbon nanotubes (SWCNTs) [65].

At the forefront, the materials such as SWCNTs are believed to be advantageous candidates for ITO replacement due to their excellent optoelectronic properties, chemical stability, abundant amount of carbon, and good adhesion to various substrates [19,66–68]. Their applications enable us to create entirely new components in flexible and stretchable transparent electronics [69–71]. However, in addition to carbon nanotube parameters such as length, the concentration of defects, and degree of bundling, their optoelectronic properties depend greatly on the ratio of semiconducting and metallic tubes, which directly impacts CNT–CNT junctions.

The most radical and efficient way to improve both optical and electrical properties of SWCNTs can be realized through tuning their Fermi level by adsorption doping [3,72]. This approach employs *p*- or *n*-doping compounds, which cause a shift of electron density depending on their redox potential relative to the potential of SWCNTs when adsorbed on their surfaces [73]. For redox species, more positive electrode potentials than that of the SWCNTs yield the efficient Fermi level downshift (*p*-doping) resulting in (i) transition of contacts between metallic and semiconducting SWCNTs from Schottky to ohmic, (ii) increase in charge carrier concentration, which in turn leads to a decrease in overall resistance, (iii) suppression of adsorption peaks associated with the transition between van Hove singularities (vHs), *i.e.*, leading to the improvement in transmittance. Among various dopants, chloroauric acid ($HAuCl_4$) has been found to be the most efficient one that enabled the state-of-the-art sheet resistance of 39 Ω sq^{-1} with the transmittance of 90 % at 550 nm to be achieved [20]. An appealing strategy to dope SWCNTs comprises the nanotube opening and subsequent dopant encapsulation that protects a dopant from ambient conditions.

1.3.2. Supercapacitors

Miniaturization of power sources is foreseen to drive the development of electronic and electrical engineering industries in the design of new wearable devices and electric vehicles which require flexible and lightweight systems for storing and converting the energy [74–77]. On the one hand, there is a demand for materials capable to accumulate a large amount of charge, *i.e.* lightweight high energy density systems, to reach high gravimetric and volumetric specific characteristics. On the other hand, the employment of flexible materials might improve the performance due to rational packaging such as

rolling-up architectures to reach appropriate nominal values and good compatibility with wearable devices [76–83]. Surely, the overall performance relies on many characteristics or parameters, such as cell geometry, charge storage mechanism, voltage loss, and current collector architecture. They also include the cycling stability of the electrode material and electrolyte durability under the applied current and the operating temperatures of the electrolyte.

Supercapacitors (SCs), first proposed by Becker [84] further studied by Trasatti [85] and Conway *et al.* [86–89], occupy an intermediate niche between "conventional capacitors" and "batteries" in the Ragone plot, constantly expanding the scope of their applications [75,90–92]. These devices possess a high power density close to or even superior to conventional capacitors, while their energy density approaches one of the batteries [93,94]. Formally, two major groups of SCs are differentiated depending on a charge storage mechanism: electrochemical double layer (EDL) capacitors and the ones based on electrochemical reactions, *i.e.* pseudocapacitance [38,92,95–97]. The EDL based SCs involve the redistribution of charges at the electrode-electrolyte interface for energy storage, requiring materials with a high specific area (distinct porosity) and excellent conductivity, such as carbon-based ones [93,98–100], with charge storage of *ca.* 0.18 e^- per surface atom. Whereas pseudocapacitive properties are attributed to different processes such as adsorption/underpotential deposition or fast reversible redox reactions (faradaic processes) with up to 1–2 e^- stored per atom [44,90]. Typical materials with pronounced pseudocapacitive properties are transition metal oxides [101–104], conducting polymers (CPs) [43,49,105–107], and carbon nanostructures decorated with electroactive functional groups [108]. Obviously, the rational combining of EDL and pseudocapacitive materials is expected to enhance the specific capacitance of SCs due to anticipated synergetic effects.

Carbon nanotubes (CNTs) are known materials for EDL-based SCs. The CNTs are proposed to be a feasible substitute for a metallic current collector such as aluminum due to their high conductivity and ability to operate at high current density without degradation [109]. CNT films are flexible and lightweight [110], allowing the reduction of the physical size of SCs, their weight, and cost [79,111]. Uniquely, films made of single-walled carbon nanotubes (SWCNTs) might be realized in a free-standing configuration under a dry-transfer protocol enabling high access to the surface and great flexibility [112,113]. However, the high conductivity and chemical stability of these materials coexist with the low specific capacitance of ~150 F g^{-1}, which reduces the number of applications for SCs based on the SWCNTs [93,114]. Complementary, soft mater like CPs, with pseudocapacitive properties, ensures higher capacity, energy density, and good flexibility [115]. The CPs are usually characterized by a well-organized three-dimensional structure, high specific surface area, and good diffusion characteristics [116]. Polyaniline (PANI) is one of the most popular CPs due to its high electrochemical activity and simple synthesis protocols [106,117,118]. The specific capacitance of PANI strongly depends on the

method of synthesis and protonation state reaching values up to $1000 \, F \, g^{-1}$ [119]. Such a high capacitance value is theoretically proven to be associated with PANI molecules' structure favoring a proton-diffusion-based mechanism of conductivity, while many other CPs have lower conductivity and accumulate less energy [117]. The conductivity of a PANI film depends on the protonation state and form of a polymer chain leading to a change in conductivity during charging-discharging. PANI has the best performance in protonic media like an acid solution, whereas in other electrolytes charge accumulation is less efficient [120,121].

CHAPTER 2. MATERIALS AND METHODS

2.1. SWCNT thin films synthesis

Single-walled carbon nanotubes used in the thesis research were synthesized by a floating catalyst (aerosol) chemical vapor deposition (CVD) method in a laminar flow reactor as described elsewhere [2,19,122]. The process is based on the disproportionation of carbon monoxide (Boudouard reaction) on the surface of iron nanoparticles, which are formed in the reactor by means of the ferrocene vapor decomposition. During the SWCNT synthesis iron catalytic nanoparticles become encapsulated in the as-synthesized carbon nanotubes. Average values of nanotubes' length and diameter are 20-40 μm and 2.1 nm, correspondingly. SWCNT films comprising randomly oriented SWCNTs were produced through collection of SWCNT aerosol on the nitrocellulose membrane filter. By varying the collection time, we made films of different thicknesses, which is associated with the optical transmittance at the wavelength of 550 nm. Specifically, $Th = 239 \times A_{550}$, where Th is the film thickness (nm), and A_{550} is the absorbance at the wavelength of 550 nm [123–125]. In order to place the SWCNT film on the desired substrate we used the dry-transfer technique [21].

For bilateral doping research we used SWCNT films of 70 % transmittance at the wavelength of 550 nm, which corresponds to the thickness of 37 nm. Pristine SWCNT film samples were cut with a size of 10×10 mm^2 and deposited onto quartz substrates using a dry-transfer technique.

For electrochemical treatment influence on SWCNT structure and filling efficiency we employed SWCNT films of ~87 % transmittance in the middle of visible region (550 nm). SWCNT film samples about 18×10 mm^2 were cut from a larger film and then dry transferred onto the 20×12 mm^2 Kapton® (DuPont de Nemours, Inc., U.S.A.) substrates with the rounded-corners square opening of 6×6 mm^2 to get a free-standing SWCNT film geometry [112].

For production of SWCNT/PANI composites we utilized the films with the transmittance of 80 %, 90 %, and 95 % denoted in the corresponding sub-chapter as *SWCNT80*, *SWCNT90*, and *SWCNT95*, those thicknesses are around 23, 11, and 5 nm, respectively. Free-standing SWCNT films were prepared by a simple dry-transfer technique [112]. The films were transferred from the filters to the 3 mm thick poly(methylmethacrylate) (PMMA) frames with square openings of 10×10 mm^2. Free-standing SWCNT films on the PMMA frames were utilized as working electrodes for electrochemical deposition of PANI.

2.2. Methods of SWCNT film processing

2.2.1. Preparation of SWCNT films for electrochemical treatment

To avoid impact of film densification on the properties of SWCNT film [126], all samples were preliminary immersed into deionized water and then dried at the ambient conditions. Removal of adsorbed gaseous species and adsorbed water was done by heating the sample films in the oven for 15 min at 195 ºC and pressure of 0.05 bar. Such samples described exhibit intrinsic SWCNT properties are denoted as densified and heated: *SWCNT-DH* in dedicated sub-chapter of the thesis. These properties were assigned to be a benchmark for evaluation of material characteristics upon to the electrochemical treatment.

For proper analysis of cyclic voltammogram features, we prepared iron-free sample (*SWCNT-woFe*) that was used to compare with the as-synthesized SWCNT films. To remove the iron nanoparticles, free-standing SWCNT film was heated to the temperature of 1400 ºC for 3 min by Joule heating in the vacuum chamber at pressure $5 \cdot 10^{-6}$ Torr [127]. The resulting *SWCNT-woFe* film was then transferred on the Kapton® substrate and processed in the similar way to *SWCNT-DH* film.

2.2.2. Opening of SWCNTs

2.2.2.1. Thermal opening

For thermal treatment of SWCNT films on quartz substrate we heated them at the heating rate of 10 ºC min^{-1} in a muffle furnace (Nabertherm GmbH, Germany) to the desired temperature (up to 500 ºC) in the ambient atmosphere. After the heat-treatment of the SWCNTs for 20 min, the samples were removed from the furnace and remained at room temperature to cool down.

2.2.2.2. Electrochemical opening

Electrochemical treatment of SWCNT films was conducted by means of cyclic voltammetry (CV) using the potentiostat P40-X (Electrochemical Instruments, Russia). A three-electrode configuration was used with the cell volume of 250 mL. SWCTN films on the Kapton® substrate with attached conductive copper tape represented the working electrode. Iridium wire was employed as an auxiliary electrode while a reversible hydrogen electrode (RHE) was used as a reference electrode. Aqueous 0.5 mol L^{-1} sulfuric acid electrolyte of approximately 150 mL was purged with nitrogen for 1 h prior the experiments. The pH value of the electrolyte was measured using Oakton® pH 6+ handheld pH meter (Environmental Express, USA) to be 0.77 ± 0.01. Before all the tests, we pre-treated all samples by cycling the potential in the range 0.2-0.4 V at the scan rate of 20 mV s^{-1} for 15 cycles. The electrochemical treatment included the potential cycling over 100 cycles at 20 mV s^{-1}. The lower vertex potential for electrochemical treatment was fixed for all samples at the level of 0.2 V to avoid the

hydrogen evolution reaction on the SWCNT film. Upper vertex potential (UVP) was varied for different samples from 0.7 to 1.7 V with 0.2 V step to investigate the material structure and filling efficiency depending on the UVP. However, SWCNT film treated at UVP = 1.7 V undergoes strong oxidation during the treatment, thus the film loses structural integrity under the surface tension of the electrolyte. Therefore, results regarding the film treated at such conditions were mostly omitted.

The reference sample used in the corresponding sub-chapter was prepared in the similar way with the application of the pre-treatment, but instead the electrochemical treatment it was left immersed in the electrolyte for 2.5 h.

The electrochemically treated films were then dried at ambient conditions. Additional vacuum oven heating at the same conditions was done for complete water elimination and gaseous species desorption from the film surface (*SWCNT-EH*).

2.2.3. Adsorption doping of SWCNT films

The adsorption doping procedure was carried out by a drop-casting of 7 μL of 15 mmol L^{-1} $HAuCl_4$ ($HAuCl_4 \cdot 3H_2O$, Acros Organics, Thermo Fisher Scientific Inc., U.S.A.) solution in ethanol (99.5 %, ETAX) onto the 10×10 mm^2 SWCNT film at room temperature.

2.2.4. Filling of SWCNTs

The filling of SWCNTs was carried out to estimate the filling efficiency of SWCNT films after electrochemical treatment. In order to do this, we dip coated *SWCNT-EH* films in the 15 mmol L^{-1} ethanol solution of $HAuCl_4$ for 5 min with a 200 mm min^{-1} withdrawal speed.

2.2.5. Electrochemical deposition of PANI

We performed potentiodynamic deposition of PANI on SWCNT films using a three-electrode cell configuration. SWCNT films, a platinum foil, and Ag|AgCl$_{(sat)}$ electrode (ESr-10102, Izmeritelnaya tekhnika, Russia; 197 mV *versus* standard hydrogen electrode) were used as working, counter, and reference electrodes, respectively. All electrochemical tests were performed with a potentiostat VMP3 Biologic SAS (Bio-Logic SAS, France). Electrochemical polymerization of $C_6H_5NH_2$ was carried out using cyclic voltammetry (CV) technique within the potential range [-200; 800] mV *vs.* Ag|AgCl$_{(sat)}$ electrode at the 20 mV s^{-1} scan rate, using 0.5 mol L^{-1} aqueous solution of $C_6H_5NH_2 \cdot HCl$ in 1 mol L^{-1} H_2SO_4 as the electrolyte and monomer source. We monitored the charge over the cycle number to control the thickness of the deposited PANI. As-deposited films of SWCNT/PANI composites were washed with deionized water and dried in air for 24 h. We synthesized sample series with 40, 50, 60, and 70 PANI deposition cycles for each SWCNT film.

2.3. Characterization methods

2.3.1. Electrochemical methods

The open-circuit potential (OCP) measurements were conducted in a three-electrode cell with SWCNTs as a working electrode, Pt counter electrode and KCl saturated Ag|AgCl$_{(sat)}$ reference electrode. OCP transients were recorded using a BioLogic VMP3 (Bio-Logic SAS, France) potentiostat/galvanostat, the sampling rate was set to be 0.5 Hz. The OCP measurements were carried out for both pristine and thermally treated SWCNT films, where the samples were obtained by thermal treatment the pristine SWCNTs at 350 ºC. The ohmic drop was estimated to be negligible (*ca.* 0.003 V) and was not considered in OCP measurement.

Performance of SWCNT/PANI composites was evaluated the in 1 mol L^{-1} H$_2$SO$_4$ exploiting both three- and symmetric two-electrode cell configurations. For three-electrode cell measurements, SWCNT/PANI composites were used in an as-prepared form. The potential range was [0; 1000] mV for CV studies and [0; 800] mV *vs.* Ag|AgCl$_{(sat)}$ electrode for galvanostatic charge-discharge tests. Electrical contact was realized *via* the SWCNT film not covered by PANI. In the case of the three-electrode cell, the CV studies were carried out using 20, 50, 100, 250 mV s^{-1} scan rates, while the galvanostatic charge-discharge tests were performed at 4.3 A g^{-1} current density. Also, we measured capacitance retention by monitoring open circuit potential [90] for 10 min after charging to 800 mV *vs.* Ag|AgCl$_{(sat)}$ electrode to evaluate self-discharge of prepared composites, which possibly stems from current leakage.

The specific capacitance of the SWCNT/PANI composites was calculated from CV data using equation (1):

$$C_{Sp} = \frac{\oint idE}{2\Delta E \cdot v_s \cdot m} \ (1)$$

where C_{Sp} is a specific gravimetric capacitance of the material, i is current, ΔE is the potential range, v_s is the potential scan rate, m is the material mass.

To realize the two-electrode configuration, two SWCNT/PANI composite films with a separator Whatman™ GF/A, 0.26 mm were carefully transferred to an ECC-Std cell (Ell-Cell, Germany) imitating a coin cell type supercapacitor. In such a configuration, the entire film surface of the SWCNT/PANI composite films was in contact with cell current collectors (stainless steel) *via* the PANI layer. CV studies were performed at the 20 mV s^{-1} scan rate and using voltage range of [0; 800] mV. Galvanostatic charge-discharge measurements were carried out at a current density of 4.3 A g^{-1}. Similarly, we tested capacitance retention by assessing the open circuit voltage for 10 min after charging to 800 mV.

The specific capacitance values of the composite materials were calculated by processing galvanostatic charge-discharge data using equation (2):

$$C_{Sp} = \frac{I \cdot t}{\Delta E \cdot m} \ (2)$$

where C_{Sp} is a specific gravimetric capacitance of material, I is current, ΔE is a potential range, t is a discharge time, m is a material mass.

To estimate specific capacitance at different charge-discharge rates and bent angles of free-standing electrodes we fabricated a device in the two-electrode free-standing configuration. First, 90 % transmittance at 550 nm wavelength SWCNT film of 13×18 mm^2 was transferred on a Kapton® (DuPont de Nemours, Inc., U.S.A.) substrate with an area available for the electrolyte of 10×15 mm^2. Then it was immersed in the 0.5 mol L^{-1} aqueous solution of $C_6H_5NH_2 \cdot HCl$ in 1 mol L^{-1} H_2SO_4 to expose 10×10 mm^2 of free-standing SWCNT film for PANI electrodeposition employing 40 cycles. After composite material was obtained, a free-standing film 10×15 mm^2 (composite part is 10×10 mm^2, another part is uncovered SWCNT film acted as a current collector) was transferred onto poly(dimethylsiloxane) (PDMS) film. Two electrodes were then oriented so that composite films were overlapping, while current collector areas were directed to opposite sides (Figure A1). Cu tape was utilized to connect assembled device to potentiostat clamps. For electrodes' separation, the Whatman™ glass microfiber filter (grade GF/A) was used. 1 mol L^{-1} H_2SO_4 water solution was used as an electrolyte to wet the glass separator.

2.3.2. Spectroscopy

2.3.2.1. UV-Vis-NIR absorption spectroscopy

In purpose of bilateral doping assessment UV-Vis-NIR absorption spectra were measured in the wavelength range of 190–2690 nm using the Lambda 1050 (PerkinElmer Inc., U.S.A.) spectrophotometer. To ensure the reproducibility of the measurements for each sample, 3 spectra were collected and averaged. For electrochemical treatment evaluation UV-Vis-NIR absorption spectra of SWCNT films were collected for free-standing film in the wavelength range of 180-3200 nm with a 2 nm scanning resolution. Although SWCNT films are known to possess quite uniform properties over the surface, still it might exhibit some inhomogeneity of their thicknesses [21]. To provide consistency and reliability of comparison between different samples, all pieces of SWCNT films used in the electrochemical treatment evaluation studies were taken to have similar optical properties that is shown in Appendix (Figure A2).

2.3.2.2. Raman spectroscopy

Raman spectroscopy was utilized to evaluate structural changes of the SWCNT films [128]. Spectra were obtained with a DXRxi Raman Imaging Microscope (Thermo Fisher Scientific Inc., U.S.A.) with a diode-pumped solid-state laser operating at 532 nm. At least 5 spectra for each sample were recorded in the region 50-2950 cm^{-1} at a 0.5 mW laser power. The laser spot diameter on the film surface was 5-11 μm. All spectra were normalized to the intensity of G-mode of SWCNTs and averaged to allow correct comparison of relative peaks' intensities.

For the evaluation of the functional composition of the SWCNT/PANI composites we utilized samples obtained through 70 potential sweep cycles of PANI electrodeposition.

2.3.2.3. X-ray photoelectron spectroscopy

Analysis of the material surface chemical composition was conducted by means of X-ray photoelectron spectroscopy (XPS). The spectra were recorded with PHI 5000 VersaProbe II (Physical Electronics Inc., ULVAC-PHI Inc., Japan) using Al K_α X-ray source of a 1486.6 eV energy from a 50-200 μm spot with used parameters of 50 W beam power, accelerating voltage of 15 kV and incidence angle 45°.

Spectra deconvolution and quantification of functional groups was done using CasaXPS software v2.3.25 and v.2.3.17 (Casa Software Ltd., UK). Standard deviations of synthetic peak areas were estimated using the CasaXPS v2.3.25 software built-in calculation feature based on the Monte Carlo procedure. Residual standard deviation of the peak model was calculated with the abovementioned software.

Survey spectra were collected at a 117.4 eV pass energy in the range of 0-1350 eV binding energies with a 0.5 eV resolution and averaged over 4-6 scans.

High-resolution C1s spectra were registered at a 23.5 eV pass energy in the range of 276-296 eV binding energies with a 0.1 eV resolution and averaged over 6-7 scans. C1s spectra peaks were modeled using Gaussian/Lorentzian product symmetrical and asymmetrical functions after the internal calibration of C1s peak binding energy to be 284.5 eV and subtraction of the background by Shirley's method. Concentrations quantification of the C1s chemical states was done using peak areas of the corresponding components in the peak model considering photoionization cross-sections of the elements at given photon energy.

Au4f, Cl2p and core level spectra collected for bilateral doping evaluation are refined by multiple scanning and peaks are approximated by the Lorentz–Gauss function.

The high-resolution S2p, N1s and O1s spectra used in assessment of SWCNT/PANI composites were measured in BE ranges (with a number of sweeps) 157.0–177.0 (7 sweeps), 388.0–410.0 (10 sweeps) and 520.0–542.0 eV (8 sweeps), respectively. The BE scale was internally calibrated to the energy 284.4 eV of the C1s peak. The high-resolution spectra were deconvoluted using Gaussian/Lorentzian and Doniach-Sunjic functions after subtraction of the non-linear background by Shirley's method.

Atomic concentration of oxygen in samples used in electrochemical treatment influence investigation was calculated based on the survey spectra and ratio of C1s and O1s lines.

2.3.3. Microscopy

For assessment of SWCNT microstructure before and after adsorption doping we performed transmission electron microscopy (TEM) using a Tecnai G2 F20 (FEI, Thermo Fisher Scientific Inc., U.S.A.) microscope operating at a 100 kV accelerating voltage. The morphology of the SWCNT films was analyzed and the diameters of the SWCNT bundles were estimated based on the sample statistic of around 200 points. Scanning transmission electron microscope (STEM) observations were carried out in an aberration-corrected UltraSTEM-100 (Nion Co., U.S.A.) microscope operated at 60 keV electron energy. The beam semi-convergence angle was 30 mrad, and the elastically scattered electrons were detected with a medium angle annular dark field (MAADF) detector with a collection semi-angle of 60–200 mrad. A MAADF detector was used to improve the contrast of light elements including carbon, and thus, to facilitate the accurate determination of SWCNT wall positions in the images. The column vacuum around the sample stage was in the order of 10^{-10} mbar during the experiments, suppressing chemical reactions.

Accessibility of SWCNT internal voids and formation of Au-nanowires were examined using transmission electron microscopy. Images of high angle annular dark field scanning transmission electron microscopy (HAADF-STEM) were acquired using Titan Themis Z (Thermo Fisher Scientific Inc., U.S.A.) operating at a 200 kV accelerating voltage. The transmission electron microscope was equipped with DCOR+ condenser system spherical aberrations corrector.

The morphology and structure of prepared SWCNT/PANI composites were examined by scanning (SEM) and transmission electron (TEM) microscopy techniques. SEM micrographs were obtained using a JIB-4700F (JEOL Ltd., Japan) microscope at an accelerating voltage of 5 kV and using Thermoscientific Quattro device (FEI, Thermo Fisher Scientific Inc., U.S.A.) at 10 kV accelerating voltage. TEM images were acquired using JEM-2800 (JEOL Ltd., Japan) and Tecnai G2 F20 (FEI, Thermo Fisher Scientific Inc., U.S.A.) microscopes at a 100 kV accelerating voltage in both cases.

2.3.4. SWCNT films electrical properties assessment

Electrical properties of SWCNT films were evaluated by measuring sheet resistance of the SWCNT films in the linear four-probe configuration at 1 mA testing current using RM3000 Test Unit (Jandel Engineering Ltd, UK).

Sheet resistance values for each sample were recorded 3-5 times and then averaged to avoid the influence of the film anisotropy.

For a quantitative optoelectrical property evaluation of different SWCNT films, we compared their equivalent sheet resistances (R_{90}) [129] calculated for the transmittance of 90 % at 550 nm according to the equation (3):

$$R_{90} = \frac{R_S \cdot A_{550}}{\log_{10}(10/9)} \ (3)$$

where R_S is sheet resistance (in $\Omega\,\text{sq}^{-1}$) and A_{550} is the absorbance at the wavelength of 550 nm.

Testing spot of SWCNT films used in electrochemical treatment studies was the area of the film exposed to the electrochemical treatment, yet supported on the substrate.

2.3.5. SWCNT filling efficiency evaluation

On the basis of STEM images we counted the number of encapsulated gold nanowires (NWs) and measured their length using ImageJ2 software for each sample from at least 0.4 μm^2 area. The encapsulation efficiency of SWCNT films was evaluated using the value of the encapsulated nanowires length per unit area of SWCNT film that was calculated as the ratio of total length of encapsulated NWs to the area of SWCNT film examined from STEM images.

Gold nanowires length distribution curves were obtained with the application of kernel density estimation assuming normal kernels and 0.2 bandwidth fixed throughout all SWCNT sample films. All the curve areas were normalized using the total nanowires occurrence frequency in the particular SWCNT film, *i.e.* number of distinguishable nanowires divided by the examined SWCNT film area.

2.3.6. Mass calculation and weighting of SWCNT/PANI composites

For the gravimetric capacitance calculations, SWCNT/PANI composite films were weighted using scales of the simultaneous thermal analysis device STA 449 F3 Jupiter® (Erich NETZSCH GmbH & Co. Holding KG, Germany), enabling estimation of mass with high precision (gravimetric resolution is 0.1 μg). For these tests, we transferred the material to alumina crucibles and weighted it in a closed device.

To calculate the masses of SWCNT films, the densities of the films were multiplied by the area of the films. The densities were calculated according to equation (4):

$$\rho_T = \rho_{0.5} \times \frac{\log_{10} T}{\log_{10} 0.5} \quad (4)$$

where T is a transmittance of SWCNTs film at 550 nm, $\rho_{0.5} = 5.5$ µg cm^{-2} is the density of the film with the transmittance of 50 %, and ρ_T is a density of the film with the transmittance T [130].

2.4. DFT calculations

The calculations of Fermi-level changes induced by adsorption doping were performed by a density functional theory (DFT) method within the Perdew–Burke–Ernzerhof general gradient approximation [131]. We used the projector augmented wave method approximation [132] with the periodic boundary conditions as implemented in the Vienna ab initio Simulation Package [133,134]. A plane-wave energy cut-off was set to 400 eV. Structural relaxation was performed until the forces acting on each atom became less than 10^{-3} eV Å^{-1}. Van der Waals interaction was taken into account with the Grimme-d3 functional [135]. For the investigation of doping effects, we used 240 carbon atoms per SWCNT (10,10) supercell. Geometry optimization was performed in Gamma point, while for the precise density of states (DOS) and band structure calculations, the $1 \times 1 \times 4$ Monkhorst–Pack scheme was implemented [136]. To avoid spurious interactions between the neighboring unit cells, the translation vector along the non-periodic direction was set to be greater than 15 Å.

CHAPTER 3. RESULTS AND DISCUSSION

3.1. Bilateral doping of SWCNT films

3.1.1. Thermal treatment

To optimize our method for efficient SWCNT doping utilizing their inner space for dopant incorporation, we evaluated optoelectronic and structural changes, induced by SWCNT thermal treatment in the range from 100 to 500 ºC. For these purposes, we used UV-Vis-NIR and Raman spectroscopies, and four-probe sheet resistance measurements.

3.1.1.1. Changes in optical and electrical properties induced by treatment

UV-Vis-NIR absorption spectra were measured to analyze the electronic states of SWCNTs before and after the thermal treatment (Figure 1). Spectra usually clearly display the excitonic transitions between van Hove singularities (vHs) in semiconducting (S_{11} and S_{22}) and metallic (M_{11}) SWCNTs. It should be noted that SWCNT films are environmentally doped by adsorbed gaseous species. In order to clearly represent the processes occurring during the thermal treatment in the temperature range examined, we plotted the absorbance values at the wavelengths of 2378, 1310, and 894 nm, which corresponded to the mean value of S_{11}, S_{22}, and M_{11} transitions (Figure 1b). S_{11} peak intensity exhibits significant monotonous growth with the temperature increase up to 350 ºC, the intensity of S_{22} peak is characterized by the same behavior pattern, although with a smaller growth rate, and the M_{11} peak remains nearly unaltered up to 350 ºC. When the treatment temperatures surpass 350 ºC, all peaks start to decrease remarkably. The initial growth of S_{11} and S_{22} peak intensities with temperature up to 350 ºC can be attributed to the desorption of oxygen, which is known to be adsorbed by the SWCNT surface from the air leading to the *p*-doping effect [137,138]. Rapid fall of all peak intensities at higher temperatures (400 ºC and above) indicates the oxidation of SWCNTs, which starts from end-caps since they are the most reactive parts of nanotubes [139].
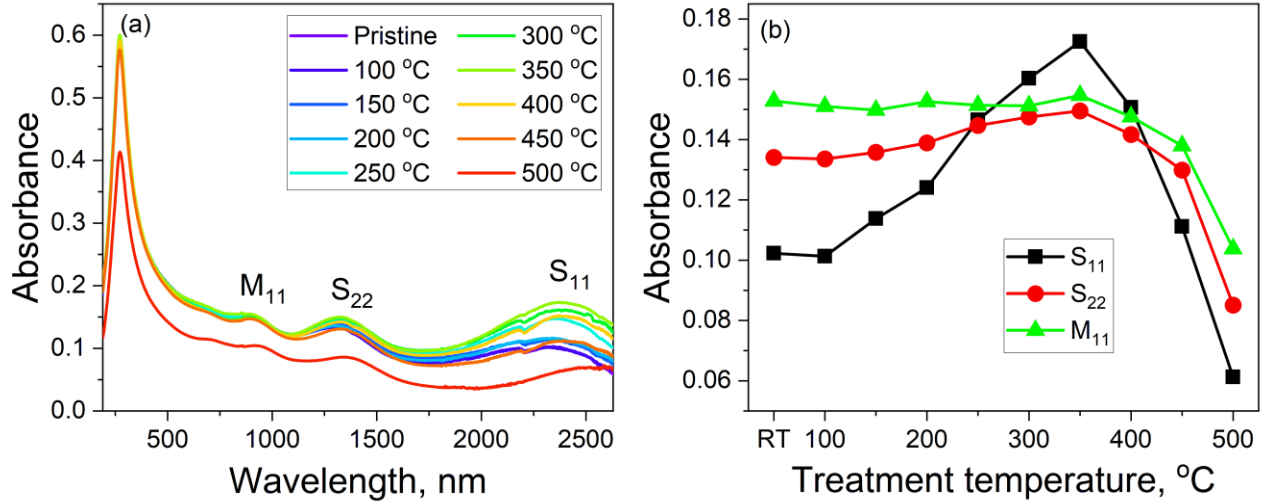
Figure 1. UV-Vis-NIR absorption spectra of the SWCNT films treated at different temperatures (a). Intensity of S_{11} (2378 nm), S_{22} (1310 nm), and M_{11} (894 nm) peaks as a function of the treatment temperature (b).

Since transmittance in visible spectrum, particularly at 550 nm, and equivalent sheet resistance (R_{90}) are parameters defining quality of transparent conductors, we monitored their variations with the change in the treatment temperature. Figure 2 represents relative changes in T_{550} and R_{90} in comparison to the pristine sample, as functions of the treatment temperature. Transmittance and equivalent sheet resistance were calculated following the equations (3) and (5):

$$R_{90} = \frac{R_S \cdot A_{550}}{\log_{10}(10/9)} \quad (3)$$

$$A_{550} = -\log_{10} T_{550} \quad (5)$$

where A_{550} is the absorbance at the wavelength of 550 nm, T_{550} is the transmittance at the wavelength of 550 nm and R_S is sheet resistance (in Ω sq^{-1}).

The transmittance (Figure 2) remains almost unchanged when SWCNT films are treated at temperatures up to 350 °C, although at higher temperatures the transmittance increases markedly. It have to be attributed to the oxidation of the carbon and oxidation of residual catalytic nanoparticles. The equivalent sheet resistance experienced continuous growth with the increase of the treatment temperature, which can be explained by the desorption of oxygen from the SWCNT surface and the oxidation of SWCNTs at temperatures higher than 350 °C.
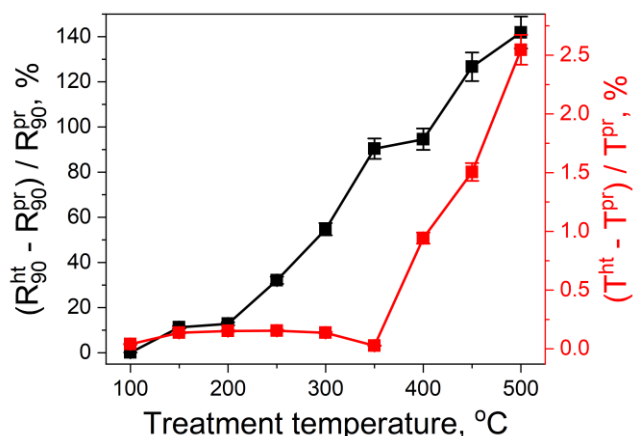
Figure 2. Relative changes of transmittance and equivalent sheet resistance of SWCNT films treated at different temperatures.

3.1.1.2. Structural changes caused by temperature treatment

The quality of SWCNTs was estimated as the ratio of G- to D-mode intensities (I_G/I_D) calculated using Raman spectroscopy data. The thermal treatment of the SWCNT films up to 300 ºC did not lead to significant changes in the I_G/I_D ratio. Further increase in the temperature caused a slight decrease in the I_G/I_D ratio, which might be attributed to the introduction of defects in the SWCNTs due to the oxidation process in the air (Figure 3a). These results are in accordance with the changes in the intensity distribution in the RBM frequency range with increasing treatment temperature (Figure 3b). The RBM peaks remain unaltered up to 300 ºC, and a further increase in the temperature leads to the disappearance of RBM peaks corresponding to smaller diameters, which are more reactive [140].
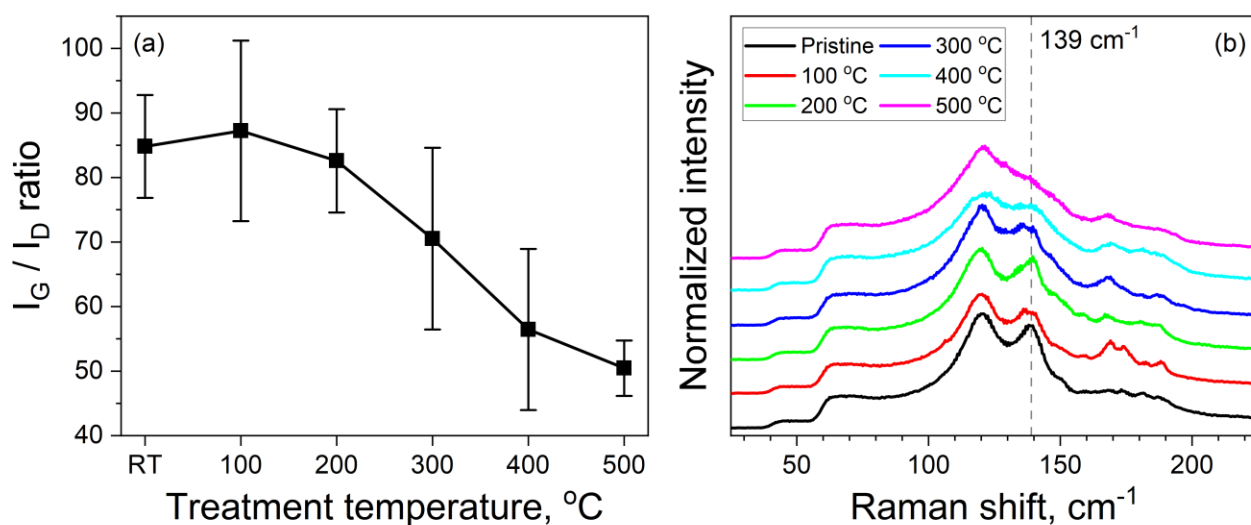
Figure 3. Raman spectra alterations with thermal treatment of SWCNT films at different temperatures. Evolution of the I_G/I_D intensity ratio (a) and RBM-mode after treatment at different temperatures (b).

3.1.2. Doping procedure

For high-efficiency SWCNT doping, we implemented a facile method of thermal treatment in an ambient atmosphere with a subsequent drop-casting of $HAuCl_4$ solution. Thermal treatment of SWCNT films in the range of 300–500 °C facilitates opening the tubes, *i.e.* by the cap removal, exposing the inner surface of the tubes to the environment. To increase conductivity and transmittance of the SWCNT networks, we utilized one of the strongest electron acceptor dopants for SWCNT films – chloroauric acid ($HAuCl_4$) [141]. Extraction of electron density from SWCNTs promotes the reduction of gold from the oxidized state to metallic one, which decorates the SWCNT surface in the form of Au^0 nanoparticles [142].

Figure 4 shows the equivalent sheet resistance and transmittance as a function of the thermal treatment temperature of pristine SWCNTs doped with 15 mmol L^{-1} $HAuCl_4$ ethanol solution. The equivalent sheet resistance, R_{90} is a quantitative measure for conductive transparent materials that balances the sheet resistance and transmittance of SWCNT films and usually assessed at the film transmittance of $T_{550} = 90$ % according to the equation (3) [129]. While the pristine SWCNTs typically had equivalent sheet resistance of about 150 Ω sq^{-1}, drop-casting of the $HAuCl_4$ solution yielded a reduction of R_{90} by 65 %. After the treatment at 300–400 °C, doped SWCNTs exhibit the lowest R_{90} value approaching a record of 31 ± 4 Ω sq^{-1} (at 400 °C). A change in R_{90} is primarily attributed to *p*-doping by $[AuCl_4]^-$ species. The electrochemical potential of $[AuCl_4]^-$ species is high enough [73,143] to force the first and the second vHs electrons to disappear that is especially pronounced in the case of tubes with a large diameter [142]. Such doping effect is manifested in the UV-Vis-NIR transmittance spectra (Figure 4b), leading to the removal of S_{11}, S_{22}, and M_{11} peaks and the appearance of a new peak located at the wavelength close to that of the initial S_{22} peak. It corresponds to the nanotubes' intersubband plasmon appearing when the excitonic levels are fully saturated with charge carriers [125,144]. These data prove that *p*-doping caused an efficient downshift of the Fermi level favored by $HAuCl_4$ treatment.
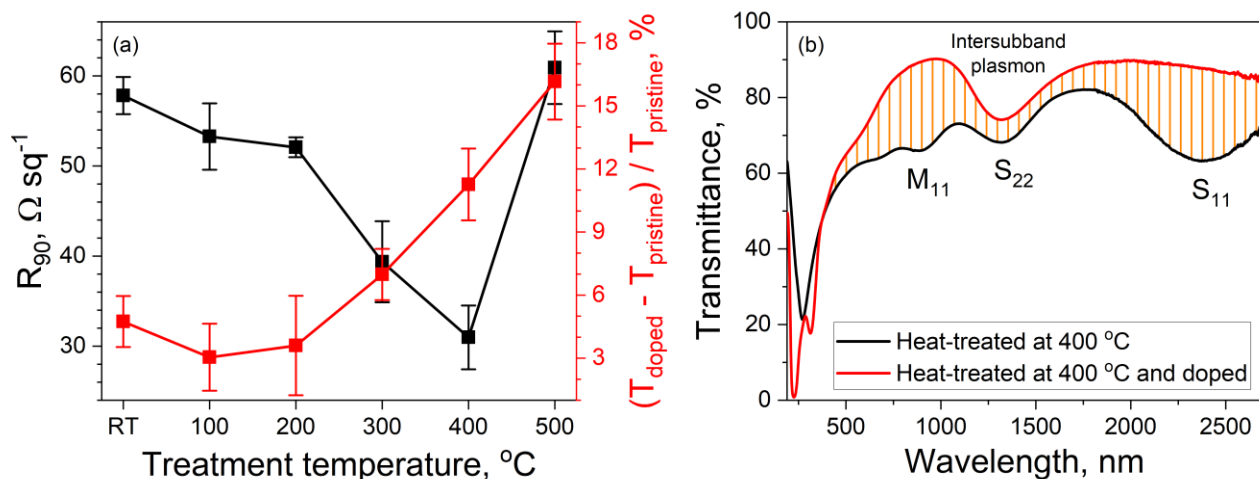
Figure 4. Effect of thermal treatment and doping on optoelectronic properties of SWCNTs. Equivalent sheet resistance and transmittance of the SWCNT films treated at different temperatures (100–500 ºC) for 20 min followed by doping with 15 mmol L^{-1} $HAuCl_4$ ethanol solution (a). UV-Vis-NIR absorption spectra of the SWCNT film treated at 400 ºC in the air (black) and the same film after doping (red) with 15 mmol L^{-1} $HAuCl_4$ (b). Hatched area illustrates film transmittance increase in the visible and NIR range due to the doping.

An increase in the transmittance after the doping of nanotubes treated at temperatures above 300 ºC can be attributed to the entering of the dopant into the SWCNTs' inner space, favored by the opening of the tubes. At temperatures above 400 ºC, we observe a deterioration of the sheet resistance that can be explained by the formation of numerous defects due to the destructive oxidation of SWCNTs. Although at 500 ºC higher transmittance should have improved R_{90}, this effect is negated by a significant sheet resistance jump.

3.1.3. Characterization of doped SWCNTs

We have evaluated the doping efficiency of SWCNT films treated at 100–500 ºC using Raman spectroscopy. The Raman spectrum of the pristine SWCNT films (Figure 5a) typically contains chirality sensitive radial breathing mode (RBM) around 100-500 cm^{-1}, D-mode peak near 1340 cm^{-1}, graphitic G-mode peak near 1590 cm^{-1}, and 2D-mode peak at 2680 cm^{-1}. The RBM is an out-of-plane bond-stretching mode, where peak wavenumbers are inversely proportional to the SWCNT diameter, the D-mode reflects the concentration of structural defects, the G-mode is responsible for tangential vibrations of carbon atoms, and the 2D-mode is the second harmonic overtone of the D-mode [145].
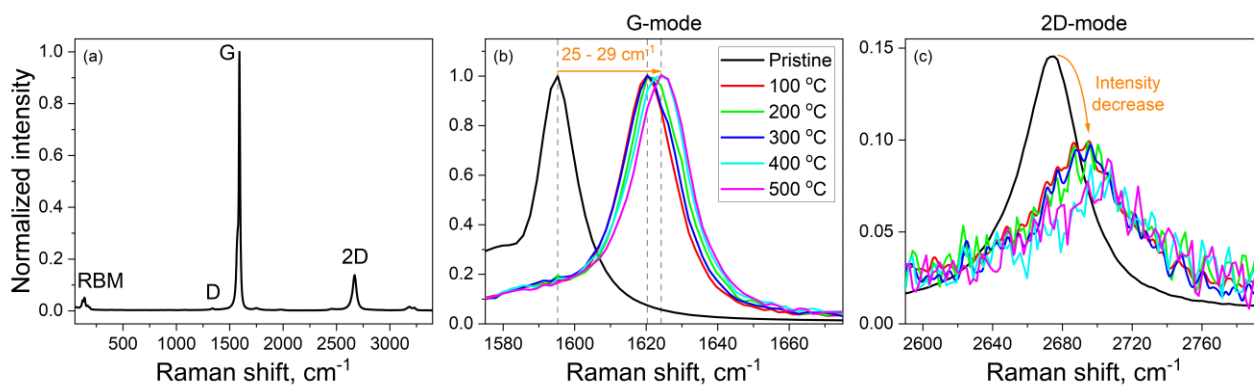
Figure 5. Raman spectra of pristine SWCNTs (a); G-mode (b) and 2D-mode (c) peaks of doped SWCNTs after thermal treatment at 100–500 ºC in comparison to the pristine film.

Figure 5b,c present respectively G- and 2D-mode changes of SWCNT films treated at 100–500 ºC with subsequent HAuCl$_4$-doping. Typically, blue shifts of the G-mode peak and 2D-mode positions are attributed to the *p*-doping [3,146]. The G-mode peak of all samples shifts to higher values of *ca.* 25–28 cm^{-1}, while the G-mode peak of films treated at 400 and 500 ºC demonstrates a slightly greater shift (29 cm^{-1}) when compared to the others (Figure 5b). 2D-mode peak intensities experience a remarkable decrease accompanied by the peak position upshift. Similar to G-mode changes, 2D-mode alterations are most pronounced for 400 and 500 ºC-treated SWCNT films (Figure 5c). Therefore, SWCNTs thermally treated at 100–500 ºC experience strong *p*-doping. In the meantime, the doping efficiency of films treated at 400–500 ºC is higher than in the case of other temperatures, which can be attributed to the caps' removal at temperatures above 300 ºC and effective doping of the opened SWCNTs.

The origin of more efficient SWCNT doping due to the prior caps' removal *via* thermal treatment is also supported by our TEM observations. Figure 6 displays TEM images of HAuCl$_4$-doped films of both pristine and thermally treated SWCNTs. In images of pristine and treated up to 300 ºC SWCNTs, we observe the decoration of nanotubes' surface with metallic gold nanoparticles with a size of approximately 5–10 nm (Figure 6a,b). In contrast, for samples thermally treated at 400 ºC, in addition to outer surface decoration with Au^0 nanoparticles, we can notice the filling of the inner SWCNT space (Figure 6c,d). Measurement of the interplanar spacing of the encapsulated material from the TEM images resulted in a value of 0.235 nm. It was admitted to be metallic gold, which has a (111) interplanar spacing of 0.2355 nm (PDF-2 [4-784]). Gold nanoparticles formed *via* spontaneous reduction of [AuCl$_4$]$^-$ anions decorate the outer surface of SWCNTs. When the heat-treatment temperature is high enough to oxidize the nanotube caps, *e.g.* 400 ºC, the doping solution penetrates into the SWCNT inner

space, resulting in improved doping and, also, the formation of the metallic gold phase. This is manifested in higher doping efficiency for the SWCNT film treated at 400 ℃, which explains its record R_{90} value.

Although we attributed the formation of Au^0 nanoparticles and encapsulated gold wires to spontaneous reduction of $[AuCl_4]^-$, some parts of metallic gold can be formed under the exposure of a 100 kV TEM electron beam [147]. Therefore, we carried out STEM measurements at a low voltage of 60 keV electron energy (Figure 6c,d). No transformation of nanowires inside nanotubes during the measurements was observed.
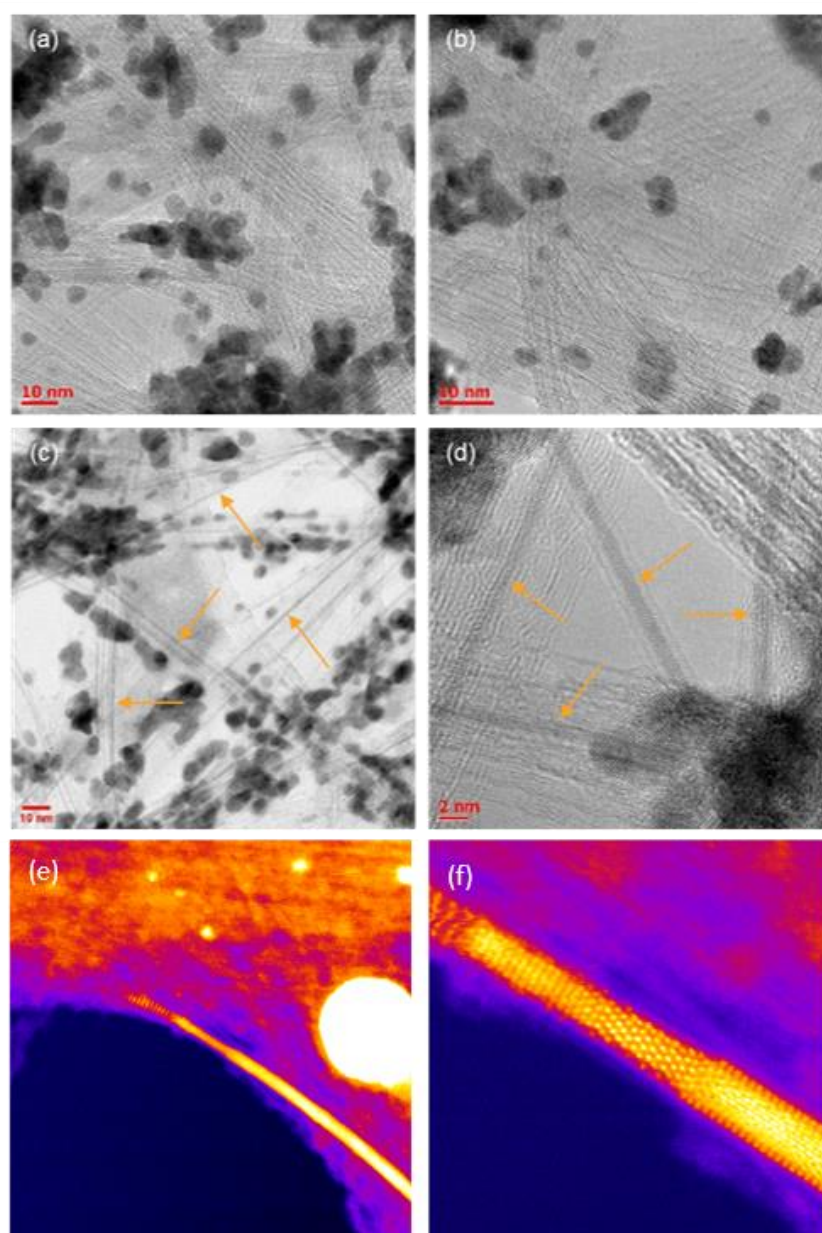
Figure 6. TEM images of SWCNT films doped with 15 mmol L^{-1} HAuCl₄ ethanol solution: without preliminary thermal treatment (a); pre-treatment at 300 ℃ (b) and 400 ℃ (c and d). Arrows

indicate SWCNTs filled with the metallic Au phase. STEM images of 15 mmol L^{-1} $HAuCl_4$-doped opened SWCNTs with encapsulated gold nanowires (e and f).

Figure 6e,f show a gold wire at the edge of a nanotube bundle that precisely follows the structure of the SWCNTs, and thus serves as strong evidence for their endohedral nature. During *in situ* measurements, the diffusion of gold atoms within the nanotube is observed; at 60 keV in a pseudo-elastic scattering from Au atoms, the electron energy reaches up to ~0.9 eV, which may overcome the cohesive energy at the disordered edge and release atoms. The diffusion of carbon and released Au atoms within the tube is observed, imparting a smeared-out contrast confined along the nanotube (Figure A3).

3.1.4. Evaluation of the doping mechanism

To explain the higher doping efficiency of treated nanotubes, we have evaluated changes by measuring OCP of SWCNT films immersed into the $HAuCl_4$ solution. A general trend related to OCP transients is illustrated in Figure 7a recorded for pristine and treated at 350 °C SWCNT films immersed into ethanol solutions with 7.5 and 60 mmol L^{-1} $HAuCl_4$ concentrations. We observe that all OCPs increase until they are stabilized after *ca.* 1600 s (Figure A4). These potential transients indicate the appearance of the electron transfer processes, *i.e.* the discharge process. In Figure 7b, steady-state potentials reached at 1600 s are presented as functions of dopant concentration.
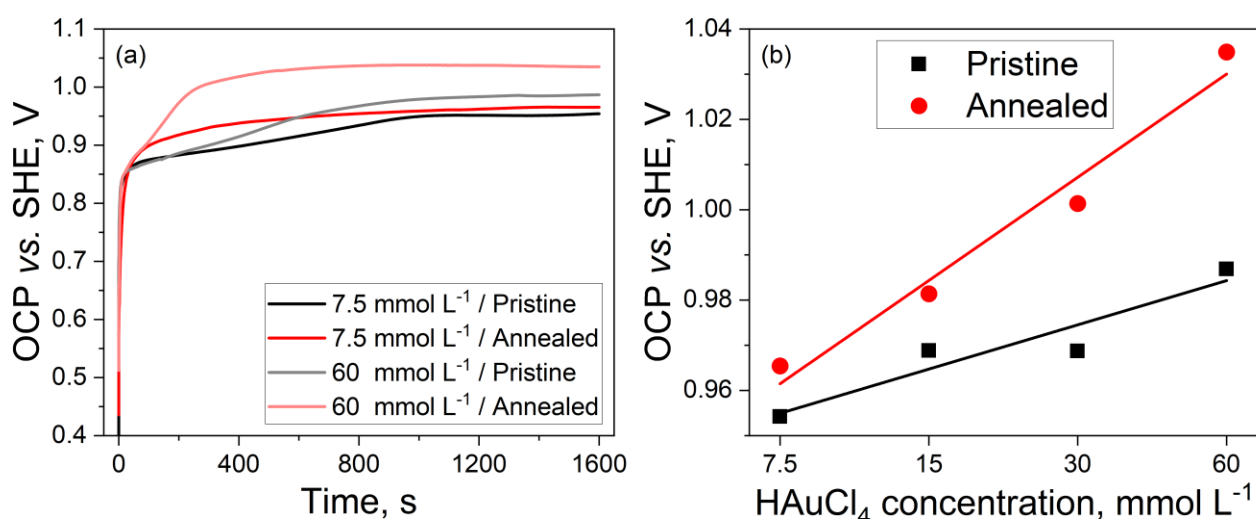
Figure 7. OCP transients of pristine (black, gray) and treated at 350 °C (red, light red) SWCNTs recorded in 7.5 (dark colors) and 60 mmol L^{-1} (light colors) $HAuCl_4$ solutions (a). Concentration dependence of OCP values at 1600 s for 7.5, 15, 30 and 60 mmol L^{-1} $HAuCl_4$ solutions (b).

From Figure 7a and b, we can observe that the equilibrium potential of the treated SWCNT film in comparison to the pristine ones becomes 11 and 48 mV greater for doping with 7.5 and 60 mmol L^{-1} HAuCl₄ solutions, respectively. The more positive potential indicates the more efficient withdrawal of electrons from SWCNTs or more efficient doping. The potential scale is presented *versus* the standard hydrogen electrode (SHE).

When the SWCNT film is in contact with the HAuCl₄ ethanol solution, several charge-transfer involving half-reactions (Table 1) occur on the electrode [142]. From this set of equilibria, we see that monovalent gold chloride complexes coexist with trivalent gold chloride anions and metallic gold at the SWCNT film surface; thus these [AuCl₂]⁻ ions can be formed *via* [AuCl₄]⁻ reduction and Au⁰ oxidation and may play the role of doping mechanism intermediate. Despite metastable behavior of [AuCl₂]⁻ complexes in chloride solutions and their tendency of disproportionation at high concentrations, [143] in the studied system at the equilibrium ($E_{b1} = E_{b2} = E_{b3}$), ions of monovalent gold complexes should exist in small concentrations in solutions. If we compare standard electrode potential values of [AuCl₄]⁻ and [AuCl₂]⁻ reduction to metallic gold, we will see that the latter has higher E^o. This means that chloride complexes of monovalent gold have greater electron acceptor ability than trivalent gold ions and behave as even stronger *p*-dopants.

Table 1. Reactions occurring at the SWCNT film when it is in contact with the doping solution, their standard electrode potentials, and equations for electrode potential

	Half-reaction	Standard electrode potential *vs.* SHE / V	Electrode potential
(a)	$CNT \rightleftharpoons CNT^+ + 1e^-$	$E_a^o = \pm\,0.025$ [3,73]	
(b1)	$[AuCl_4]^- + 3e^- \rightleftharpoons Au^0 + 4Cl^-$	$E_{b1}^o = 1.002$	$E_{b1} = E_{b1}^o + \dfrac{R \cdot T}{3 \cdot F} \cdot \ln \dfrac{C_{[AuCl_4]^-}}{C_{Cl^-}^4}$
(b2)	$[AuCl_4]^- + 2e^-$ $\rightleftharpoons [AuCl_2]^- + 2Cl^-$	$E_{b2}^o = 0.926$	$E_{b2} = E_{b2}^o + \dfrac{R \cdot T}{2 \cdot F}$ $\cdot \ln \dfrac{C_{[AuCl_4]^-}}{C_{[AuCl_2]^-} \cdot C_{Cl^-}^2}$
(b3)	$[AuCl_2]^- + 1e^- \rightleftharpoons Au^0 + 2Cl^-$	$E_{b3}^o = 1.154$	$E_{b3} = E_{b3}^o + \dfrac{R \cdot T}{1 \cdot F} \cdot \ln \dfrac{C_{[AuCl_2]^-}}{C_{Cl^-}^2}$

To support or refute the role of Au^{1+} species in the higher doping efficiency we accomplished XPS measurements for 15 mmol L^{-1} doped SWCNT films treated at 400 ºC. It showed the presence of Au^{3+} and Au^0 (Figure A5). The spectrum from an Au $4f_{7/2-5/2}$ core level consists of two doublets associated with Au^{3+} ions at 85.9, 89.7 eV, and Au^0 at 83.8, 87.4 eV, respectively. The higher peaks from Au^{3+} indicate that a substantial amount of Au^{3+} remains on the nanotubes in the form of gold chloride.

Additionally, we have carried out a theoretical analysis of their electronic properties for separate cases of either only outer or simultaneous outer and inner doping. Earlier DFT calculations have shown that the *p*-type character of doping is due to the adsorption of $[AuCl_4]^-$ species [148]. We can expect other Au-containing species to participate in the doping process. This led us to the systematic investigation of the influence of several $[AuCl_x]$-based dopants on the electronic structure of the carbon nanotubes. Molecular groups of gold chlorides utilized in calculations were taken from the crystal structure of Au (III) [149] and Au(I) [150] chlorides, while pure Au nanorods were cut from fcc bulk gold. SWCNTs of (10,10) chirality were chosen as a model nanotube to be investigated.
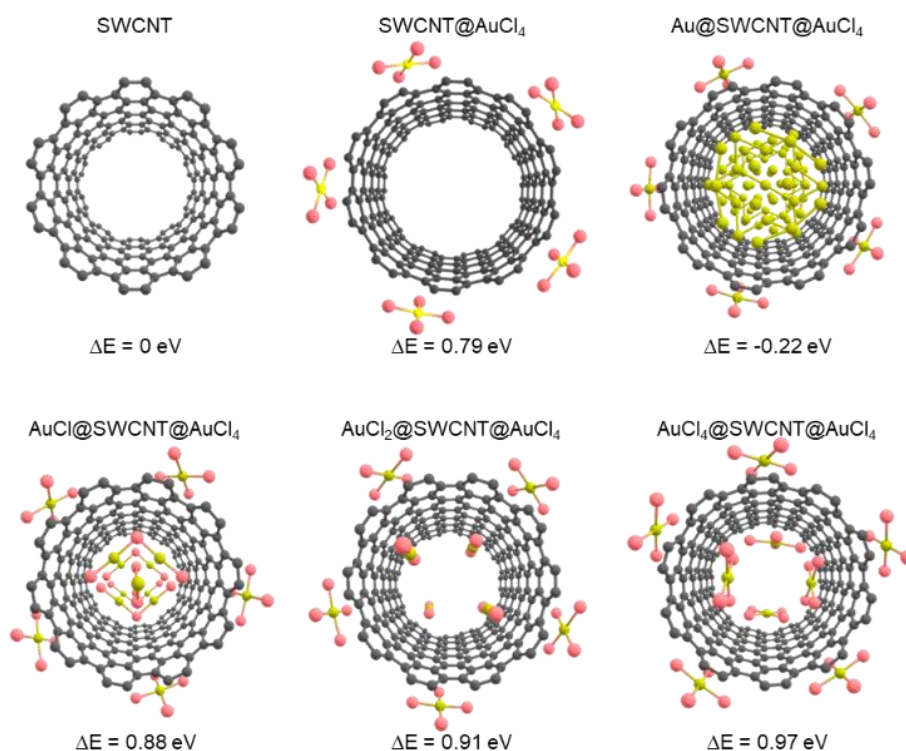
Figure 8. Atomic structures of pristine SWCNT (10,10), doped outside, and doped both inside and outside with different $[AuCl_x]$ dopants. The corresponding Fermi level shift is indicated below each structure. Grey, pink and yellow balls denote carbon, chlorine, and gold atoms, respectively.

Calculations (Figure 8 and Figure A6) show that SWCNTs doped only from the outside (SWCNT@AuCl$_4$) demonstrate a significant Fermi level downshift of 0.79 eV, characterizing *p*-type doping. Simultaneously, further incorporation of Au nanowires into SWCNTs leads to the charge density transfer from the nanowire to SWCNTs and a 0.22 eV Fermi level general shift, corresponding to *n*-type doping. However, there is no significant effect on the charge transfer between SWCNTs and Au nanoparticles present on the nanotube surface (Figure 6c).

In the case of bilateral doping of [AuCl$_4$]$^-$, the largest SWCNT Fermi level downshift to 0.97 eV is observed. This indicates the more efficient *p*-type doping when compared to the sample doped only from the outer surface, reflecting the efficient doping of opened SWCNTs.

Therefore, we can conclude that more efficient doping of heat-treated SWCNTs when compared to the pristine ones is confirmed by the OCP transient measurements, although it stems most likely from bilateral character of doping than from participation of other redox active species as [AuCl$_2$]$^-$ that was supported by XPS measurements and DFT calculation.

3.2. Electrochemical opening for SWCNT filling

3.2.1. Electrochemical treatment

During the pre-treatment cycling we observe the anodic current vanishing after 15 cycles that reflects the electrochemical stripping of iron nanoparticles, *i.e.* SWCNT growth catalyst, exposed to the electrolyte and ion diffusion to bulk of the electrolyte (Figure A7). Such behavior of SWCNT film coincide with the results reported earlier in [151]. The slightly tilted rectangle shape of the current-potential curve by the end of pre-treatment is well-known shape for the SWCNT electrodes and illustrates the process of charging and discharging of electrical double layer (EDL).

There are several processes expected to happen at the SWCNT film electrode. Some of them originate from the presence of residue iron nanoparticles, while others are redox processes related to carbon. To distinguish them, we compared the as-synthesized SWCNT film (*SWCNT-DH*) with the iron-free film (*SWCNT-woFe*). Figure 9 shows CVs of the as-synthesized and iron-free SWCNT films treated at UVP = 1.3 V. They represent the current density as a function of the electrode potential showed for a small number of initial cycles (1, 3, 6 and 10) and for longer treatment (10, 30, 60 and 100 cycles).

Although, CVs of the *SWCNT-DH* film containing iron nanoparticles have clear difference when compared to the ones of the *SWCNT-woFe* film, they still have common features that demonstrate quite small current densities but still are distinguishable (Figure 9a,c insets). First is a pairs of reversible peaks **a$_1$/c$_1$** located near 0.685 and 0.653 V correspondingly and observable for both iron-free and pristine

SWCNT films electrochemically treated at all studied UVPs. Pair of peaks a_1/c_1 is known for carbon nanomaterials and being usually attributed to the OCFGs redox processes, namely hydroxyl/carbonyl ($C - O / C = O$) and carbonyl/carboxyl ($C = O / COOH$) functional groups transformations [152–155]. Potentials obtained in this research are in a good agreement with potentials reported in literature. However, Kobets *et al.* [156] reported particular pH dependent potentials for $C - O / C = O$ and $C = O / COOH$ transformations separately for reduced graphene oxide, where $C = O / COOH$ process has significantly lower potential than $C - O / C = O$ (~300 mV). These reactions could be considered as a two-step system with $E_{C=O/COOH} - E_{C-O/C=O} < 180$ mV. Hence one could expect single wave with lower a_1/c_1 peak separation (~29.5 mV) and potential between single potentials of both processes instead of two separate pairs of peaks [157]. It conforms well to the experimental observation of single peak pair with peak separation ~32 mV. Second feature common for iron-free and pristine SWCNT films is a pair of peaks a_2/c_2 located at ~0.773 and ~0.765 V. This feature should be most probably related to carbon-involving process, although the specific process is hard to unambiguously declare.

When compared to the iron-free film the pristine has additional peaks: anodic peak (or two peaks such as for treatment at UVP = 1.3 V) a_3 located close to 0.389 V appearing at the reverse scan, pair of peaks a_4/c_4 (near 0.514 V) with extensive cathodic current density during initial cycles and anodic a_5 at ~0.914 V. All of these features current density depend on the UVP applied for electrochemical treatment and also depend on the cycle number. Namely, they lose current density with cycling until either complete vanishing by 10-15 cycle (a_3 and a_5) or stabilization with the sustainable shape (a_4/c_4) as shown in Figures A8-A9. Presence of these features observed only for pristine films containing iron from the SWCNT synthesis, combined with their similar behavior in response to cycling and UVP applied and significant changes up to 10-15 cycle confirm that these peaks are due to the iron-related processes. Indeed, Heras *et al.* [151] reported stripping of iron from the nanotube films in acidic solution under potentiodynamic electrochemical treatment expressed in the anodic peak close to 0.12 V *vs.* Ag|AgCl$_{(sat)}$ electrode, that corresponds to the ~0.36 V *vs.* RHE in the 0.5 mol L^{-1} H$_2$SO$_4$ electrolyte utilized in this research. Therefore, we attribute a_3 peak at the reverse potential sweep to the oxidation of the metallic iron just exposed to the electrolyte after cap removal during the prior anodic sweep. Reversible pair of peaks a_4/c_4 with extensive initial cathodic peak should be attributed to the Fe^{3+}/Fe^{2+} redox reaction, illustrating high initial concentration of Fe^{3+} ions in the vicinity of the SWCNT film after initial anodic sweeps. Even though we cannot clearly attribute a_5 feature to the specific redox process, its presence in pristine SWCNTs at the initial cycles only leads to the conclusion that it illustrates redox process involving iron. The fact that its peak current on anodic sweep correlates with Fe^{3+} reduction current (c_4) feature a_5 most probably displays end caps removal coupled with encapsulated iron oxidation.
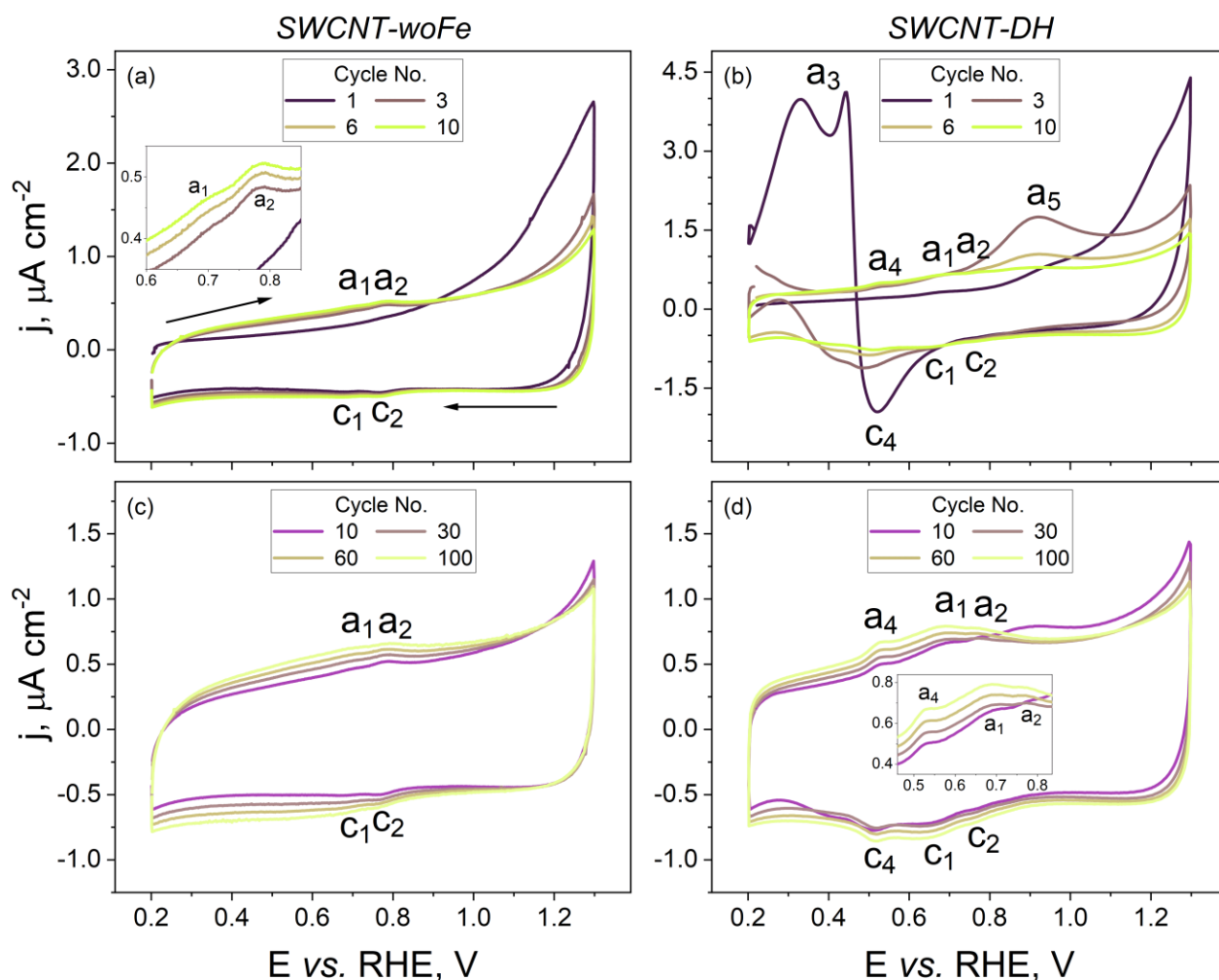
Figure 9. CV curves for the electrochemical treatment of the *SWCNT-woFe* (a,c) and *SWCNT-DH* (b,d) films at UVP = 1.3 V. The top figures display curves for a small number of initial cycles (1, 3, 6 and 10), while bottom for longer treatment (10, 30, 60 and 100).

The CV curves indicating only non-faradaic processes were observed for last pre-treatment cycles (Figure A7) suggesting an absence of iron exposed to the electrolyte by the beginning of the treatment. Since during the treatment we observe peaks reflecting the processes related to the initially encapsulated iron, we can conclude that opening of SWCNT channels starts when UVP = 0.9 V, which facilitates exposing encapsulated iron to the electrolyte.

3.2.2. Structural evaluation

To evaluate the structural changes in the SWCNTs, we acquired Raman spectra. The spectra of SWCNT films (Figure 10a) show so-called radial-breathing mode (RBM) in the region $100\text{-}200\,cm^{-1}$, G-mode (at $1595\,cm^{-1}$) indicating symmetric planar vibrations of carbon atoms in the lattice, D-mode (at $1342\,cm^{-1}$) that reveal vibrations of carbon atoms in sp^2 defects, and 2D-mode that is the overtone of

D-mode (2774 cm^{-1}) [128]. The intensity ratio of G to D-mode (I$_G$/I$_D$) is commonly used as the figure of merit of the graphitic nanostructures [158]. In this regard, we observe that electrochemical treatment of the SWCNT film causes minor changes in the I$_G$/I$_D$ ratio that stays in the range from 71 to 84 (Figure 10). However, slightly higher values for the electrochemically treated SWCNT films might reveal the removal of amorphous carbonaceous impurities. The SWCNT film treated at stronger conditions (UVP = 1.7 V) exhibit I$_G$/I$_D$ ratio decrease down to 61 manifesting the formation of structural defects. RBM is another mode that is sensitive to structural defects, in particular to the SWCNT wall oxidative corrosion [57,159,160]. In Figure 10b we observe that two broad peaks of RBM slightly changes for reference sample when compared to *SWCNT-DH* film. Additional slight decrease in peaks intensity happens when UVPs from 0.7 to 1.1 V are applied, although spectra are very similar to each other. Following UVP increase causes RBM mode peaks to gradually lose their intensity. It implies that SWCNT wall oxidative corrosion happens in two stages. First stage occurring at UVPs ≤ 1.1 V is associated with minor SWCNT wall defect formation, while the second, beginning at UVPs > 1.1 V, implies their further possible growth and additional formation.
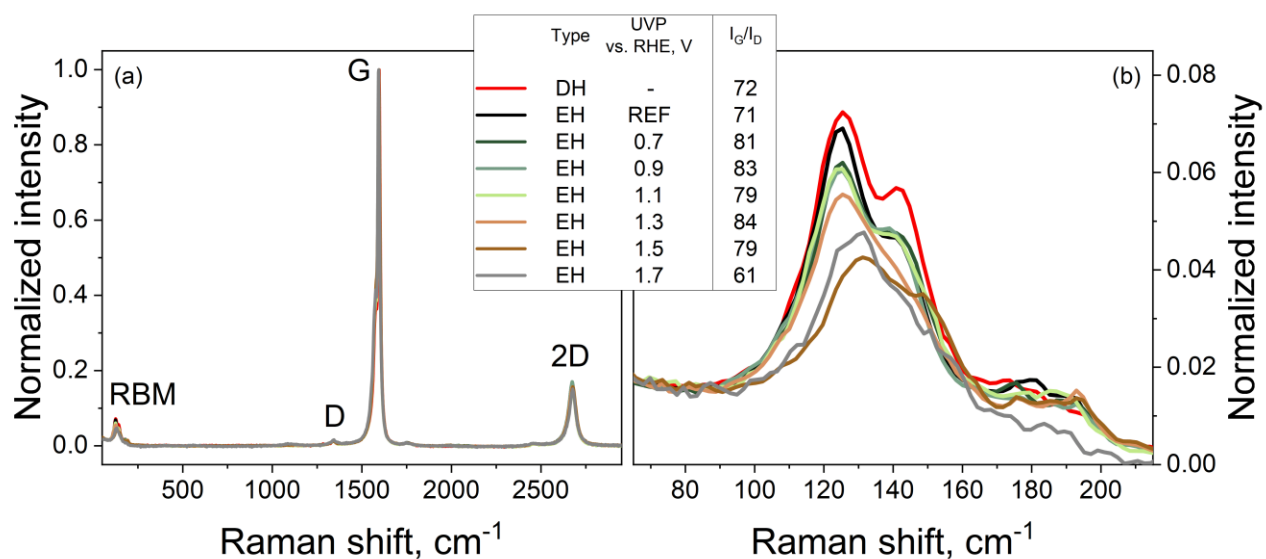
Figure 10. Survey Raman spectra (a) and RBM-mode (b) for *SWCNT-EH* films treated at different UVPs in comparison to the *SWCNT-DH* film.

We have also tracked the sheet resistance of SWCNT films for the evaluation of the SWCNT structural changes. The sheet resistance of the SWNCT film is dependent on combination of such factors as Schottky barriers between the nanotubes, degree of adsorption doping, purity and concentration of defects in SWCNTs. Table 2 contains the data on the sheet resistance of *SWCNT-DH* and *SWCNT-EH*

films, depending on the UVP applied, along with the ratio of the values. We observe that the sheet resistance of the SWCNT films decreases after the treatment, which is caused by the adsorption doping of SWCNTs with sulfuric acid and adsorbed oxygen formed during the electrochemical treatment [138,161]. This results in Fermi level shift (Figure A10) and decreases Schottky barriers between metallic and semiconducting SWCNTs. Moreover, we observe a decrease in the *SWCNT-EH* to *SWCNT-DH* films' sheet resistance ratio with increase of the UVP up to 1.3 V. It happens because of the longer exposure of SWCNT film to the sulfuric acid, and stronger effect of adsorbed oxygen whose evolution is more extensive at higher potentials. Additionally, some amount of sulfuric acid might stay within the film even after heating in the vacuum oven causing irreversible adsorption doping. In contrast, when we apply the UVP ≥ 1.5 V sheet resistance starts growing, likely exhibiting stronger electrons scattering on the structural defects. Therefore, taking into account complex nature of the sheet resistance changes we could expect massive structural defect formation at UVPs > 1.3 V.

Table 2. Sheet resistance values for *SWCNT-DH* and *SWCNT-EH* films and ratio of those for films treated at different UVPs.

UVP *vs.* **RHE / V**	$R_S^{SWCNT-DH}$ / Ω sq^{-1}	$R_S^{SWCNT-EH}$ / Ω sq^{-1}	$\dfrac{R_S^{SWCNT-EH}}{R_S^{SWCNT-DH}}$
Reference	360	287	0.80
0.7	425	299	0.70
0.9	431	273	0.63
1.1	358	229	0.64
1.3	408	193	0.47
1.5	351	226	0.64
1.7	470	1067	2.27

Assessment of carbon atoms' chemical state was done using XPS spectroscopy (Figure A11). C1s XPS spectra of *SWCNT-EH* films were analyzed by deconvolution to six components (Figure 11). Peak located at binding energy of ~284.5 eV was attributed to the sp^2-hybridyzed (C=C) carbon representing SWCNTs intact structure, while peak at ~285.4 eV was assigned to be sp^3-hybridyzed (C-C) carbon reflecting presence of disordered carbon [162]. Peaks representing oxygen containing functional groups (OCFGs) are located in the range ~286.5-289.1 eV. In particular peak at ~286.5 eV

show presence of hydroxyl and epoxy (C-O) functional groups, peak at ~288.0 reflect carbonyl (C=O) bonds and peak at ~289.1 eV is associated with carboxyl (O-C=O) functionalization [163]. The sixth peak at ~290.6 eV binding energy correspond to the π-π* shake-up satellite indicating conductive aromatic structure of the SWCNTs [164]. Deconvolution peak model results in envelope residual standard deviation from the obtained data (0.963-1.209) close enough to the residual standard deviation of the background 1.126, confirming quality of fit (Table A1).
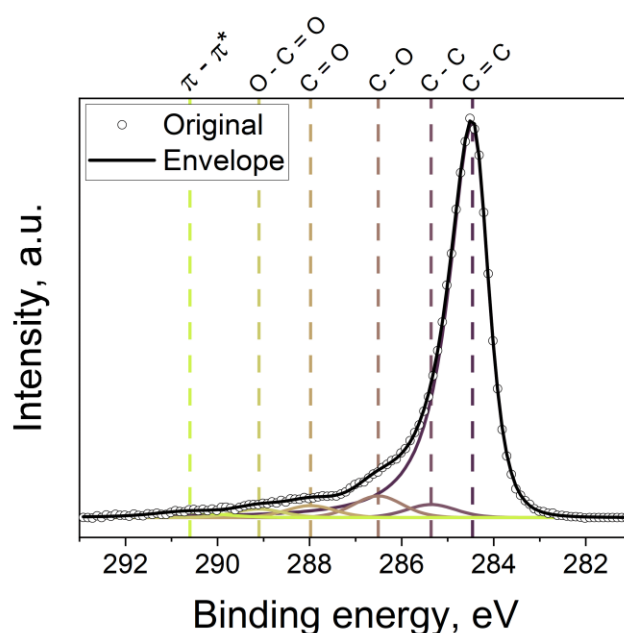
Figure 11. High-resolution C1s XPS spectra for *SWCNT-EH* film treated at UVP = 1.3 V fitted with six peaks representing various carbon chemical states.

Table 3 contains the data of sp^2- and sp^3-hybridyzed carbon content in the sample coupled with oxygen containing functional groups (OCFGs) concentration obtained by the analysis of C1s core-level spectra of *SWCNT-EH* films (detailed data in Table A1). With the application of the electrochemical treatment we observe growth of the atomic concentration of OCFGs along with oxygen that implies that the material undergoes chemical functionalization. Besides, we observe general trend to the decrease of peak area representing sp^2-hybridyzed carbon atoms, reflecting gradual destruction of sp^2 SWCNT conjugated system, so we should expect the formation of defects on the nanotube walls. Distinguishable from the others is the SWCNT film sample treated at UVP = 1.1 V. It displays the sp^2-hybridyzed carbon peak area closest to the reference sample, while the sp^3-hybridyzed carbon peak area is the smallest throughout all samples. This reflects oxidation that affects sp^3-hybridyzed carbon and may also involve oxidation of transitionally hybridized end-cap carbon atoms.

Table 3. Concentration of functional groups and their standard deviations from C1s fitted spectra for *SWCNT-EH* films compared to the reference film.

UVP *vs.* RHE / V	at.% C=C	at.% C-C	at.% OCFGs
Reference	91.3 ± 1.4	1.8 ± 1.2	5.4 ± 0.9
0.7	89.5 ± 1.4	1.6 ± 1.0	7.2 ± 0.8
0.9	89.8 ± 1.4	2.5 ± 0.9	6.1 ± 1.0
1.1	90.1 ± 1.4	0.6 ± 0.8	7.6 ± 0.8
1.3	86.2 ± 1.3	2.9 ± 1.0	9.4 ± 0.8
1.5	88.1 ± 1.4	3.4 ± 1.0	7.3 ± 0.8

3.2.3. Filling of SWCNTs

To assess filling efficiency, we treated SWCNT films with ethanol solution of $HAuCl_4$ to fill internal channels with gold nanowires (NWs). When we immerse *SWCNT-EH* films into the solution, the latter penetrates into the opened SWCNT cavities under capillary forces. Due to the high positive redox potential of the $[AuCl_4]^-$ anion (1.002 V *vs.* SHE) it can withdraw electrons from SWCNTs [73]. Thus, when SWCNT film is in the contact with the filler solution, gold spontaneously reduces in the form of encapsulated metallic NWs and nanoparticles on the surface of nanotubes.

The filling efficiency of the SWCNT film could be estimated by measuring the amount of the filled SWCNT channels in a unit area of the SWCNT film. Therefore for filling evaluation we used specific length of encapsulated NWs (the NWs length per unit film area), which directly depends on two parameters: first, the mean length of the encapsulated NWs; second, the number of NWs per unit area of a SWCNT film. Both the NW length distribution and its areal concentration depends on the processes that happen during the treatment procedure. Those should include growth of existing defects, nucleation of new defects on the SWCNT walls and the cap removal, *i.e.*, internal channels opening. Based on the dark-field STEM images (Figure 12c-e) of the *SWCNT-EH* films doped with $HAuCl_4$ solution we built the gold NW length distribution curves depending on the applied UVP and calculated mean values of the NW length (Figure 12a). Besides, the area under each distribution curve is proportional to the number of NWs per unit SWCNT film area.
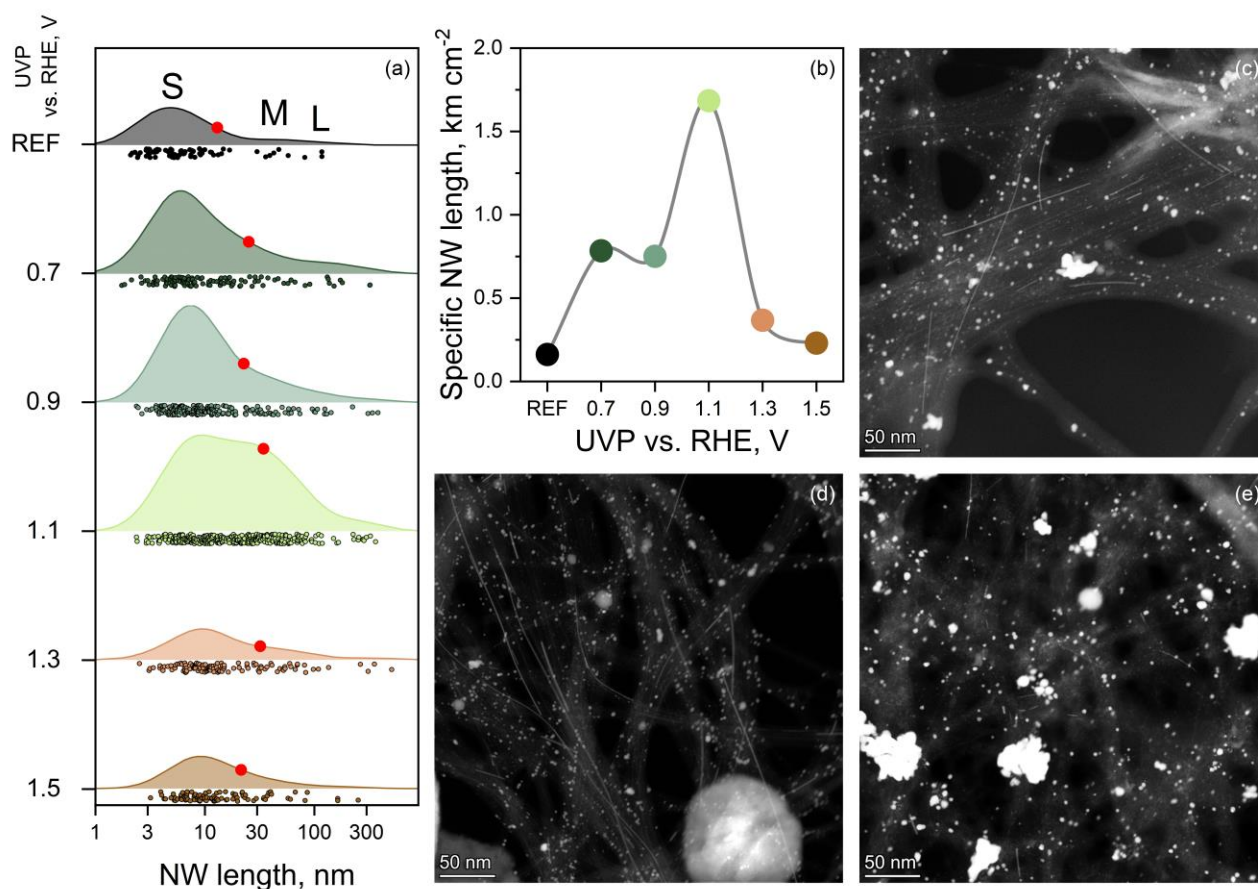
Figure 12. Length distribution and mean length of Au nanowires (red circles) in *SWCNT-EH* films filled in the HAuCl₄ ethanol solution (a). Area under each curve is proportional to the number of NWs. The length of Au nanowires per a unit f-SWCNT film area prepared by means of the electrochemical treatment at different UVPs (b). TEM images of *SWCNT-EH* films treated at UVP = 0.7 V (c), 1.1 V (d) and 1.5 V (e) and filled in the HAuCl₄ ethanol solution.

All the NW length distribution curves display occurrence frequency of NWs with a particular length. Produced f-SWCNT exhibit three-modal log-normal distribution with: (1) a distinguishable mode at small NW length, which peak position secured in the region 5-10 nm, denoted as S, (2) an emerging mode with peak value close to medium NW length of 38 nm (M), (3) the distribution tale of NWs longer than ~100 nm (L). Molecular dynamics simulations imply the strong dependence of the solution flow in SWCNT inner cavities on the presence of structural defects and functional groups [4,22–26], thus it is reasonable to expect constraining character of defects on the NWs formation. Therefore, the S-mode should reflect short NWs formed by filling through the wall defect, since they are not favorable for high solution penetration rate, but still have to allow such phenomena. The M-mode should

be attributed to the NWs encapsulated by means of filling from the de-capped or initially open SWCNT end until solution reaches the nearest side-opening or functional defect located relatively close to the open end. The L-branch most probably indicates the NWs encapsulated from the SWCNT open end to the closest structural defect located relatively far from it. This should be expected to be quite rare case. Correspondingly, a few examples of such long NWs were observed for the most of samples.

The application of treatment at UVP = 0.7 V changes significantly both, the distribution curve shape and NW number. Firstly, in the length distribution we observe shift of the S-mode to the slightly longer NWs that illustrate the moderate growth of wall defects, allowing higher rate of solution entering cavities through them. This behavior is common for the samples treated at UVP ≤ 1.3 V. Secondly, we observe 2.5 folder NW number increase when compared to the reference sample. It indicates the nanotube wall defect formation coupled with the beginning of the SWCNT end-cap removal process. The treatment at UVP = 0.9 V results in quite similar distribution and slightly higher NW number due to the same processes. The NW length distribution for the films treated at UVP = 1.1 V is outstanding from the others. Such dramatic rise of the occurrence frequency of medium-sized and long NWs correspond to the treatment favoring the efficient end-cap removal. However, nucleation process increases the concentration of defects on the nanotubes' walls, thus most of filled from the open-end NWs belong to the M-mode. As a result, we observe the longest nanowires and their highest areal concentration, leading to the best filling efficiency of ~1680 m cm^{-2} (Figure 12b). At UVPs ≥ 1.3 V, the drastic decrease in the NW number is observed coupled with the decrease of M to S-mode ratio. Such drop should be explained by formation of too excessive defects and their rapid growth, so their quantity and size become unfavorable for the filling. Namely, neighboring defects might couple in a single larger defect diminishing number of NWs.

3.3. PANI deposition for flexible supercapacitors

3.3.1. Synthesis of SWCNT/PANI composite materials

Fabrication of free-standing SWCNT/PANI structures includes a transfer of a SWCNT film onto a PMMA frame followed by electrochemical synthesis of PANI and subsequent drying as schematically depicted in Figure 13a along with the images of corresponding samples. During the synthesis, we identified the strong influence of SWCNT film sheet resistance on PANI deposition and evaluated the PANI growth *versus* the total charge consumed per cycle. Sheet resistance values measured for SWCNT80, SWCNT90, and SWCNT95 films are 106 ± 3, 183 ± 3, and 478 ± 16 Ω sq^{-1}, respectively. Figure 13b shows the exemplary CV curves recorded during 70 cycles of PANI deposition on a SWCNT95 film where at least two peaks can be identified. The first peak, denoted as *a1*, is located at

212 mV on the anodic sweep. It corresponds to the oxidation of the leucoemeraldine non-conducting PANI form to the emeraldine (Figure A12 and A13). The second peak, *c1*, located at 103 mV on the cathodic sweep of the curve corresponds to the transition of PANI from the emeraldine to pernigraniline state [119,165]. These redox processes are accompanied by the addition or elimination of protons, which also hints that PANI accumulates energy most efficiently in acidic media [119]. Notably, the maximal conductivity of PANI is achieved at a doping degree of 50 %, which is attributed to PANI in the form of emeraldine salt, to be up to 10^3 S cm^{-1} while it is about 10^{-2} S cm^{-1} for emeraldine base [166] (Figure A14).

The *a1* and *c1* peaks are weakly manifested on the CV curves at the beginning of the cycling. Starting from the 6th and up to the 30th cycle, we have observed the moderate growth of peaks' current favored by autocatalytic type of reactions, *i.e.* accelerated by the appearance of nucleates [167]. After 20 deposition cycles, the position of the *a1* peak shifts from 305 mV to 420 mV with a corresponded noticeable increase in the current. Following the 35th cycle, the growth is expected to be rather uniform with a linear dependence of consumed charge *versus* cycle number. This should be associated with the growth of polymer chains [168]. Peak potentials continue shifting with a cycle number, reaching 540 mV and 10 mV at the 70th cycle for *a1* and *c1* peaks, respectively. We observed similar trends for the electrodeposition of PANI on SWCNT90 and SWCNT80 films (Figure A15). Peak shift could be associated with both increasing thicknesses of the growing PANI layer and elongation of the PANI chains [47].

The normalized charge consumed per PANI synthesis cycle *versus* the cycle number is plotted in Figure 13c to evaluate the influence of the SWCNT sheet resistance on the PANI growth. Generation of aniline radical-cations in the near-surface layer of the electrode occurs during the first 10-15 cycles. Then dimeric, trimeric, and oligomeric anilines and products of their oxidation are being formed up to about the 40th cycle producing small quantities of PANI on the SWCNT surface. Moreover, electrochemical characteristics of the composite materials prepared with 20-35 deposition cycles should be rather similar to characteristics of the pristine SWCNT films and do not demonstrate redox reactions characteristic for PANI due to the small amount of the polymer on the SWCNT surface. Especially it is observed for SWCNT80. These films are characterized by the higher normalized charge over the first 30 cycles due to the higher specific surface area of the film (Figure A16).
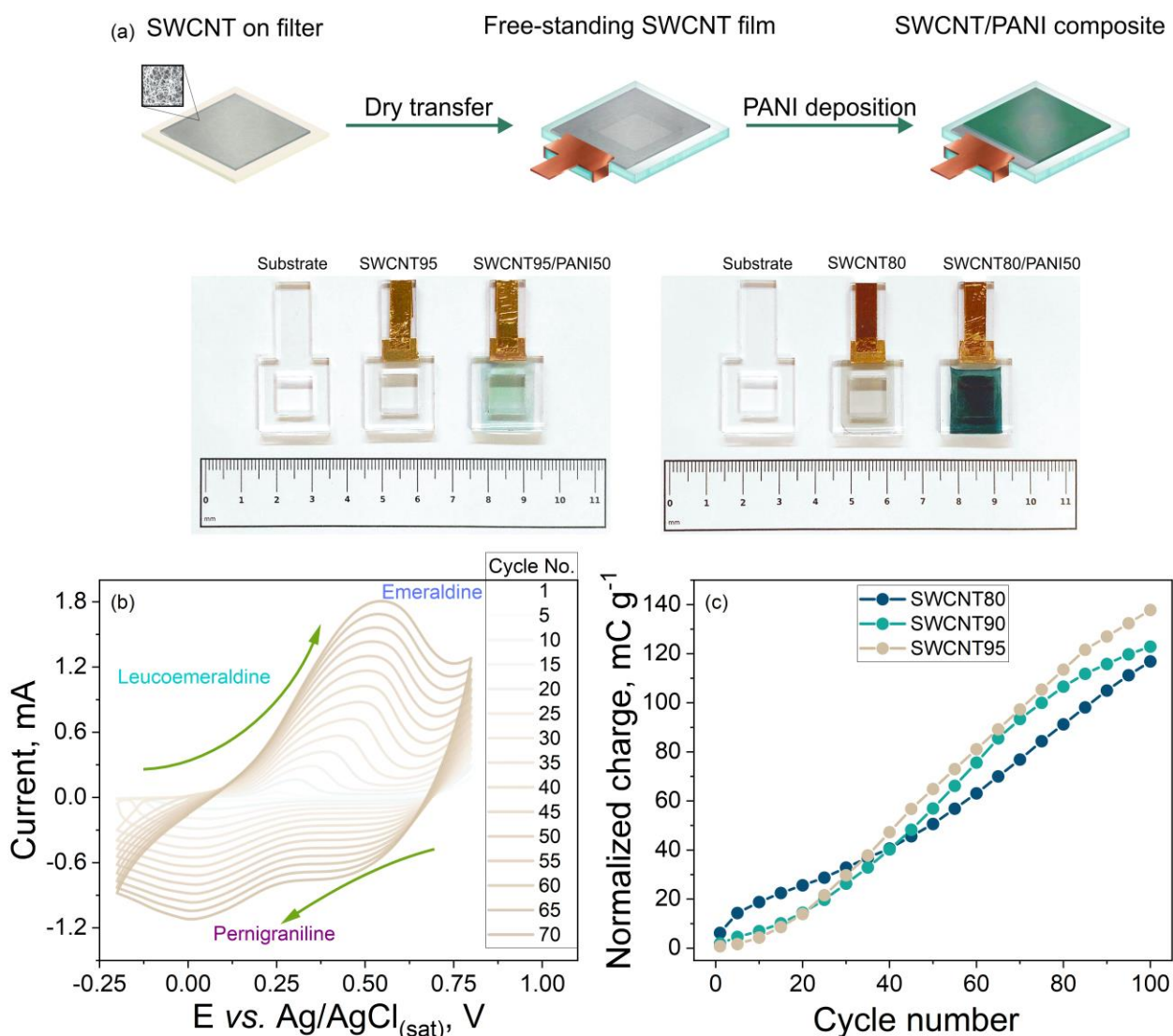
Figure 13. Fabrication and characterization of the free-standing SWCNT/PANI composites. Schematic illustration of the SWCNT/PANI composite preparation, images of the substrates, free-standing SWCNT95, and SWCNT80, and composites SWCNT95/PANI50 and SWCNT80/PANI50 (a). CV curves of electrochemical PANI polymerization on a free-standing SWCNT95 film recorded over 70 cycles at 20 mV s^{-1} scan rate (b). Normalized charge consumed per cycle for PANI electrodeposition on the SWCNT films with transmittance 80, 90 and 95 % (c).

The amount of the polymer deposited during 40–70 cycles was found to suit the most to assess the pseudocapacitive properties of PANI. Besides, controlling the quantity of the deposited polymer in this range is straightforward due to the linear dependence of charge *versus* cycle number. In this range, the growth behavior of all the samples is similar.

After 70 cycles, we observe a deceleration of the PANI growth indicating a change of polymerization mechanism to the termination stage due to a decrease in the concentration of monomer in the solution, impairment of diffusion with increasing thickness and density of the electrode, side electrochemical reactions [169]. However, even after 100 cycles, polymer growth continues. For evaluation of capacitive properties, we have selected composites synthesized using 40, 50, 60, and 70 deposition cycles, further denoted as PANI40, PANI50, PANI60, and PANI70 because this range has linear charge growth and enables deposition of sufficient but not excessive amounts of PANI. The dependence of the mass of the composite material on the applied number of cycles is presented in Figure 14. The increase in the mass of the composite materials corroborates well with an increase in the cycle number assessed in a linear range of 40-70 cycles.
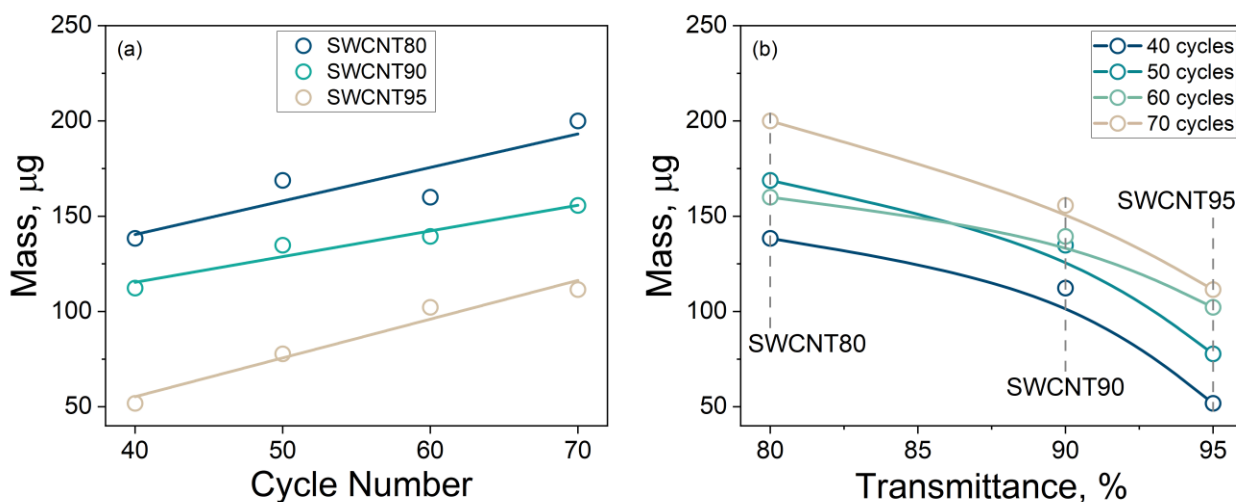
Figure 14. Dependence of the mass of the composite material on the number of PANI electrodeposition cycles (a). Dependence of the mass of the composite material on the SWCNT film transmittance (b). Lines are a guide for an eye.

3.3.2. Structure of the SWCNT/PANI composite materials

A pristine SWCNT film obtained by the aerosol CVD method is represented by randomly oriented distributed nanotubes, as it is shown for an exemplary SWCNT80 film in Figure 15a. A dense PANI layer with no visible gradient of thickness appears at the surface of SWCNT80 already after 40 deposition cycles (Figure 15b, Figure A17). After the 70th deposition cycle, PANI occupies the entire visible surface of the SWCNT80/PANI70 composite and the tubes are noticed at the film cross-section only (Figure 15c, Figure A17). On contrary, we observe polymer deposition mainly in the cavities between SWCNTs in the case of SWCNT95/PANI40 (Figure 15d, Figure A17). A loose structure of the

SWCNT95/PANI40 material depicted at a cut becomes denser with an increase in the number of PANI deposition cycles. In particular, PANI replicates the SWCNT95 film surface when the number of deposition cycles equals 70 (Figure 15e, Figure A17). As noted earlier, thick SWCNT films demonstrate greater conductivity, which leads to a generation of higher concentration of radical-cations in the vicinity of the SWCNT film surface, thus a dense layer of polymer is primarily formed on the surface of the material [168].
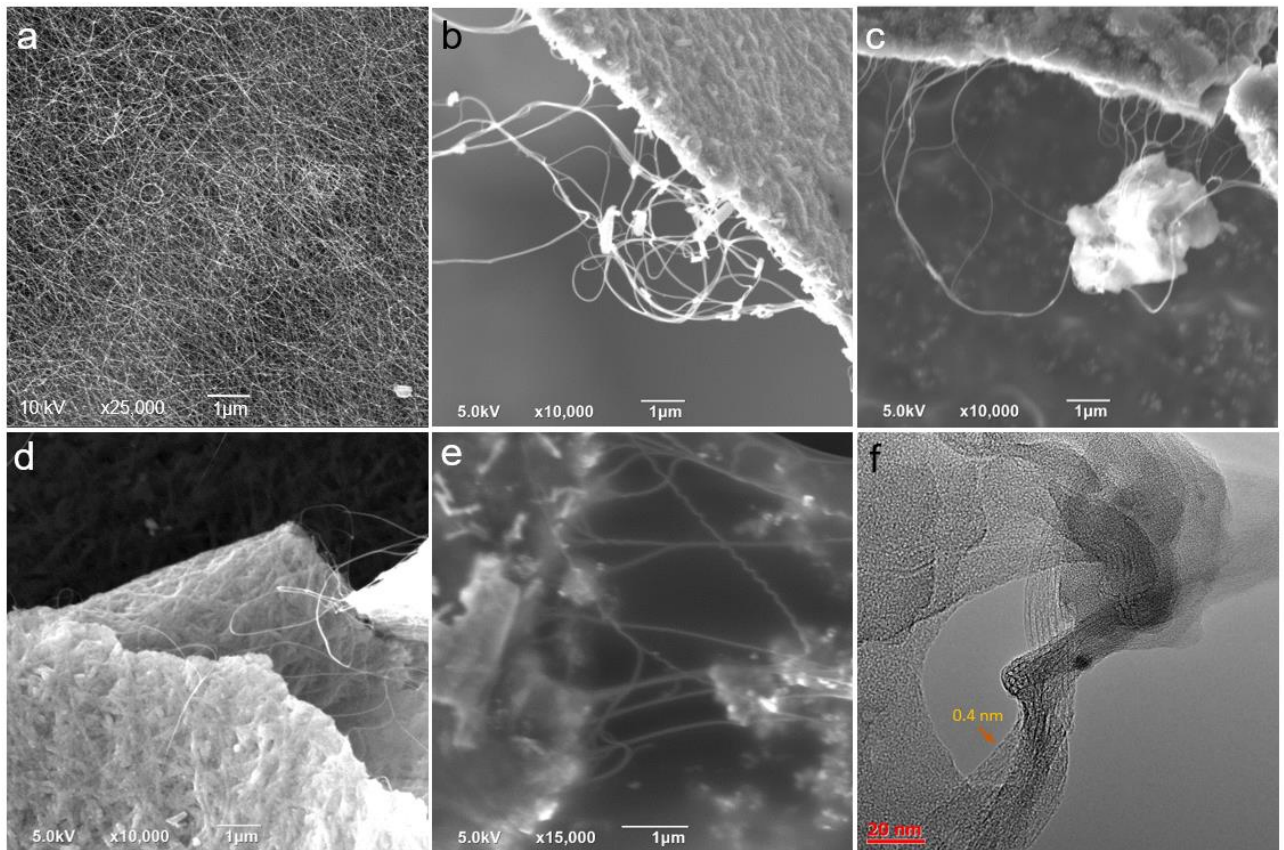
Figure 15. Morphology and structure characterization of the SWCNT/PANI composites. SEM images of the pristine SWCNT80 film (a); SWCNT80/PANI40 composite (b); SWCNT80/PANI70 composite (c); SWCNT95/PANI40 composite (d); SWCNT95/PANI70 composite (e); TEM images of SWCNT90/PANI40 composite film (f).

TEM analysis is conducted to study the dispersion and morphology of SWCNT in a PANI matrix for a sample made of SWCNT with a transmittance of 90 % and 95 % and with 40 cycles of PANI deposition (SWCNT90/PANI40 and SWCNT95/PANI40) as shown in Figure 15f, Figure A17 and A18. The images confirm the uniform distribution of SWCNT in the PANI matrix. According to TEM observations, the deposited PANI has the inclusion of ordered regions of 10–20 nm (Figure 15f,

Figure A17 and A18). Close to the SWCNT surface, PANI has a more ordered layered structure (approaching about 15 atomic layers as calculated from TEM images). However, it is characterized by an amorphous three-dimensional structure in a polymer bulk which is related to specific interactions between PANI and SWCNTs. When a small amount of PANI is deposited, the polymer layers are oriented along the surface of the SWCNT due to van der Waals interactions between the conjugated SWCNT system and aromatic fragments of the polymer [169]. With an increase in the number of layers, van der Waals forces weaken and the polymer is no longer associated with the conjugated SWCNT system; it continues to grow chaotically with the formation of an entangled three-dimensional structure [168]. The main part of the SWCNT90/PANI40 material consists of amorphous PANI agglomerates surrounding SWCNT bundles. In some images (Figure 15f, Figure A18), a well-pronounced PANI/SWCNT crystal structure is observed near the SWCNT surface, while PANI is represented predominantly as an amorphous polymer at a distance from the SWCNT. SWCNT net of 90 % transmittance is denser in the PANI matrix and has larger bundles when compared to 95 % SWCNT film which is related to the larger number of CNTs in pristine films.

Raman spectroscopy was employed for the identification of the functional composition and structure of the samples (Figure 16). All recorded spectra were normalized to the G-mode intensity. A spectrum of pristine SWCNT95 exhibits several typical peaks those Raman shift values are shown in Table A2. An intensive peak at about 1600 cm^{-1} corresponds to the in-plane tangential stretching of the carbon-carbon bonds [170] and is referred to as G-mode in literature [171]. Its appearance is associated with optical vibrations of two adjacent carbon atoms in the nanotube structure [172]. When two or more adjacent carbon atoms deviate from their ideal position (for example, when they are covalently bonded with functional groups) or are removed from the structure, defects arise, and the intensity of G-mode decreases. When it occurs, a peak located at ~1350 cm^{-1} (D-mode) appears in Raman spectra [171]. This peak has a low intensity in spectra of pristine SWCNTs and the obtained composite films. The defectiveness of the pristine films and composites is usually estimated by the G-mode to D-mode intensity ratio (I_G/I_D) [173]. For the SWCNT95 sample, this ratio is more than 100, which corresponds to a low defectiveness, *i.e.* high quality of SWCNTs. The peak observed in the range of 2600–2700 cm^{-1} is the overtone of the D-peak called 2D-mode [172]. This mode is responsible for the joined vibrations of carbon atoms in carbon hexagons [174]. Moreover, its shift and broadening correspond to the doping of SWCNTs [174]. The peak of the 2D-mode is located near 2672 cm^{-1} in the spectrum of the pristine SWCNT95 and has a relative intensity of 0.11. Shift and broadening of that peak occur after deposition of PANI on the SWCNT films, the center of 2D-mode is shifted to ~2677 cm^{-1} and is characterized by maximal intensity value 0.10–0.11. A different trend is observed for the

SWCNT90/PANI70 composite spectrum. The center of the 2D-mode is located near ~2682 cm⁻¹ and with a maximum intensity of 0.11.
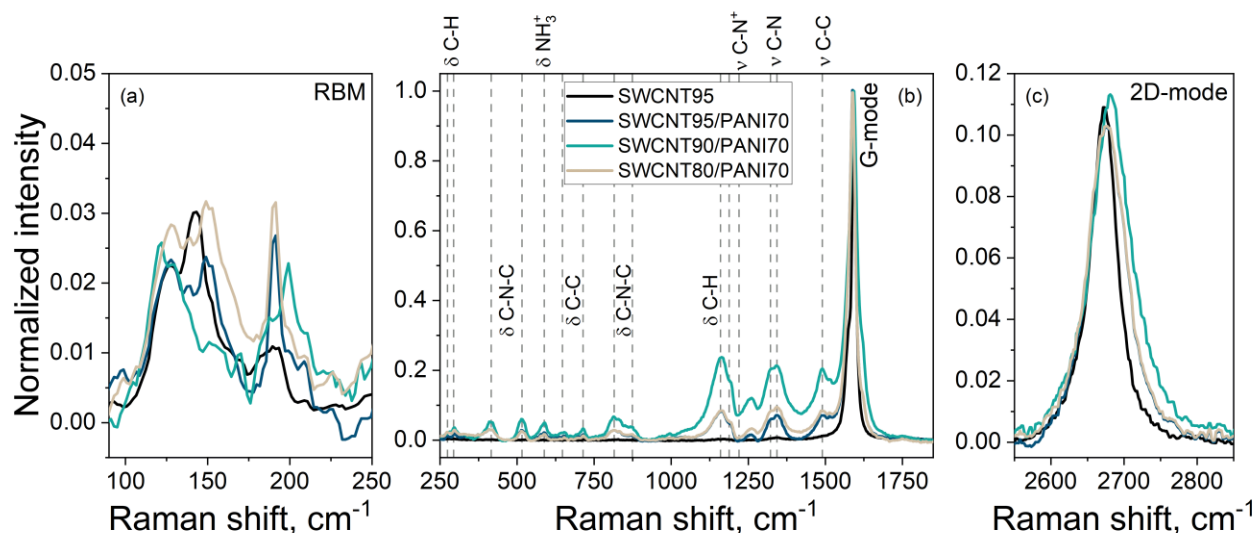
Figure 16. Normalized Raman spectra of the samples SWCNT95, SWCNT95/PANI70, SWCNT90/PANI70, SWCNT80/PANI70 presented in Raman shift ranges: from 90 to 250 cm⁻¹ (a); from 250 to 1850 cm⁻¹ (b); from 2550 to 2850 cm⁻¹ (c).

A slight shift of these peaks after the PANI deposition to higher wavenumbers corresponds to the *n*-doping of SWCNTs by PANI. In addition to the peaks described earlier, a group of low-intensity peaks is observed in the Raman shift range from 90 to 250 cm⁻¹. Those peaks are characteristic for only single- and double-walled CNTs and are known as radial breathing mode (RBM) [175,176].

All the peaks of PANI are located in the range from 250 to 1600 cm⁻¹. The peak at ~1590 cm⁻¹ overlaps with the G-mode of SWCNT and corresponds to the vibrational oscillation of C–C (ν C–C) in benzene rings. The peak at 1490 cm⁻¹ corresponds to the vibration of ν C–C bonds in quinoid rings and identifies the presence of doped PANI structures [177]. Peaks at 1322 and 1220 cm⁻¹ correspond to the ν C–N⁺ and ν C–N vibrations, respectively [177,178]. The peak at 1160 cm⁻¹ corresponds to the δ C–H oscillation in quinoid rings [179]. The peak at 874 cm⁻¹ is attributed to the deformational oscillation of C–N–C (δ C–N–C) and/or deformation of benzene rings in both polaron and bipolaron forms. The peak at 815 cm⁻¹ can be related to the deformations of benzene rings [180]. The two peaks at 714 and 647 cm⁻¹ are characteristic of highly ordered PANI and correspond to the δ C–C vibrations of rings [181]. The peak at 588 cm⁻¹ stems from the deformational vibrations of protonated amine groups. Peaks

at 516 and 416 cm^{-1} correspond to the δ C-N-C out-of-plane vibration and indicate twister conformation of PANI [182]. Two peaks at 294 and 274 cm^{-1} arise because of the δ C–H out-of-plane vibrations.

All the composite samples consist of similar PANI species regardless of the transmittance of films: benzene rings in aromatic and quinoid forms; nitrogen in neutral and positively charge states; polaron and bipolaron quasi-particles. However, in the spectrum of SWCNT90/PANI70, peaks have the highest intensity, which should correspond to rather thick PANI layers on the SWCNT surface [51,183,184]. The presence of charged fragments and polaron/bipolaron quasi-particles in the Raman spectra of the composite materials indicates the deposition of PANI in emeraldine conducting form.

Evaluation of the functional composition and surface concentration of elements of the SWCNT95/PANI40 sample was done using the XPS method. The C1s, O1s, N1s, S2s, and S2p core-level photoemission lines were indicated in the survey spectrum of the SWCNT95/PANI40 sample (Figure A19) as well as C KLL and O KLL edges. The at.% concentrations of C, O, N, and S elements are equal to 79.6, 9.0, 9.0, and 2.4 at.%, respectively. The high amount of O in the sample is related to both its functionalization by oxygen-containing functional groups (OCFG), resulting from the secondary reactions of oxidation of aniline monomer during the synthesis, and the presence of SO_4^{2-} counter-ions. The C:O:N:S ratio in the sample is 1:0.11:0.11:0.03. The C1s spectrum is fitted by five peaks (Figure 17a). The first one is located at BE 284.4 eV which is typical for sp^2-hybrid carbon assigned to the C=C bonds in aromatic rings [185,186]. The second peak at BE 285.3 eV can be ascribed to both C–C and C–N bonds in aromatic PANI units [187] as well as C–C bonds in carbon nanotubes located mostly near edges or defects. The peak located at BE 286.2 eV is specific to hydroxyl OCFG connected with carbon atoms as well as polaronic groups in PANI (C–NH$^+$) [188,189], while the peak located at BE 287.3 eV is related to the carbonyl OCFG [190] and neutral charge C=N fragments in quinoid PANI units [191]. The last peak at BE 289.0 eV is specific to carboxyl OCFG [192] and bipolaronic PANI units [193]. Thus, the C1s spectra of the sample demonstrate that PANI is functionalized by OCFG and can contain both charged and neutral units in aromatic and quinoid forms. The N1s spectrum of the sample proves the presence of PANI units in both charge states and forms (Figure 17b). The peak located at BE 398.3 eV is ascribed to the C=N bonds of quinoid PANI units in a neutral charged state, while the peak at BE 399.5 eV is related to the –NH– bonds of aromatic PANI units in a neutral charged state [194]. The peaks at BE 401.1 and 402.7 eV are assigned to the –NH$^+$– bonds (polaronic structures) in aromatic PANI units and =NH$^+$– bonds (bipolaronic structures) in quinoid ones [187,189,195]. The S2p spectrum of the material consists of one doublet with a distance between centers of peaks of 1.18 eV (Figure 17d). The first and second peaks in doublet are located at BE 168.1 eV (S2p$_{3/2}$) and 169.2 eV (S2p$_{1/2}$), respectively. They can be assigned to the –SO$_3$ groups attached to the polymer units [196] and/or SO_4^{2-} counter ions which are neutralizing charged N species [197]. The O1s high-resolution

spectrum was fitted with four peaks (Figure 17c). The peaks located at BE 531.1, 532.4, and 533.6 eV are specific to carbonyl, carboxyl, and hydroxyl OCFGs, respectively [188,190]. The peak at BE 532.4 eV can also be related to the $-SO_3$ groups and/or SO_4^{2-} counter-ions. The low amount of adsorbed water was additionally found in the O1s spectrum (peak at BE 535.2 eV) [190].
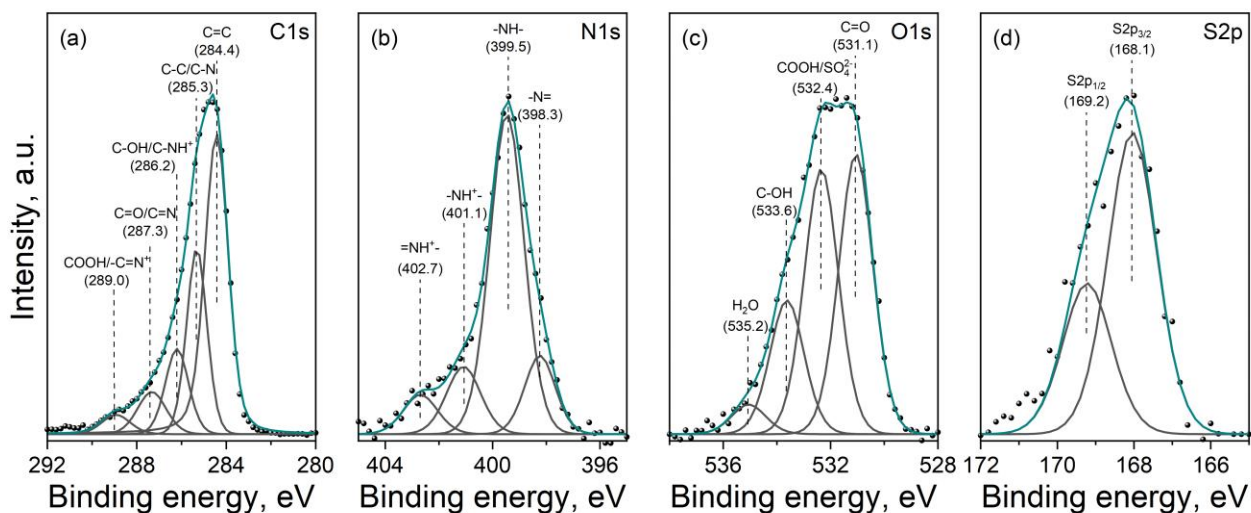
Figure 17. High-resolution C1s (a), N1s (b), O1s (c) and S2p (d) XPS spectra of SWCNT95/PANI40 sample.

The at.% concentrations of different species are represented in Table A3. The 21.5 at.% of carbon atoms is connected with OCFG and different nitrogen species, while the remaining 53.3 at.% and 25.3 at.% of carbon is related to the sp^2-hybrid carbon and sp^3-hybrid carbon (including C–C and C–N bonds). The concentrations of different OCFG were calculated from O1s high-resolution spectra. Thus, carbonyl OCFG is the main in PANI (39.5 at.%), while the concentration of carboxyl/SO_4^{2-} and hydroxyl OCFG is equal to the 37.4 and 18.9 at.%, respectively. The low amount of water (4.2 at.%) adsorbed on the polymer surface was also obtained. The total concentration of neutral charged nitrogen species (=N– in quinoid PANI units and –NH– in aromatic PANI units) is equal to 78.5 at.%. It means that the main part of the polymer is in a neutral state. As the concentration of =N– (14.1 at.%) is much lower than those of –NH– (64.4 at.%), the polymeric chain predominantly consists of aromatic PANI units. The total concentration of charged nitrogen species is equal to 21.5 at.% and corresponds to the formation of polaronic and bipolaronic structures.

3.3.3. Electrochemical measurements

3.3.3.1. Three-electrode cell configuration

The representative CV curves recorded in the three-electrode cell for the composites prepared using 40 and 70 PANI deposition cycles are characterized by the appearance of three pairs of redox peaks (Figure 18). These peaks correspond to redox reactions of PANI [105], *i.e.* the peak *a1* at 350 mV and counter peak *c1* at 180 mV corresponds to the leucoemeraldine-emeraldine transition. The peak *a2* at 550 mV and counter peak *c2* at about 400 mV may be associated with cross-linking reactions between polymer chains [119,198]. The peaks *a3* at 850 mV and *c3* at 700 mV can be related to the emeraldine-pernigraniline transition. A minor shift of the peaks is observed. It can be associated with the distinct architecture of the polymer chains and composite agglomerates. These peaks are better expressed on the CV curves of the thinnest SWCNT films with a small number of PANI deposition cycles (40 cycles). A thick polymer layer formed at a greater number of deposition cycles prevents the diffusion of the electrolyte that turns the redox peaks to be weakly manifested. Materials based on SWCNT90 have a better oriented 3D-structure, which contributes to better conductivity and faster redox processes. Besides, a lot of polymerization by-products might affect the shape of the CV curves that also explains less pronounced peaks and a slightly different shape of curves observed in the case of thicker polymer layers [44]. CV curves for all the samples are presented in Appendix (Figure A20).
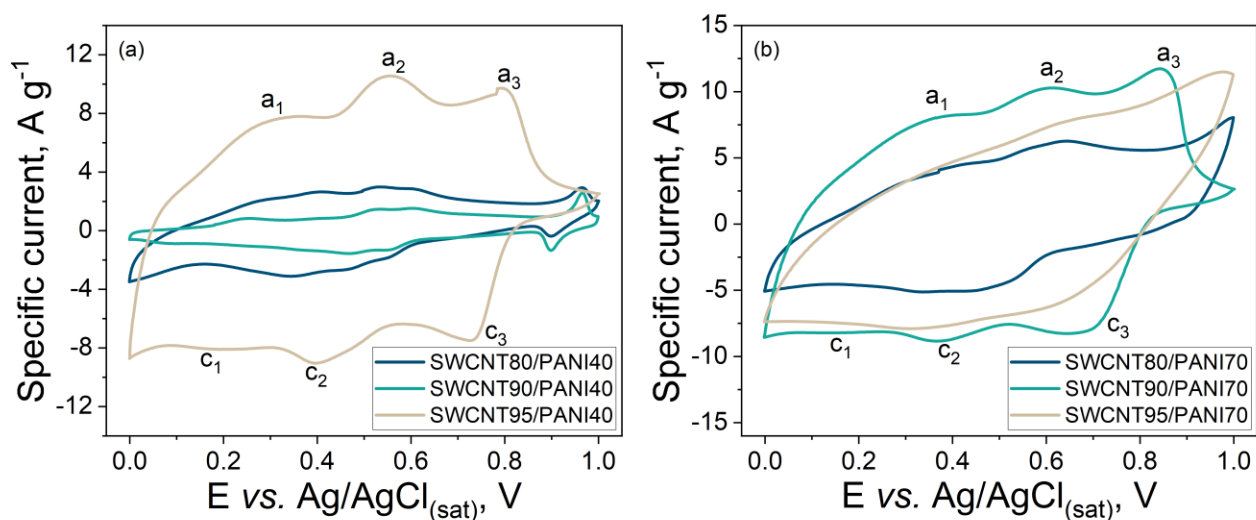
Figure 18. Characterization of capacitive properties of the SWCNT/PANI composites using the three-electrode cell configuration. CV curves of the samples based on SWCNT95, 90, and 80 and PANI deposited during 40 polymerization cycles, recorded at the scan rate of 20 mV s^{-1} (a). CV of the samples based on SWCNT95, 90, and 80 and PANI deposited during 70 polymerization cycles, recorded at the scan rate of 20 mV s^{-1} (b).

Galvanostatic charging-discharging results are presented in Figure 19a for the SWCNT95/PANI70 composite as an example. At a current density of 4.3 A g^{-1}, the discharge cycle can be described by two regions. A fast region corresponds to a range of potentials from the upper one to *ca.* 400 mV, while another region is characterized by a more moderate slope (400 mV-0 mV). The charge-discharge curves show good stability over the presented 10 cycles with the same temporal characteristics for discharge (or charge) cycles. Afterward, once being charged, we monitored potential values in an open-circuit mode for 10 min (Figure 19b). We observe that the thickness of the SWCNT film used for the PANI deposition influences the retained potential value, *i.e.* capacitance performance of the SC. The lowest self-discharge value is measured for the films with the highest transmittance (95 %). The low self-discharge rate for the composite materials based on the more transparent films is most likely associated with the higher resistance of the SWCNT95 framework [199]. The charge leakage is blocked due to the lower density of the films giving a rise to a greater impact of barriers at contacts between the semiconductor, and metallic SWCNTs in the film.
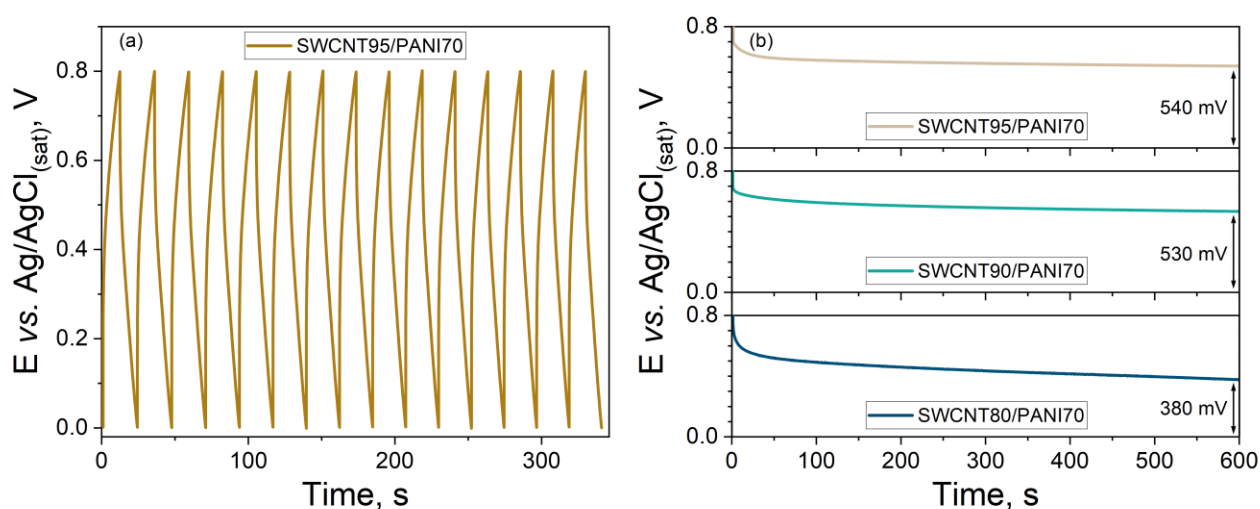
Figure 19. Charge-discharge curves of the SWCNT95/PANI70 composite (a). Open circuit potential transient recorded during 10 min after charging at 4.3 A g^{-1} for the SWCNT##/PANI70 composites (b).

A comparison of specific capacitance of the composite materials in the three-electrode cell at a scan rate of 20 mV s^{-1} is given in Figure 20. The highest capacitance is observed for the SWCNT95 samples (up to 541 F g^{-1}), and it is ~3 times higher than the capacitance of original SWCNTs (178 F g^{-1}) [115]. The high capacitance of the SWCNT95/PANI## samples (when compared with other composites, especially with the samples of 40–50 PANI deposition cycles) is explained by the porous

structure of these samples, which facilitates the diffusion of the electrolyte into the composite film [47]. The SWCNT95 films have a low density, allowing PANI to be deposited inside the SWCNT network so that the polymer bounds directly with the tubes. The lower capacitance of composites based on the SWCNT80 and SWCNT90 films is associated with the preferential growth of PANI on the surface of the film and higher PANI surface density. Moreover, in the later composites, the accumulation of the ions proceeds through amorphous PANI, which does not bound with SWCNTs directly, leading to a decrease in the efficiency of the materials [47]. The composite materials based on SWCNT80 and SWCNT90 reach the maximum capacitance when 70 deposition cycles yield an amorphous PANI layer with a characteristic 3D-structure. Notably, the retention of charge is much greater in the case of the SWCNT95/PANI## composites, again, caused by the higher electrical resistance of the SWCNT film.
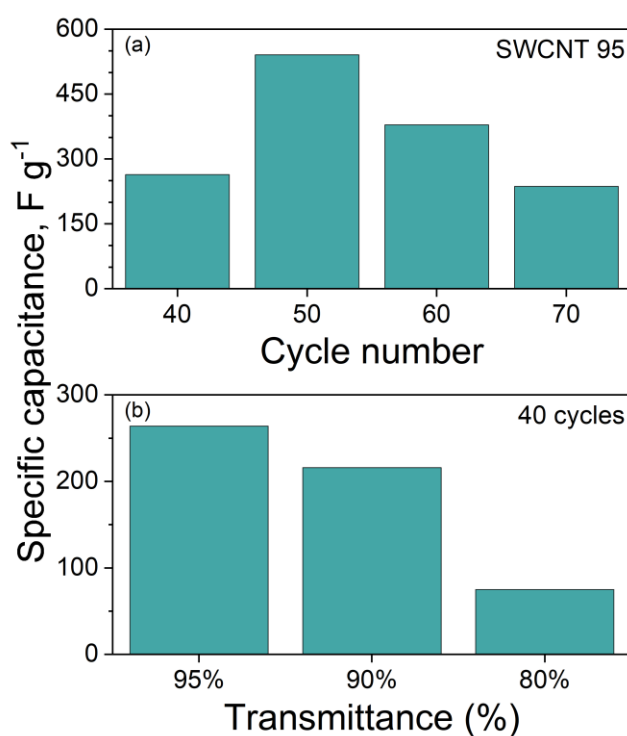
Figure 20. Specific capacitance measured in the three-electrode cell at the scan rate of 20 mV s^{-1} for the composites SWCNT95/PANI## (a), and composites SWCNT##/PANI40 (b).

Thus, using an excessive number of deposition cycles and/or using SWCNT films with the low transmittance (*i.e.*, greater thickness) as a template yields charge accumulation primarily attributed to amorphous PANI. Whereas films with high transmittance and a small PANI loading are characterized by a more ordered structure that causes the entire volume of the material to be included in the charge accumulation [168].

3.3.3.2. Two-electrode cell configuration

The three-electrode cell configuration is useful for analyzing redox reactions; however, real devices are operated as two-electrode cells. Cell capacitance in a two-electrode configuration is at least two times lower when compared with a three-electrode cell with the same mass of electrodes [200]. Moreover, a two-electrode cell, imitating coin cell architecture, offers a configuration where the PANI layer is in contact with the current collector mitigating the contribution of the SWCNT films in electron transport related to its sheet resistance. Figure 21 demonstrates CV curves recorded at 20 mV s^{-1} for the composite materials based on the SWCNT films of different transmittance after 50 deposition cycles of PANI when tested in a symmetrical two-electrode cell. We identify peaks at 350-550 mV during charging while the corresponding peaks are at 450-100 mV on the reverse scan. These peaks are related to the redox PANI reactions. The peaks are not well pronounced, rather wide, and overlap each other, which is associated with the lower sensitivity of the two-electrode cell [200]. Peaks on the CV curves of the materials based on the films with high transmittance (95 % and 90 %) appear earlier than peaks on the curves acquired for SWCNT80/PANI50 material. This indicates better diffusion availability of the SWCNT95 and SWCNT90 based composite materials for the electrolyte, which conforms to the conclusions made above. The calculated capacitance of the composites using the recorded CVs equals 130 and 175 F g^{-1} for SWCNT80/PANI50 and SWCNT90/PANI50, respectively, while it is 106 F g^{-1} for the SWCNT95/PANI50.
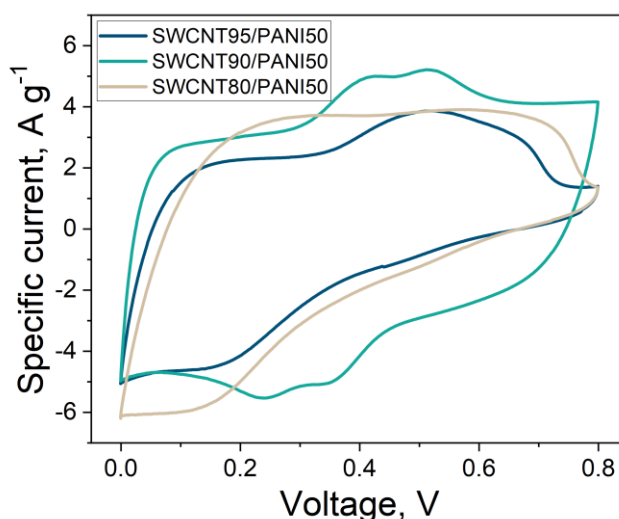
Figure 21. Capacitive properties of the SWCNT/PANI composites in the two-electrode cell configuration. CV of SWCNT95/PANI50, SWCNT90/PANI50, and SWCNT80/PANI50 measured in the two-electrode cell at 20 mV s^{-1}.

We studied next the capacitive properties of the composites in galvanostatic charge-discharge cycles at 4.3 A g^{-1}, followed by an assessment of self-discharge characteristics (Figure 22a). The films of SWCNT95/PANI50 tend to show rather asymmetric performance with long charging and fast discharging, which can be related to the high contribution of the redox process. The composites show low retention of capacitance with *ca.* 780 mV fade of voltage. The highest capacitance, in this case, is for the thicker PANI films, *i.e.*, specific capacitance measured in the two-electrode cell increases from 25 F g^{-1} to around 125 F g^{-1} for SWCNT95/PANI50 and SWCNT80/PANI50 respectively. Moreover, in the case of the two-electrode cell configuration, the thinner composite films lose their charge faster when compared with the thicker films. The self-discharge related losses in a two-electrode cell could be associated with a contact of composite with the current collectors through PANI. An increase in the PANI thickness leads to the rise of the polymer layer resistance and, thus, higher charge retention. The high charge retention can be also supported by the higher contribution of Faradaic processes. Therefore, the most significant influence on the self-discharge related losses in the two-electrode configuration has the thickness of the polymer coating, but not the SWCNT film.
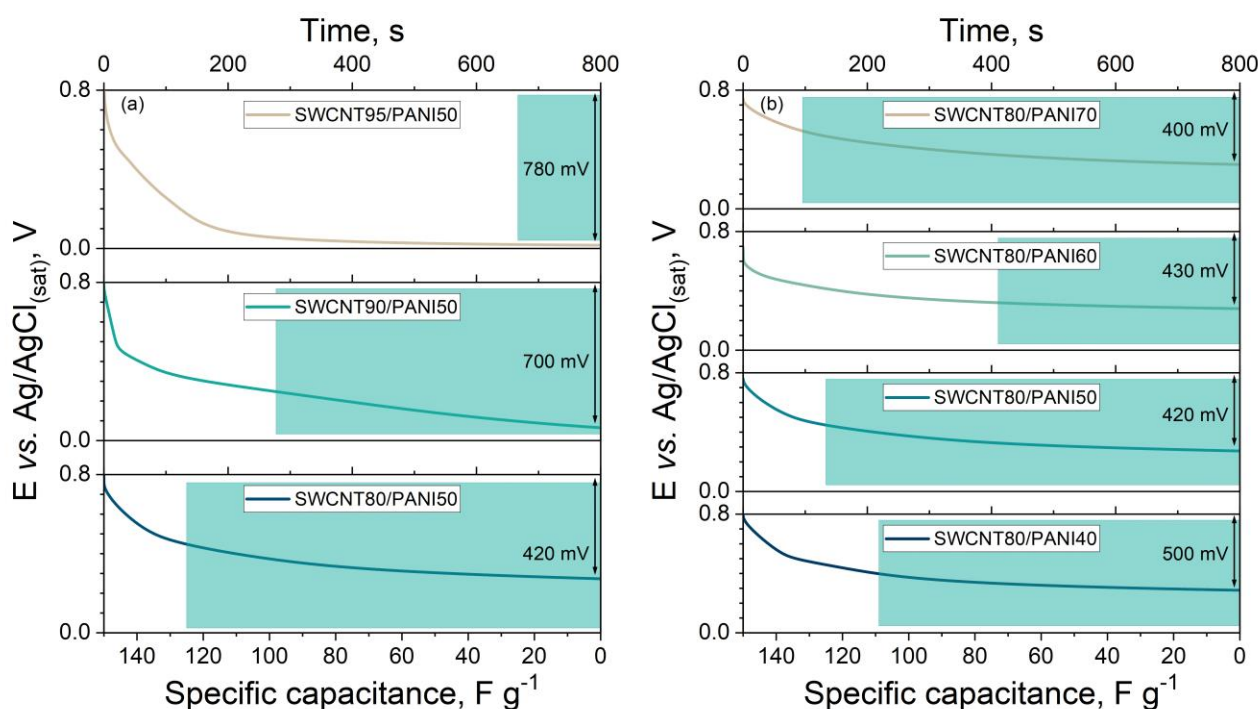
Figure 22. Capacitive properties of the SWCNT/PANI composites in the two-electrode cell configuration. Remaining potential after self-discharge for the SWCNT films with 50 PANI deposition cycles and capacitance calculated using galvanostatic discharge semicycle (a). Remaining potential after self-discharge for SWCNT80/PANI## and capacitance of SWCNT80/PANI## calculated using galvanostatic discharge semicycle (b).

We evaluated the dependency of capacitance for the composites based on the SWCNT80 films *versus* the number of deposition cycles of PANI, as well as their self-discharge characteristics after galvanostatic charge-discharge cycles (Figure 22b). The specific capacitance measured in the galvanostatic mode at a current density of 4.3 A g^{-1} in the two-electrode cell configuration tends to increase with an increase in the number of polymer deposition cycles to be up to 132 F g^{-1}. There is a minor hint on the improvement of charge retention during self-discharge with an increase in the number of PANI deposition cycles to be correlated with the measured capacitance.

The power and energy densities [90,200] of the assembled SC symmetric devices based on SWCNT/PANI composites obtained in this work were compared with the ones recently reported for SC devices based on PANI and carbon nanostructures (Figure A21). The resultant SC devices show a high energy density of 4.3–7.2 W h kg^{-1} at a power density of 1558–1794 W kg^{-1}, which is greater when compared to the symmetrical supercapacitors reported last years [201–206]. While energy density remains similar or slightly lower than the ones depicted in other works, power density reaches higher values. The calculated energy and power values are typical for hybrid SCs based on carbon nanostructures and PANI. Thicker SWCNT layers (80 % transmittance) demonstrate higher energy values when compared to the 90 % and 95 % because of the slower self-discharge processes demonstrated above.

3.3.3.3. Cycling and bending stability

The electrochemical stability of the SWCNT95/PANI50 material was also studied during long-term cycling in a two-electrode cell at a scan rate of 100 mV s^{-1} in a voltage range [0; 800] mV (Figure 23). The coulombic efficiency was calculated as the ratio of the cathodic charge Q_c to anodic charge Q_a, while the capacitance retention was calculated as maximum capacitance divided by the capacitance of a given cycle. Tendency to an increase in capacitance during the first thousand cycles is observed, which is possibly associated with the saturation of the polymer with the electrolyte. This behavior is typical for all CPs [207]. After 1000 cycles, a decrease in the capacitance is observed and it is stabilized at about 60 % of the original capacitance after 5000 cycles. This indicates relatively high stability for pseudocapacitive materials, but it is lower than that achieved in other works [208,209]. The behavior of coulombic efficiency is different from that of capacitance. The coulombic efficiency has a maximum value close to unity for only a few first cycles, after which it dramatically decreases, reaching a plateau (about 0.7) by the 500th cycle. Such a difference between the charge and discharge is associated with the side reactions of this type of film described above and can also be a reason for the low cyclic stability of the material.
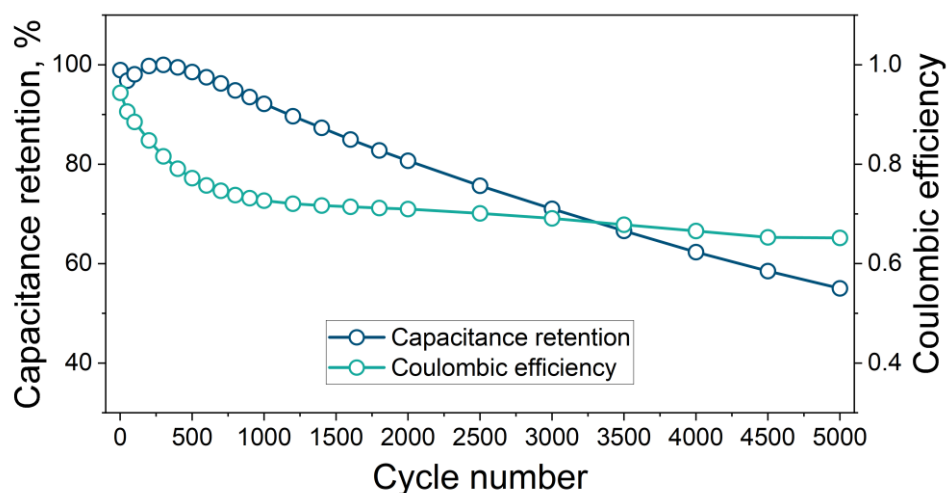
Figure 23. Electrochemical stability of the SWCNT95/PANI50 composite in two-electrode cell: capacitance retention and coulombic efficiency during long cycling.

To estimate specific capacitance at different charge-discharge rates and bent angle the device in a two-electrode free-standing configuration was employed using SWCNT90/PANI40 composite (Figure 24a). Using current density values during synthesis and mass-to-cycle number correlation of initial composite batch, obtained previously, the mass of resulting electrodes was estimated to be 73.6 µg. Five charge-discharge curves were recorded at four current densities, *i.e.*, 0.27, 0.68, 1.36, and 2.72 A g^{-1} (Figure A22).

The voltage drop decrease is observed with a decrease in charge-discharge rate. Also, the same behavior with 2 regions is taking place (the first region of rapid discharge down to 400 mV and then comparatively slower discharge from 400 mV down to 0 mV). At low currents density as 0.27 A g^{-1} cell does not reach 0.8 V even after 450 s, therefore, the capacitance was calculated for discharge semicircle employing the highest reached voltage in this case. Figure 24b represents the dependence of specific capacitance of the cell depending on the charge-discharge rate for all 5 cycles of each rate. It was calculated according to equation (2) with mass of active material to be equal to mass of two electrodes. We conclude that the higher the rate of supercapacitor cell charge, the lower the cell specific capacitance is. It could be the result of two related effects: increase of voltage drop with the growth of current and higher contribution of Faradaic processes at lower charge-discharge rates. After 25 cycles measured at different current densities, 90 % of the initial capacitance remains. A high drop in capacitance might be due to imperfectly flat cell architecture and side process accompanying the first cycles.
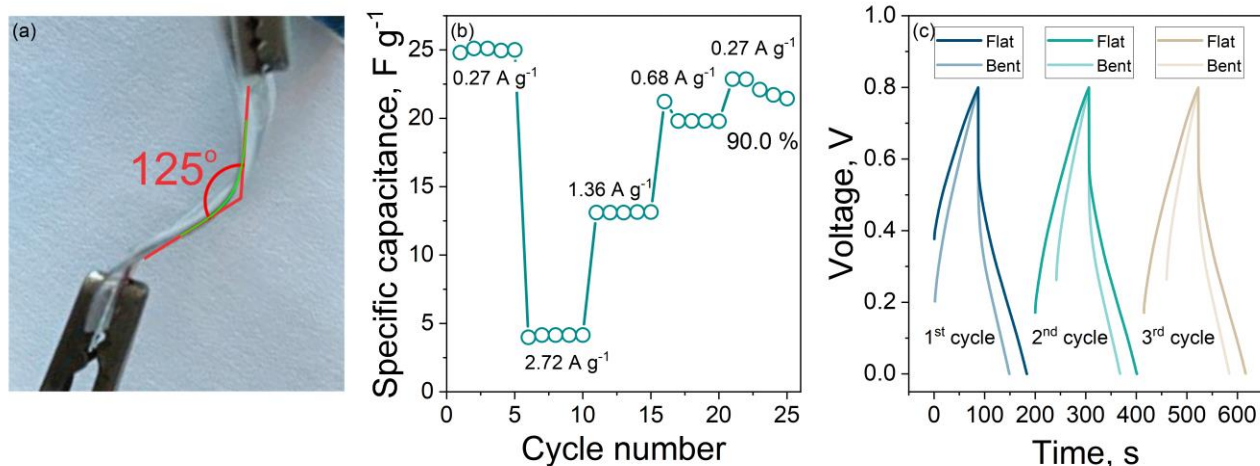
Figure 24. Characterization of SWCNT90/PANI40 film based two-electrode supercapacitor device. Photograph of bent supercapacitor: green curved line – electrodes location in the cell, red lined – directions of electrode terminations (a). Specific capacitance of the cell for different charge-discharge rates for every 5 consecutive cycles (b). Comparison of 3 consecutive charge-discharge cycles for flat (bright) and bent (pale) geometry of supercapacitor recorded at current density *ca.* 0.14 A g^{-1} (c).

A similar two-electrode cell was prepared for bending tests. Charge-discharge curves were measured for the flat and then for the device bent at an angle of 125° and also with some additional twisting along the device length. For both flat and bent geometry 3 charge-discharge cycles were recorded at *ca.* 0.14 A g^{-1}. Figure 24c shows the comparison of consecutive cycles for flat and bent devices. Starting from the second cycle, the device exhibits a representative pattern. We observe that device discharge capacitance per cycle decreases by 35 %. It is mainly represented by the smaller time consumed for each charge-discharge cycle. Besides, voltage drop increases for the bent sample that is manifested in some drop of the capacitance of the bent sample, although such effect might be corrected by optimizing cell configuration. On top of that, the coulombic efficiency of the bent sample is 94 % while for the flat it reaches 84 % only which can relate to worse electrolyte penetration and additional undesirable side reactions.

Capacitance retention of the prepared two-electrode free-standing device was assessed by cycling in a galvanostatic mode at 0.34 A g^{-1} over 1000 cycles charging it to 0.8 V. Before testing, the assembled device was conditioned for 24 h just at room temperature and afterward 10 training cycles were performed. The capacitance retention *versus* cycle number is given in Figure A24. We observe a moderate decrease in capacitance up to 200 cycles. The device capacitance reaches the stable values after about 500 cycles, maintained up to 1000 cycles.

CONCLUSIONS

1. Novel and simple method of highly efficient bilateral doping of SWCNT films for application as transparent conductive films was developed based on the thermal treatment of SWCNT films for the nanotube caps' opening at optimal temperatures of 300–400 ºC followed by doping with $HAuCl_4$ ethanol solution.

2. With application of the proposed method, a transparent conductive SWCNT films with a record equivalent sheet resistance value of 31 ± 4 Ω sq^{-1} were obtained. This value was achieved due to the significant Fermi-level downshift in the case of simultaneous doping from outside and inside of the thermally treated nanotubes.

3. Using CV features, Raman and XPS spectroscopy, sheet resistance measurements and filling efficiency evaluation we conclude that the formation of structural defects introduced under potentiodydamic treatment (CV) follows 3 stages with the following features. The 1st stage (UVPs < 1.1 V $vs.$ RHE): minor amount of wall defect formation & inefficient end-cap removal. The 2nd stage (UVP = 1.1 V $vs.$ RHE): trade-off between an efficient opening & moderate level of SWCNT wall defects. The 3rd stage (UVPs > 1.1 V $vs.$ RHE): extensive SWCNT wall destruction due to electrochemical treatment, the least efficient filling of SWCNTs.

4. We revealed that maximum filling efficiency ~1680 m cm^{-2} of gold nanowires length per unit area of ~87 % transmittance SWCNT film correspond to electrochemical treatment at UVP = 1.1 V $vs.$ RHE that is ~10 times higher than filling efficiency of reference sample.

5. We found that the weight of the SWCNT/PANI composite material synthesized under CV protocols increases linearly with decreasing the transmittance and increasing the number of deposition cycles (40-70 cycles). Layered PANI stricture is observed near SWCNT surface only, while PANI between nanotube bundles is represented as an amorphous polymer. It was found that PANI is deposited on the surface of thick films, with a comparably small amount of deposited polymer inside the network due to high nanotube density and film conductivity, whereas for thinnest films, a high degree of polymer penetration into the nanotube film is observed.

6. In three-electrode cell the specific gravimetric capacitance increases as the transmittance of SWCNT film ranges in a row of 80 %, 90 %, and 95 % (maximum is 541 F g^{-1}, 95 % transmittance SWCNT film and 50 PANI deposition cycles) due to a good 3D architecture and fast diffusion processes for more transparent films with a small number of PANI deposition cycles. Self-discharge is determined by the conductivity of the SWCNT films and decreases with the transmittance increase.

7. In two-electrode cell when electrical contact is realized through PANI layer, films based on SWCNT80 and SWCNT90 with the thickest PANI layer (70 cycles) show the highest specific capacitance reaching 130 and 175 F g^{-1}, respectively. Self-discharge in two-electrode configuration

is determined by the conductivity of the polymer and decreases with an increase of the deposited polymer layer thickness. Synthesized SWCNT composites were tested as free-standing flexible symmetric supercapacitors showing good stability during cycling and bending.

Materials obtained in the thesis research might find applications. In particular, efficiently doped SWCNT films can be applied as flexible transparent conducting films in flexible devises and wearable electronics. Composites based on the free-standing SWCNT covered with electrodeposited polyaniline showed decent supercapacitor material performance. It could find the application as the materials for flexible power sources, powering miniature wearable electronic devises. Developed protocols for filling SWCNT channels with Au nanowires might be used for production of filled SWCNTs with various other materials, including small organic molecules, inorganic substances, metals *etc*. Filled with metal SWCNTs may find application in electrocatalysis in HER and other reactions [14,210], gas-sensors, nanoelectronics and magnetic materials [1].

BIBLIOGRAPHY

1. Kharlamova M. V., Kramberger C. Applications of filled single-walled carbon nanotubes: Progress, challenges, and perspectives // Nanomaterials. 2021. Vol. 11, № 11. P. 2863.

2. Tian Y. et al. Growth of single-walled carbon nanotubes with controlled diameters and lengths by an aerosol method // Carbon N. Y. Elsevier Ltd, 2011. Vol. 49, № 14. P. 4636–4643.

3. Ki K.K. et al. Fermi level engineering of single-walled carbon nanotubes by AuCl 3 doping // J. Am. Chem. Soc. 2008. Vol. 130, № 38. P. 12757–12761.

4. Mattia D., Gogotsi Y. Review: Static and dynamic behavior of liquids inside carbon nanotubes // Microfluid. Nanofluidics. 2008. Vol. 5, № 3. P. 289–305.

5. Monthioux M., Flahaut E., Cleuziou J.P. Hybrid carbon nanotubes: Strategy, progress and perspectives // J. Mater. Res. 2006. Vol. 21, № 11. P. 2774–2793.

6. Poudel Y.R., Li W. Synthesis, properties, and applications of carbon nanotubes filled with foreign materials: a review // Mater. Today Phys. Elsevier Ltd, 2018. Vol. 7. P. 7–34.

7. Banhart F. et al. Metal atoms in carbon nanotubes and related nanoparticles // Int. J. Mod. Phys. B. 2001. Vol. 15, № 31. P. 4037–4069.

8. Kharlamova M. V. Advances in tailoring the electronic properties of single-walled carbon nanotubes // Prog. Mater. Sci. Elsevier Ltd, 2016. Vol. 77. P. 125–211.

9. Li Y.F. et al. Air-stable p-n junction diodes based on single-walled carbon nanotubes encapsulating Fe nanoparticles // Appl. Phys. Lett. 2007. Vol. 90, № 17.

10. Kato T. et al. P-N junction with donor and acceptor encapsulated single-walled carbon nanotubes // Appl. Phys. Lett. 2009. Vol. 95, № 8.

11. Borowiak-Palen E. et al. Iron filled single-wall carbon nanotubes - A novel ferromagnetic medium // Chem. Phys. Lett. 2006. Vol. 421, № 1–3. P. 129–133.

12. Kitaura R. et al. High yield synthesis and characterization of the structural and magnetic properties of crystalline ErCl3 nanowires in single-walled carbon nanotube templates // Nano Res. 2008. Vol. 1, № 2. P. 152–157.

13. Shiozawa H. et al. Nickel clusters embedded in carbon nanotubes as high performance magnets // Sci. Rep. Nature Publishing Group, 2015. Vol. 5. P. 1–9.

14. Aygün M. et al. Comparison of alkene hydrogenation in carbon nanoreactors of different diameters: Probing the effects of nanoscale confinement on ruthenium nanoparticle catalysis // J.

Mater. Chem. A. 2017. Vol. 5, № 40. P. 21467–21477.

15. Lota G. et al. High performance supercapacitor from chromium oxide-nanotubes based electrodes // Chem. Phys. Lett. 2007. Vol. 434, № 1–3. P. 73–77.

16. Jordan J.W. et al. Host–Guest Hybrid Redox Materials Self-Assembled from Polyoxometalates and Single-Walled Carbon Nanotubes // Adv. Mater. 2019. Vol. 31, № 41. P. 1904182.

17. Fedi F. et al. Reversible changes in the electronic structure of carbon nanotube-hybrids upon NO2exposure under ambient conditions // J. Mater. Chem. A. Royal Society of Chemistry, 2020. Vol. 8, № 19. P. 9753–9759.

18. Tsapenko A.P. et al. Aerosol-Assisted Fine-Tuning of Optoelectrical Properties of SWCNT Films // J. Phys. Chem. Lett. 2019. Vol. 10, № 14. P. 3961–3965.

19. Khabushev E.M. et al. Structure-dependent performance of single-walled carbon nanotube films in transparent and conductive applications // Carbon N. Y. Elsevier Ltd, 2020. Vol. 161. P. 712–717.

20. Khabushev E.M. et al. Machine Learning for Tailoring Optoelectronic Properties of Single-Walled Carbon Nanotube Films // J. Phys. Chem. Lett. 2019. P. 6962–6966.

21. Kaskela A. et al. Aerosol-Synthesized SWCNT Networks with Tunable Conductivity and Transparency by a Dry Transfer Technique // Nano Lett. 2010. Vol. 10, № 11. P. 4349–4355.

22. Hummer G., Rasaiah J.C., Noworyta J.P. Water conduction through the hydrophobic channel of a carbon nanotube // Nature. 2001. Vol. 414, № 6860. P. 188–190.

23. Joseph S., Aluru N.R. Why are carbon nanotubes fast transporters of water? // Nano Lett. 2008. Vol. 8, № 2. P. 452–458.

24. Supple S., Quirke N. Rapid Imbibition of Fluids in Carbon Nanotubes // Phys. Rev. Lett. 2003. Vol. 90, № 21. P. 214501.

25. Gogotsi Y., Naguib N., Libera J.A. In situ experiments in carbon nanotubes // Chem. Phys. Lett. 2002. Vol. 365, № 3–4. P. 354–360.

26. Noy A. et al. Nanofluidics in carbon nanotubes // Nano Today. 2007. Vol. 2, № 6. P. 22–29.

27. Bower C. et al. Intercalation and partial exfoliation of single-walled carbon nanotubes by nitric acid // Chem. Phys. Lett. 1998. Vol. 288, № 2–4. P. 481–486.

28. Monthioux M. Filling single-wall carbon nanotubes // Carbon N. Y. 2002. Vol. 40, № 10. P. 1809–1823.

29. Tsang S.C., Harris P.J.F., Green M.L.H. Thinning and opening of carbon nanotubes by oxidation using carbon dioxide // Nature. 1993. Vol. 362, № 6420. P. 520–522.

30. Niyogi S. et al. Chemistry of Single-Walled Carbon Nanotubes // Acc. Chem. Res. 2002. Vol. 35, № 12. P. 1105–1113.

31. Soldano C. Hybrid metal-based carbon nanotubes: Novel platform for multifunctional applications // Prog. Mater. Sci. Elsevier Ltd, 2015. Vol. 69. P. 183–212.

32. Ajayan P.M., Iijima S. Capillarity-induced filling of carbon nanotubes // Nature. 1993. Vol. 361, № 6410. P. 333–334.

33. Sloan J. et al. The opening and filling of single walled carbon nanotubes (SWTs) // Chem. Commun. 1998. Vol. 1, № 3. P. 347–348.

34. Smith B.W., Monthioux M., Luzzi D.E. Encapsulated C60 in carbon nanotubes // Nature. 1998. Vol. 396, № 6709. P. 323–324.

35. Kiang C.H. et al. Molecular nanowires of 1 nm diameter from capillary filling of single-walled carbon nanotubes // J. Phys. Chem. B. 1999. Vol. 103, № 35. P. 7449–7451.

36. Sloan J. et al. The size distribution, imaging and obstructing properties of C60 and higher fullerenes formed within arc-grown single walled carbon nanotubes // Chem. Phys. Lett. 2000. Vol. 316, № 3–4. P. 191–198.

37. Dujardin E. et al. Wetting of Single Shell Carbon Nanotubes // Adv. Mater. 1998. Vol. 10, № 17. P. 1472–1475.

38. Simotwo S.K., Delre C., Kalra V. Supercapacitor Electrodes Based on High-Purity Electrospun Polyaniline and Polyaniline-Carbon Nanotube Nanofibers // ACS Appl. Mater. Interfaces. 2016. Vol. 8, № 33. P. 21261–21269.

39. Jiao S. et al. A three-dimensional vertically aligned carbon nanotube/polyaniline composite as a supercapacitor electrode // RSC Adv. Royal Society of Chemistry, 2016. Vol. 6, № 112. P. 110592–110599.

40. Gao B., Zhou H., Yang J. Hierarchically porous carbons derived from polyaniline by "nanotube seeding" for high-performance ionic liquid-based supercapacitors // J. Mater. Chem. A. Royal Society of Chemistry, 2017. Vol. 5, № 2. P. 524–528.

41. Huang J., Kaner R.B. A General Chemical Route to Polyaniline Nanofibers // J. Am. Chem. Soc. 2004. Vol. 126, № 3. P. 851–855.

42. Fedorovskaya E.O. et al. Electrochemical Properties of the Ultrasonically Activated Thermally Expanded Graphite–Polyaniline Hybrid Material // Phys. Status Solidi Basic Res. 2018. Vol. 255, № 1. P. 1–5.

43. Hussain S. et al. Plasma synthesis of polyaniline enrobed carbon nanotubes for electrochemical applications // Electrochim. Acta. Elsevier Ltd, 2018. Vol. 268. P. 218–225.

44. Malik R. et al. Three-dimensional, free-standing polyaniline/carbon nanotube composite-based electrode for high-performance supercapacitors // Carbon N. Y. Elsevier Ltd, 2017. Vol. 116. P. 579–590.

45. Sivakkumar S.R. et al. Electrochemical performance of polyaniline nanofibres and polyaniline/multi-walled carbon nanotube composite as an electrode material for aqueous redox supercapacitors // J. Power Sources. 2007. Vol. 171, № 2. P. 1062–1068.

46. Bulusheva L.G. et al. Electronic state of polyaniline deposited on carbon nanotube or ordered mesoporous carbon templates // Phys. Status Solidi Basic Res. 2011. Vol. 248, № 11. P. 2484–2487.

47. Niu Z. et al. A "skeleton/skin" strategy for preparing ultrathin free-standing single-walled carbon nanotube/polyaniline films for high performance supercapacitor electrodes // Energy Environ. Sci. 2012. Vol. 5, № 9. P. 8726–8733.

48. Gupta V., Miura N. Polyaniline/single-wall carbon nanotube (PANI/SWCNT) composites for high performance supercapacitors // Electrochim. Acta. 2006. Vol. 52, № 4. P. 1721–1726.

49. Cherusseri J., Kar K.K. Ultra-flexible fibrous supercapacitors with carbon nanotube/polypyrrole brush-like electrodes // J. Mater. Chem. A. Royal Society of Chemistry, 2016. Vol. 4, № 25. P. 9910–9922.

50. Kalagi S.S., Patil P.S. Studies on electrochemical activity of CNT/PANI composite thin film coating on ITO coated glass surfaces: Effect of concentration on fractal dimension // Electrochim. Acta. Elsevier Ltd, 2017. Vol. 231. P. 521–528.

51. Iurchenkova A.A. et al. MWCNT buckypaper/polypyrrole nanocomposites for supercapasitor application // Electrochim. Acta. Elsevier Ltd, 2020. Vol. 335. P. 135700.

52. Ajayan P.M. et al. Opening carbon nanotubes with oxygen and implications for filling // Nature. 1993. Vol. 362, № 6420. P. 522–525.

53. Hirahara K. et al. One-dimensional metallofullerene crystal generated inside single-walled carbon nanotubes // Phys. Rev. Lett. 2000. Vol. 85, № 25. P. 5384–5387.

54. Tsang S.C. et al. A simple chemical method of opening and filling carbon nanotubes // Nature. 1994. Vol. 372, № 6502. P. 159–162.

55. Monthioux M. et al. Sensitivity of single-wall carbon nanotubes to chemical processing: An electron microscopy investigation // Carbon N. Y. 2001. Vol. 39, № 8. P. 1251–1272.

56. Holloway A.F. et al. Electrochemical Opening of Single-Walled Carbon Nanotubes Filled with Metal Halides and with Closed Ends // J. Phys. Chem. C. 2008. Vol. 112, № 28. P. 10389–10397.

57. Tominaga M., Yatsugi Y., Watanabe N. Oxidative corrosion potential vs. pH diagram for single-walled carbon nanotubes // RSC Adv. 2014. Vol. 4, № 52. P. 27224.

58. Afre R.A. et al. Transparent conducting oxide films for various applications: A review // Rev. Adv. Mater. Sci. 2018. Vol. 53, № 1. P. 79–89.

59. Li D. et al. Printable Transparent Conductive Films for Flexible Electronics // Adv. Mater. 2018. Vol. 30, № 10. P. 1–24.

60. Park S., Vosguerichian M., Bao Z. A review of fabrication and applications of carbon nanotube film-based flexible electronics // Nanoscale. 2013. Vol. 5, № 5. P. 1727–1752.

61. Zhang R., Engholm M. Recent progress on the fabrication and properties of silver nanowire-based transparent electrodes // Nanomaterials. 2018. Vol. 8, № 8. P. 1–17.

62. Wen Y., Xu J. Scientific Importance of Water-Processable PEDOT–PSS and Preparation, Challenge and New Application in Sensors of Its Film Electrode: A Review // J. Polym. Sci. Part A Polym. Chem. 2017. Vol. 55, № 7. P. 1121–1150.

63. Bin Mohd Yusoff A.R. et al. Au-doped single layer graphene nanoribbons for a record-high efficiency ITO-free tandem polymer solar cell // Energy Environ. Sci. Royal Society of Chemistry, 2015. Vol. 8, № 5. P. 1523–1537.

64. Eda G., Fanchini G., Chhowalla M. Large-area ultrathin films of reduced graphene oxide as a transparent and flexible electronic material // Nat. Nanotechnol. 2008. Vol. 3, № 5. P. 270–274.

65. Trottier C.M. et al. Properties and characterization of carbon-nanotube-based transparent conductive coating // J. Soc. Inf. Disp. 2005. Vol. 13, № 9. P. 759.

66. M. Rajanna P. et al. Adhesion of Single-Walled Carbon Nanotube Thin Films with Different Materials // J. Phys. Chem. Lett. 2020. Vol. 11, № 2. P. 504–509.

67. Liu H. et al. Large-scale single-chirality separation of single-wall carbon nanotubes by simple gel chromatography // Nat. Commun. Nature Publishing Group, 2011. Vol. 2, № 1.

68. Dan B., Irvin G.C., Pasquali M. Continuous and scalable fabrication of transparent conducting carbon nanotube films // ACS Nano. 2009. Vol. 3, № 4. P. 835–843.

69. Park S. et al. Large-Area Assembly of Densely Aligned Single-Walled Carbon Nanotubes Using Solution Shearing and Their Application to Field-Effect Transistors // Adv. Mater. 2015. Vol. 27, № 16. P. 2656–2662.

70. Gilshteyn E.P. et al. Mechanically Tunable Single-Walled Carbon Nanotube Films as a Universal Material for Transparent and Stretchable Electronics // ACS Appl. Mater. Interfaces. 2019. Vol. 11, № 30. P. 27327–27334.

71. Zhu C. et al. Stretchable temperature-sensing circuits with strain suppression based on carbon nanotube transistors // Nat. Electron. Springer US, 2018. Vol. 1, № 3. P. 183–190.

72. Tsapenko A.P. et al. Aerosol-Assisted Fine-Tuning of Optoelectrical Properties of SWCNT Films // J. Phys. Chem. Lett. 2019. Vol. 10, № 14. P. 3961–3965.

73. Kim K.K. et al. Doping strategy of carbon nanotubes with redox chemistry // New J. Chem. 2010. Vol. 34, № 10. P. 2183–2188.

74. Meng C. et al. Highly flexible and all-solid-state paperlike polymer supercapacitors // Nano Lett. 2010. Vol. 10, № 10. P. 4025–4031.

75. Wang X. et al. Flexible energy-storage devices: Design consideration and recent progress // Adv. Mater. 2014. Vol. 26, № 28. P. 4763–4782.

76. Yousaf M. et al. Novel Pliable Electrodes for Flexible Electrochemical Energy Storage Devices: Recent Progress and Challenges // Adv. Energy Mater. 2016. Vol. 6, № 17. P. 1–23.

77. Simon P., Gogotsi Y., Dunn B. Where Do Batteries End and Supercapacitors Begin? // Science (80-.). 2014. Vol. 343, № 6176. P. 1210–1211.

78. Chen T., Dai L. Flexible supercapacitors based on carbon nanomaterials // J. Mater. Chem. A. 2014. Vol. 2, № 28. P. 10756–10775.

79. Kim S.H. et al. A shape-deformable and thermally stable solid-state electrolyte based on a plastic crystal composite polymer electrolyte for flexible/safer lithium-ion batteries // J. Mater. Chem. A. 2014. Vol. 2, № 28. P. 10854–10861.

80. Jost K. et al. Carbon coated textiles for flexible energy storage // Energy Environ. Sci. 2011. Vol. 4, № 12. P. 5060–5067.

81. Zhou G., Li F., Cheng H.M. Progress in flexible lithium batteries and future prospects // Energy

Environ. Sci. 2014. Vol. 7, № 4. P. 1307–1338.

82. Lee Y.H. et al. Wearable textile battery rechargeable by solar energy // Nano Lett. 2013. Vol. 13, № 11. P. 5753–5761.

83. Huang D. et al. Three-dimensional conductive networks based on stacked SiO2@graphene frameworks for enhanced gas sensing // Nanoscale. Royal Society of Chemistry, 2017. Vol. 9, № 1. P. 109–118.

84. Becker H.I. Low Voltage Electrolytic Capacitor Patent. 1954.

85. Trasatti S., Buzzanca G. Ruthenium dioxide: A new interesting electrode material. Solid state structure and electrochemical behaviour // J. Electroanal. Chem. 1971. Vol. 29, № 2. P. A1–A5.

86. Craig D. Canadian Pat. No. 1196683. 1985.

87. Hadz̄i-Jordanov S. et al. Reversibility and Growth Behavior of Surface Oxide Films at Ruthenium Electrodes // J. Electrochem. Soc. 1978. Vol. 125, № 9. P. 1471–1480.

88. Conway B.E. Transition from "supercapacitor" to "battery" behavior in electrochemical energy storage // Proc. Int. Power Sources Symp. 1991. P. 319–327.

89. Jo A. et al. All-Printed Paper-Based Micro-supercapacitors Using Water-Based Additive-Free Oxidized Single-Walled Carbon Nanotube Pastes // ACS Appl. Energy Mater. 2021. Vol. 4, № 12. P. 13666–13675.

90. B.E. Conway. Electrochemical Supercapacitors: Scientific Fundamentals and Technological Applications. New York: Kluwer Academic/Plenum Publishing, 1999.

91. Bashir S. et al. Nanostructured Materials for Advanced Energy Conversion and Storage Devices: Safety Implications at End-of-Life Disposal // Nanostructured Materials for Next-Generation Energy Storage and Conversion. Berlin, Heidelberg: Springer Berlin Heidelberg, 2018. P. 517–542.

92. Béguin F. et al. Carbons and electrolytes for advanced supercapacitors // Adv. Mater. 2014. Vol. 26, № 14. P. 2219–2251.

93. Simon P., Gogotsi Y. Materials for electrochemical capacitors // Nat. Mater. 2008. Vol. 7, № 11. P. 845–854.

94. Kötz R., Carlen M. Principles and applications of electrochemical capacitors // Electrochim. Acta. 2000. Vol. 45, № 15–16. P. 2483–2498.

95. Simon P., Gogotsi Y. Perspectives for electrochemical capacitors and related devices // Nat.

Mater. Springer US, 2020. Vol. 19, № 11. P. 1151–1163.

96. Ji H. et al. Capacitance of carbon-based electrical double-layer capacitors // Nat. Commun. Nature Publishing Group, 2014. Vol. 5, № 1. P. 3317.

97. Fedorov F.S. et al. Capacitance performance of cobalt hydroxide-based capacitors with utilization of near-neutral electrolytes // Electrochim. Acta. Elsevier Ltd, 2013. Vol. 90. P. 166–170.

98. Simon P., Gogotsi Y. Capacitive Energy Storage in Nanostructured Carbon–Electrolyte Systems // Acc. Chem. Res. 2013. Vol. 46, № 5. P. 1094–1103.

99. Chmiola J. et al. Anomalous Increase in Carbon Capacitance at Pore Sizes Less Than 1 Nanometer // Science (80-.). 2006. Vol. 313, № 5794. P. 1760–1763.

100. Pan H., Li J., Feng Y.P. Carbon Nanotubes for Supercapacitor // Nanoscale Res. Lett. 2010. Vol. 5, № 3. P. 654–668.

101. Augustyn V. et al. High-rate electrochemical energy storage through Li+ intercalation pseudocapacitance // Nat. Mater. 2013. Vol. 12, № 6. P. 518–522.

102. Hu L. et al. Symmetrical MnO 2 –Carbon Nanotube–Textile Nanostructures for Wearable Pseudocapacitors with High Mass Loading // ACS Nano. 2011. Vol. 5, № 11. P. 8904–8913.

103. Zhao Y. et al. Ni 3+ doped monolayer layered double hydroxide nanosheets as efficient electrodes for supercapacitors // Nanoscale. Royal Society of Chemistry, 2015. Vol. 7, № 16. P. 7168–7173.

104. Kim J. et al. Synthesis and Electrochemical Properties of Spin-Capable Carbon Nanotube Sheet/MnO x Composites for High-Performance Energy Storage Devices // Nano Lett. 2011. Vol. 11, № 7. P. 2611–2617.

105. Yu H. et al. Facile fabrication and energy storage analysis of graphene/PANI paper electrodes for supercapacitor application // Electrochim. Acta. Elsevier Ltd, 2017. Vol. 253. P. 239–247.

106. Zhang Q. et al. Electropolymerization of graphene oxide/polyaniline composite for high-performance supercapacitor // Electrochim. Acta. 2013. Vol. 90. P. 95–100.

107. Nyholm L. et al. Toward Flexible Polymer and Paper-Based Energy Storage Devices // Adv. Mater. 2011. Vol. 23, № 33. P. n/a-n/a.

108. Evlashin S.A. et al. Role of Nitrogen and Oxygen in Capacitance Formation of Carbon Nanowalls // J. Phys. Chem. Lett. 2020. Vol. 11, № 12. P. 4859–4865.

109. Gilshteyn E.P. et al. All-nanotube stretchable supercapacitor with low equivalent series resistance // Sci. Rep. Springer US, 2017. Vol. 7, № 1. P. 17449.

110. Wen L., Li F., Cheng H. Carbon Nanotubes and Graphene for Flexible Electrochemical Energy Storage: from Materials to Devices // Adv. Mater. 2016. Vol. 28, № 22. P. 4306–4337.

111. Yu S., Patil B., Ahn H. Flexible, fiber-shaped supercapacitors with roll-type assembly // J. Ind. Eng. Chem. The Korean Society of Industrial and Engineering Chemistry, 2019. Vol. 71. P. 220–227.

112. Nasibulin A.G. et al. Multifunctional Free-Standing Single-Walled Carbon Nanotube Films // ACS Nano. 2011. Vol. 5, № 4. P. 3214–3221.

113. Fedorov F.S. et al. High Performance Hydrogen Evolution Reaction Catalyst Based on Single-Walled Carbon Nanotubes Decorated by RuO x Nanoparticles // ChemElectroChem. 2020. Vol. 7, № 12. P. 2651–2659.

114. Yu D. et al. Emergence of fiber supercapacitors // Chem. Soc. Rev. Royal Society of Chemistry, 2015. Vol. 44, № 3. P. 647–662.

115. Kanninen P. et al. Transparent and flexible high-performance supercapacitors based on single-walled carbon nanotube films // Nanotechnology. IOP Publishing, 2016. Vol. 27, № 23. P. 235403.

116. Wang K. et al. Flexible solid-state supercapacitors based on a conducting polymer hydrogel with enhanced electrochemical performance // J. Mater. Chem. A. Royal Society of Chemistry, 2014. Vol. 2, № 46. P. 19726–19732.

117. Wang K. et al. Conducting Polymer Nanowire Arrays for High Performance Supercapacitors // Small. 2014. Vol. 10, № 1. P. 14–31.

118. Le T.-H., Kim Y., Yoon H. Electrical and Electrochemical Properties of Conducting Polymers // Polymers (Basel). 2017. Vol. 9, № 12. P. 150.

119. Eftekhari A., Li L., Yang Y. Polyaniline supercapacitors // J. Power Sources. Elsevier B.V, 2017. Vol. 347. P. 86–107.

120. Frackowiak E. et al. Supercapacitors based on conducting polymers/nanotubes composites // J. Power Sources. 2006. Vol. 153, № 2. P. 413–418.

121. Rauhala T. et al. On the stability of polyaniline/carbon nanotube composites as binder-free positive electrodes for electrochemical energy storage // Electrochim. Acta. Elsevier Ltd, 2020. Vol. 336. P. 135735.

122. Tian Y. et al. Tailoring the diameter of single-walled carbon nanotubes for optical applications // Nano Res. 2011. Vol. 4, № 8. P. 807–815.

123. Ermolaev G.A. et al. Express determination of thickness and dielectric function of single-walled carbon nanotube films // Appl. Phys. Lett. AIP Publishing LLC, 2020. Vol. 116, № 23. P. 231103.

124. Gorkina A.L. et al. Transparent and conductive hybrid graphene/carbon nanotube films // Carbon N. Y. Elsevier Ltd, 2016. Vol. 100. P. 501–507.

125. Satco D. et al. Intersubband plasmon observation in electrochemically gated carbon nanotube films // ACS Appl. Electron. Mater. 2020. Vol. 2, № 1. P. 195–203.

126. Drozdov G. et al. Densification of single-walled carbon nanotube films: Mesoscopic distinct element method simulations and experimental validation // J. Appl. Phys. 2020. Vol. 128, № 18. P. 184701.

127. Romanov S.A. et al. Rapid, efficient, and non-destructive purification of single-walled carbon nanotube films from metallic impurities by Joule heating // Carbon N. Y. 2020. Vol. 168. P. 193–200.

128. Dresselhaus M.S., Dresselhaus G., Jorio A. Unusual properties and structure of carbon nanotubes // Annu. Rev. Mater. Res. 2004. Vol. 34, № 1. P. 247–278.

129. Anoshkin I. V. et al. Hybrid carbon source for single-walled carbon nanotube synthesis by aerosol CVD method // Carbon N. Y. Elsevier Ltd, 2014. Vol. 78. P. 130–136.

130. Romanov S.A. et al. Highly efficient thermophones based on freestanding single-walled carbon nanotube films // Nanoscale Horizons. Royal Society of Chemistry, 2019. Vol. 4, № 5. P. 1158–1163.

131. Perdew J.P., Burke K., Ernzerhof M. Generalized Gradient Approximation Made Simple // Phys. Rev. Lett. 1996. Vol. 77, № 18. P. 3865–3868.

132. Blöchl P.E. Projector augmented-wave method // Phys. Rev. B. 1994. Vol. 50, № 24. P. 17953–17979.

133. Kresse G., Hafner J. Ab initio molecular dynamics for liquid metals // Phys. Rev. B. 1993. Vol. 47, № 1. P. 558–561.

134. Kresse G., Furthmüller J. Efficiency of ab-initio total energy calculations for metals and semiconductors using a plane-wave basis set // Comput. Mater. Sci. 1996. Vol. 6, № 1. P. 15–50.

135. Grimme S. et al. A consistent and accurate ab initio parametrization of density functional dispersion correction (DFT-D) for the 94 elements H-Pu // J. Chem. Phys. 2010. Vol. 132, № 15.

136. Monkhorst H.J., Pack J.D. Special points for Brillouin-zone integrations // Phys. Rev. B. 1976.

Vol. 13, № 12. P. 5188–5192.

137. Shandakov S.D., Lomakin M. V., Nasibulin A.G. The effect of the environment on the electronic properties of single-walled carbon nanotubes // Tech. Phys. Lett. 2016. Vol. 42, № 11. P. 1071–1075.

138. Collins P.G. et al. Extreme Oxygen Sensitivity of Electronic Properties of Carbon Nanotubes // Science (80-.). 2000. Vol. 287, № 5459. P. 1801–1804.

139. Yu X. et al. Cap Formation Engineering: From Opened C 60 to Single-Walled Carbon Nanotubes // Nano Lett. 2010. Vol. 10, № 9. P. 3343–3349.

140. Liu B. et al. Chirality-Dependent Reactivity of Individual Single-Walled Carbon Nanotubes // Small. 2013. Vol. 9, № 8. P. 1379–1386.

141. Tsapenko A.P. et al. Highly conductive and transparent films of HAuCl4-doped single-walled carbon nanotubes for flexible applications // Carbon N. Y. 2018. Vol. 130. P. 448–457.

142. Kim S.M. et al. Role of anions in the AuCl3-doping of carbon nanotubes // ACS Nano. 2011. Vol. 5, № 2. P. 1236–1242.

143. Finkelstein N.P., Hancock R.D. A new approach to the chemistry of gold // Gold Bull. 1974. Vol. 7, № 3. P. 72–77.

144. Satco D. et al. Intersubband plasmon excitations in doped carbon nanotubes // Phys. Rev. B. American Physical Society, 2019. Vol. 99, № 7. P. 1–13.

145. Jorio A. et al. Characterizing carbon nanotube samples with resonance Raman scattering // New J. Phys. 2003. Vol. 5.

146. Kim K.K. et al. Dependence of Raman spectra G′ band intensity on metallicity of single-wall carbon nanotubes // Phys. Rev. B - Condens. Matter Mater. Phys. 2007. Vol. 76, № 20. P. 1–8.

147. Kobayashi K. et al. In situ observation of gold chloride decomposition in a confined nanospace by transmission electron microscopy // Mater. Trans. 2014. Vol. 55, № 3. P. 461–465.

148. Murat A. et al. Origin of the p-Type Character of AuCl 3 Functionalized Carbon Nanotubes // J. Phys. Chem. C. 2014. Vol. 118, № 6. P. 3319–3323.

149. Clark E.S., Templeton D.H., MacGillavry C.H. The crystal structure of gold(III) chloride // Acta Crystallogr. 1958. Vol. 11, № 4. P. 284–288.

150. Janssen E.M.W., Folmer J.C.W., Wiegers G.A. The preparation and crystal structure of gold monochloride, AuCl // J. Less-Common Met. 1974. Vol. 38, № 1. P. 71–76.

151. Heras A. et al. Electrochemical purification of carbon nanotube electrodes // Electrochem. commun. Elsevier B.V., 2009. Vol. 11, № 7. P. 1535–1538.

152. Raymundo-Piñero E., Leroux F., Béguin F. A High-Performance Carbon for Supercapacitors Obtained by Carbonization of a Seaweed Biopolymer // Adv. Mater. 2006. Vol. 18, № 14. P. 1877–1882.

153. Kim Y.-T. et al. Drastic change of electric double layer capacitance by surface functionalization of carbon nanotubes // Appl. Phys. Lett. 2005. Vol. 87, № 23. P. 1–3.

154. Ye J.-S. et al. Electrochemical oxidation of multi-walled carbon nanotubes and its application to electrochemical double layer capacitors // Electrochem. commun. 2005. Vol. 7, № 3. P. 249–255.

155. Pan H. et al. Supercapacitor Electrodes from Tubes-in-Tube Carbon Nanostructures // Chem. Mater. 2007. Vol. 19, № 25. P. 6120–6125.

156. Kobets A.A. et al. Redox Processes in Reduced Graphite Oxide Decorated by Carboxyl Functional Groups // Phys. Status Solidi Basic Res. 2019. Vol. 256, № 9. P. 1–7.

157. Allen J. Bard L.R.F. Electrochemical Methods: Fundamentals and Applications. 2nd ed. New York: Wiley, 2001.

158. Dresselhaus M.S. et al. Raman spectroscopy of carbon nanotubes // Phys. Rep. 2005. Vol. 409, № 2. P. 47–99.

159. Tominaga M., Yatsugi Y., Togami M. Effect of oxygen adsorption on the electrochemical oxidative corrosion of single-walled carbon nanotubes // RSC Adv. Royal Society of Chemistry, 2014. Vol. 4, № 96. P. 53833–53836.

160. Sakamoto S., Tominaga M. Determination of the Diameter-Dependent Onset Potential for the Oxygenation of SWCNTs // Chem. – An Asian J. 2013. Vol. 8, № 11. P. 2680–2684.

161. Graupner R. et al. Doping of single-walled carbon nanotube bundles by Brønsted acids // Phys. Chem. Chem. Phys. 2003. Vol. 5, № 24. P. 5472–5476.

162. Díaz J. et al. Separation of the sp3 and sp2 components in the C1s photoemission spectra of amorphous carbon films // Phys. Rev. B - Condens. Matter Mater. Phys. 1996. Vol. 54, № 11. P. 8064–8069.

163. Biesinger M.C. Accessing the robustness of adventitious carbon for charge referencing (correction) purposes in XPS analysis: Insights from a multi-user facility data review // Appl. Surf. Sci. 2022. Vol. 597, № May.

164. Biniak S. et al. The characterization of activated carbons with oxygen and nitrogen surface groups // Carbon N. Y. 1997. Vol. 35, № 12. P. 1799–1810.

165. Conroy K.G., Breslin C.B. The electrochemical deposition of polyaniline at pure aluminium: Electrochemical activity and corrosion protection properties // Electrochim. Acta. 2003. Vol. 48, № 6. P. 721–732.

166. Yoo J.E. et al. Improving the electrical conductivity of polymer acid-doped polyaniline by controlling the template molecular weight // J. Mater. Chem. 2007. Vol. 17, № 13. P. 1268–1275.

167. Attout A., Yunus S., Bertrand P. Electroless deposition of polyaniline: Synthesis and characterization // Surf. Interface Anal. 2008. Vol. 40, № 3–4. P. 657–660.

168. Zhang H. et al. Electrodeposition of polyaniline nanostructures: A lamellar structure // Synth. Met. 2009. Vol. 159, № 3–4. P. 277–281.

169. Kim J.-W. et al. Polyaniline/Carbon Nanotube Sheet Nanocomposites: Fabrication and Characterization // ACS Appl. Mater. Interfaces. 2013. Vol. 5, № 17. P. 8597–8606.

170. Minati L. et al. Investigation on the electronic and optical properties of short oxidized multiwalled carbon nanotubes // J. Phys. Chem. C. 2010. Vol. 114, № 25. P. 11068–11073.

171. Wu T.M., Lin Y.W., Liao C.S. Preparation and characterization of polyaniline/multi-walled carbon nanotube composites // Carbon N. Y. 2005. Vol. 43, № 4. P. 734–740.

172. Stubrov Y. et al. Manifestation of Structure of Electron Bands in Double-Resonant Raman Spectra of Single-Walled Carbon Nanotubes // Nanoscale Res. Lett. Nanoscale Research Letters, 2016. Vol. 11, № 1. P. 1–5.

173. Komarova N.S. et al. Active forms of oxygen as agents for electrochemical functionalization of SWCNTs // Carbon N. Y. 2013. Vol. 53. P. 188–196.

174. Rodriguez R.D., Ma B., Sheremet E. Raman Spectroscopy Investigation of Laser-Irradiated Single-Walled Carbon Nanotube Films // Phys. Status Solidi Basic Res. 2019. Vol. 256, № 2. P. 1–5.

175. Ansari N. et al. Trace level toxic ammonia gas sensing of single-walled carbon nanotubes wrapped polyaniline nanofibers // J. Appl. Phys. AIP Publishing LLC, 2020. Vol. 127, № 4.

176. Lone M.Y. et al. Growth of single wall carbon nanotubes using PECVD technique: An efficient chemiresistor gas sensor // Phys. E Low-Dimensional Syst. Nanostructures. Elsevier, 2017. Vol. 87, № November 2016. P. 261–265.

177. Yan X. Bin et al. Fabrication of carbon nanotube-polyaniline composites via electrostatic adsorption in aqueous colloids // J. Phys. Chem. C. 2007. Vol. 111, № 11. P. 4125–4131.

178. Peikertová P. et al. Raman study of PANI thin film during long time period in dependence on storage conditions // Chem. Pap. 2017. Vol. 71, № 2. P. 379–385.

179. Boyer M.I. et al. Vibrational analysis of polyaniline: A model compound approach // J. Phys. Chem. B. 1998. Vol. 102, № 38. P. 7382–7392.

180. Trchová M. et al. Raman spectroscopy of polyaniline and oligoaniline thin films // Electrochim. Acta. Elsevier Ltd, 2014. Vol. 122. P. 28–38.

181. Cochet M. et al. Theoretical and experimental vibrational study of emeraldine in salt form. Part II // J. Raman Spectrosc. 2000. Vol. 31, № 12. P. 1041–1049.

182. Tagowska M., Pałys B., Jackowska K. Polyaniline nanotubules - Anion effect on conformation and oxidation state of polyaniline studied by Raman spectroscopy // Synth. Met. 2004. Vol. 142, № 1–3. P. 223–229.

183. Lefrant S. et al. Functionalization of single-walled carbon nanotubes with conducting polymers evidenced by Raman and FTIR spectroscopy // Diam. Relat. Mater. 2005. Vol. 14, № 3–7. P. 867–872.

184. Pereira Da Silva J.E., Temperini M.L.A., Córdoba De Torresi S.I. Secondary doping of polyaniline studied by resonance Raman spectroscopy // Electrochim. Acta. 1999. Vol. 44, № 12. P. 1887–1891.

185. Bobenko N.G. et al. Experimental and theoretical study of electronic structure of disordered MWCNTs // Carbon N. Y. Elsevier Ltd, 2019. Vol. 153. P. 40–51.

186. Korusenko P.M. et al. Comparative study of the structural features and electrochemical properties of nitrogen-containing multi-walled carbon nanotubes after ion-beam irradiation and hydrochloric acid treatment // Nanomaterials. 2021. Vol. 11, № 9.

187. Djara R. et al. Insights from the Physicochemical and Electrochemical Screening of the Potentiality of the Chemically Synthesized Polyaniline // J. Electrochem. Soc. 2020. Vol. 167, № 6. P. 066503.

188. Iurchenkova A.A., Kallio T., Fedorovskaya E.O. Relationships between polypyrrole synthesis conditions, its morphology and electronic structure with supercapacitor properties measured in electrolytes with different ions and pH values // Electrochim. Acta. Elsevier Ltd, 2021. Vol. 391. P. 138892.

189. Tan K.L. et al. The chemical nature of the nitrogens in polypyrrole and polyaniline: A comparative study by x-ray photoelectron spectroscopy // J. Chem. Phys. 1991. Vol. 94, № 8. P. 5382–5388.

190. Iurchenkova A.A. et al. A complex study of the dependence of the reduced graphite oxide electrochemical behavior on the annealing temperature and the type of electrolyte // Electrochim. Acta. Elsevier Ltd, 2021. Vol. 370. P. 137832.

191. Ahuja P. et al. Hierarchically Grown NiO-Decorated Polyaniline-Reduced Graphene Oxide Composite for Ultrafast Sunlight-Driven Photocatalysis // ACS Omega. 2018. Vol. 3, № 7. P. 7846–7855.

192. Tabačiarová J. et al. Study of polypyrrole aging by XPS, FTIR and conductivity measurements // Polym. Degrad. Stab. 2015. Vol. 120. P. 392–401.

193. Kumar S.N., Bouyssoux G., Gaillard F. Electronic and structural characterization of electrochemically synthesized conducting polyaniline from XPS studies // Surf. Interface Anal. 1990. Vol. 15, № 9. P. 531–536.

194. Golczak S. et al. Comparative XPS surface study of polyaniline thin films // Solid State Ionics. Elsevier B.V., 2008. Vol. 179, № 39. P. 2234–2239.

195. Smolin Y.Y., Soroush M., Lau K.K.S. Oxidative chemical vapor deposition of polyaniline thin films // Beilstein J. Nanotechnol. 2017. Vol. 8, № 1. P. 1266–1276.

196. Syugaev A. V. et al. Effect of sodium dodecyl sulfate and carbon particles/nanotubes on electrodeposition of polyaniline from oxalic acid solution // J. Solid State Electrochem. Journal of Solid State Electrochemistry, 2018. Vol. 22, № 3. P. 931–942.

197. Shi H.Y. et al. A Long-Cycle-Life Self-Doped Polyaniline Cathode for Rechargeable Aqueous Zinc Batteries // Angew. Chemie - Int. Ed. 2018. Vol. 57, № 50. P. 16359–16363.

198. Zheng X. et al. Multi-growth site graphene/polyaniline composites with highly enhanced specific capacitance and rate capability for supercapacitor application // Electrochim. Acta. Elsevier Ltd, 2018. Vol. 260. P. 504–513.

199. Mikheev G.M. et al. Photon-drag effect in single-walled carbon nanotube films // Nano Lett. 2012. Vol. 12, № 1. P. 77–83.

200. Stoller M.D., Ruoff R.S. Best practice methods for determining an electrode material's performance for ultracapacitors // Energy Environ. Sci. 2010. Vol. 3, № 9. P. 1294–1301.

201. Al-Farraj E.S. et al. Fabrication of hybrid nanocomposite derived from chitosan as efficient electrode materials for supercapacitor // Int. J. Biol. Macromol. Elsevier B.V., 2018. Vol. 120. P.

2271–2278.

202. Wu D., Yu C., Zhong W. Bioinspired strengthening and toughening of carbon nanotube@polyaniline/graphene film using electroactive biomass as glue for flexible supercapacitors with high rate performance and volumetric capacitance, and low-temperature tolerance // J. Mater. Chem. A. Royal Society of Chemistry, 2021. Vol. 9, № 34. P. 18356–18368.

203. Fu F. et al. Lamellar hierarchical lignin-derived porous carbon activating the capacitive property of polyaniline for high-performance supercapacitors // J. Colloid Interface Sci. Elsevier Inc., 2022. Vol. 617, № March. P. 694–703.

204. Hong X. et al. Potassium citrate-derived carbon nanosheets/carbon nanotubes/polyaniline ternary composite for supercapacitor electrodes // Electrochim. Acta. Elsevier Ltd, 2022. Vol. 403. P. 139571.

205. Liu S. et al. Polyaniline-decorated 3D carbon porous network with excellent electrolyte wettability and high energy density for supercapacitors // Compos. Commun. Elsevier Ltd, 2021. Vol. 24, № December 2020. P. 100610.

206. Dang A. et al. A novel hierarchically carbon foam templated carbon nanotubes/polyaniline electrode for efficient electrochemical supercapacitor // Fullerenes Nanotub. Carbon Nanostructures. Taylor & Francis, 2019. Vol. 27, № 5. P. 440–445.

207. Zhang H. et al. Long-term cycling stability of polyaniline on graphite electrodes used for supercapacitors // Electrochim. Acta. Elsevier Ltd, 2013. Vol. 105. P. 69–74.

208. Xiao F. et al. Scalable Synthesis of Freestanding Sandwich-structured Graphene/Polyaniline/Graphene Nanocomposite Paper for Flexible All-Solid-State Supercapacitor // Sci. Rep. 2015. Vol. 5. P. 1–8.

209. Ghasem Hosseini M., Shahryari E. A novel high-performance supercapacitor based on Chitosan/GO-MWCNT/PANI // J. Colloid Interface Sci. Elsevier Inc., 2017. Vol. 496. P. 371–381.

210. Tavakkoli M. et al. Single-Shell Carbon-Encapsulated Iron Nanoparticles: Synthesis and High Electrocatalytic Activity for Hydrogen Evolution Reaction // Angew. Chemie Int. Ed. 2015. Vol. 54, № 15. P. 4535–4538.

APPENDIX
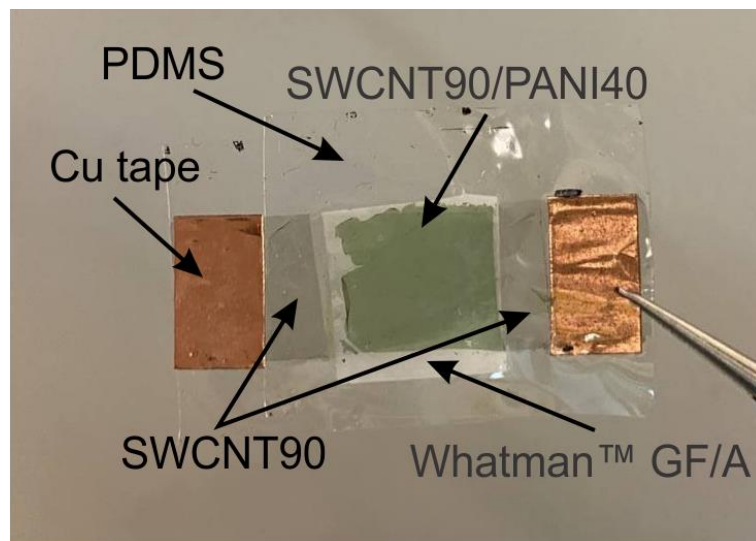
Figure A1. Flexible two-electrode cell based on SWCNT90/PANI40 composite material.
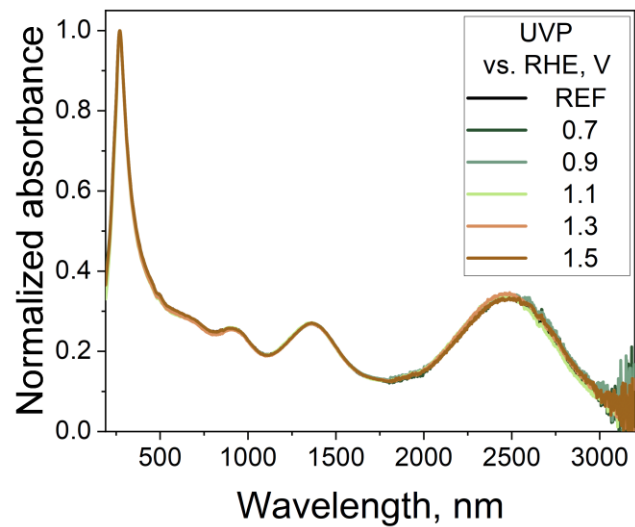
Figure A2. UV-vis-NIR spectra of *SWCNT-DH* samples used in the studies normalized to π-plasmon peak intensity.
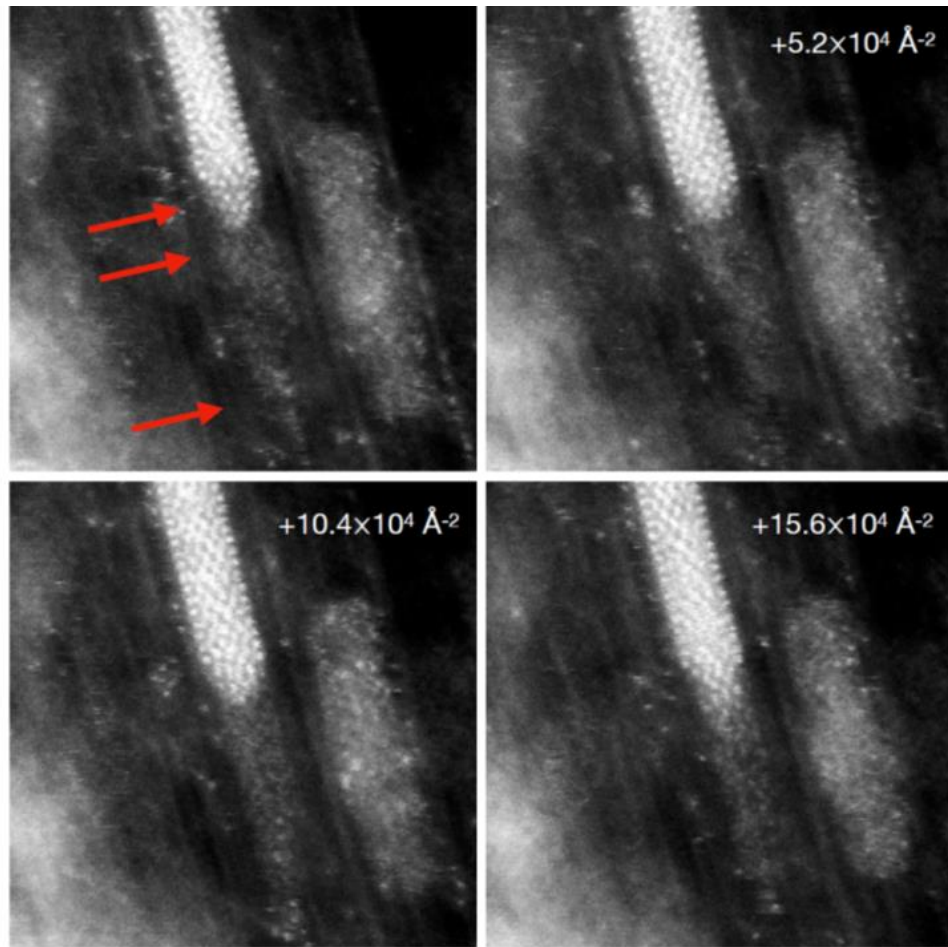
Figure A3. In situ diffusion of gold along the nanotube axis, the position pointed out by the arrows. The diffusion process is driven by the scanning electron probe, the dose equivalent per each acquired frame being $5.2 \cdot 10^4$ e⁻ Å⁻² at 25 pA probe current.
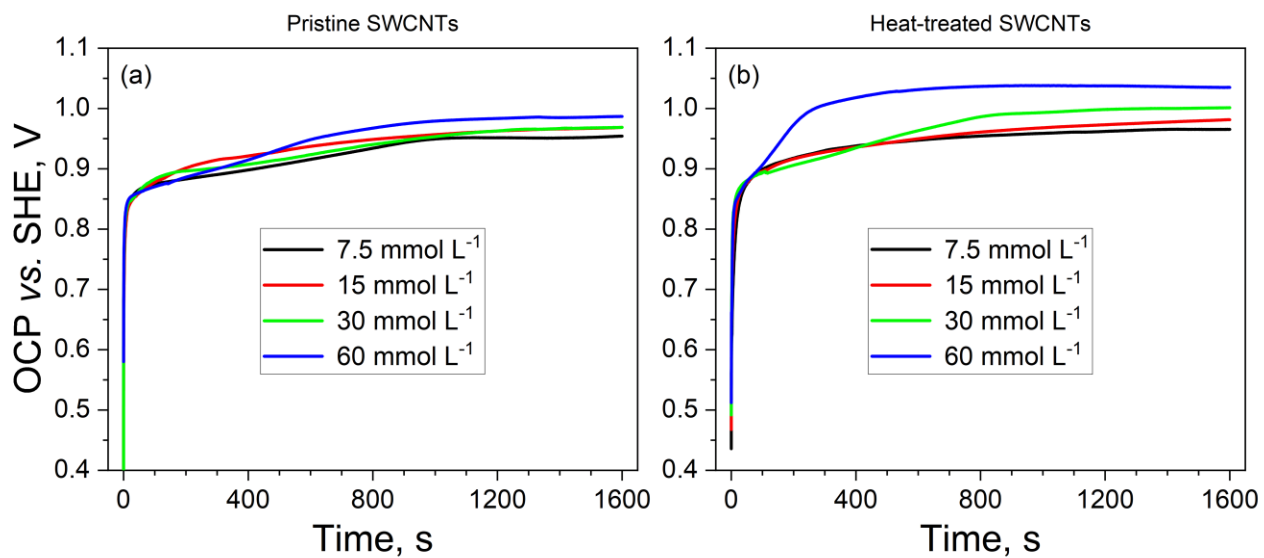
Figure A4. OCP transient for pristine (a) and heat-treated SWCNTs (b) recorded in HAuCl$_4$ solutions of 7.5, 15, 30 and 60 mmol L^{-1} concentrations.
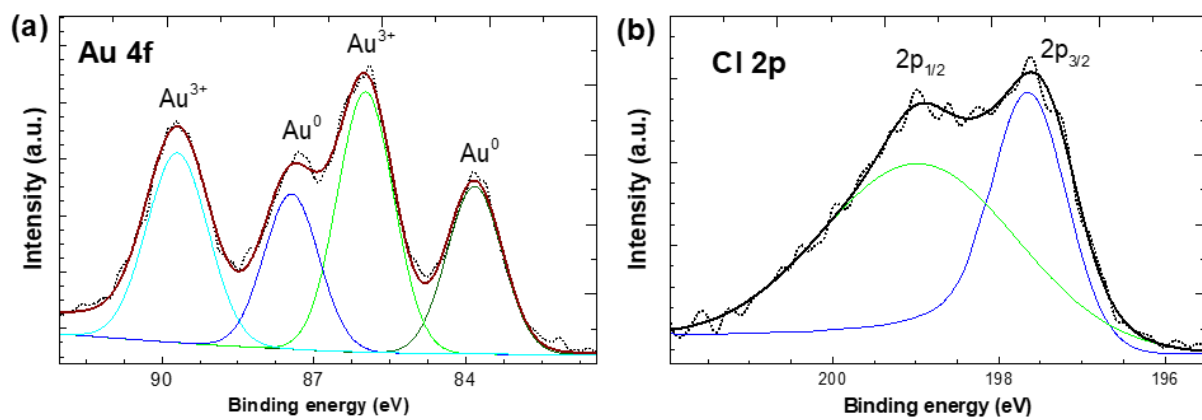
Figure A5. XPS spectra of fitted Au4f (a) and Cl2p (b) peaks.
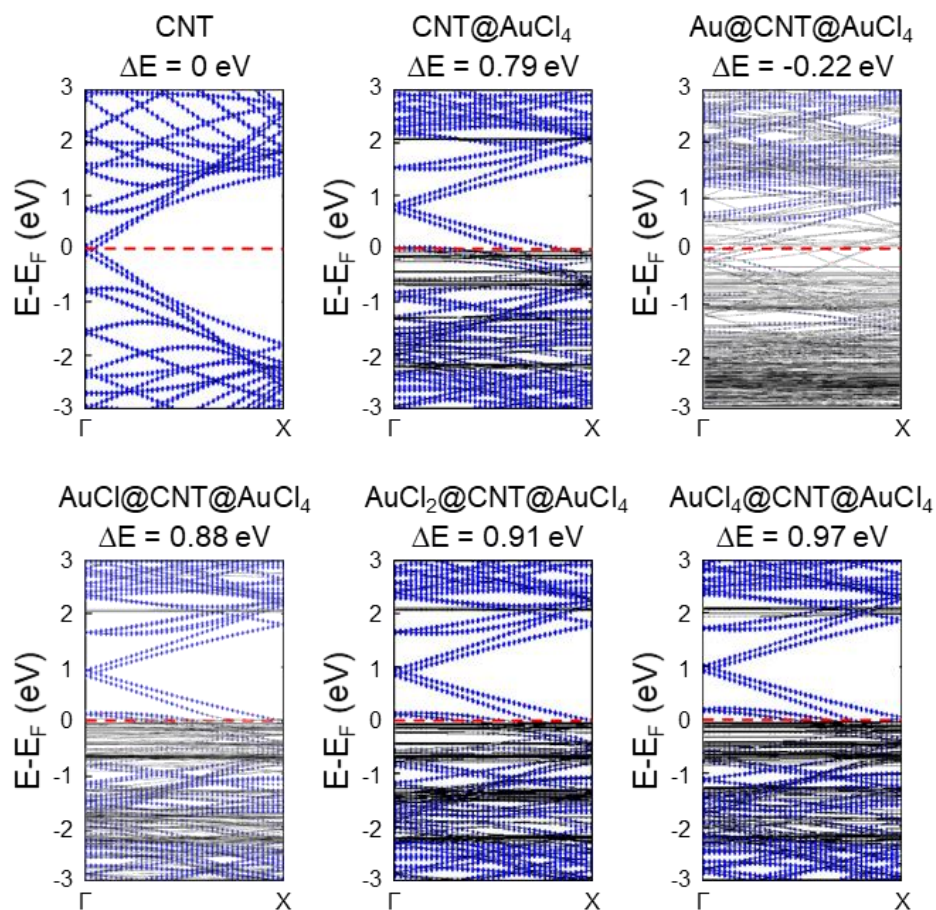
Figure A6. Band structures of pristine SWCNT(10,10), doped with [AuCl₄] from the outside, and doped from both the inside and outside with different [AuClₓ]-dopants as shown in Figure 8. Fermi level is indicated with a red dashed line, the blue dots correspond to contributions from carbon atoms.
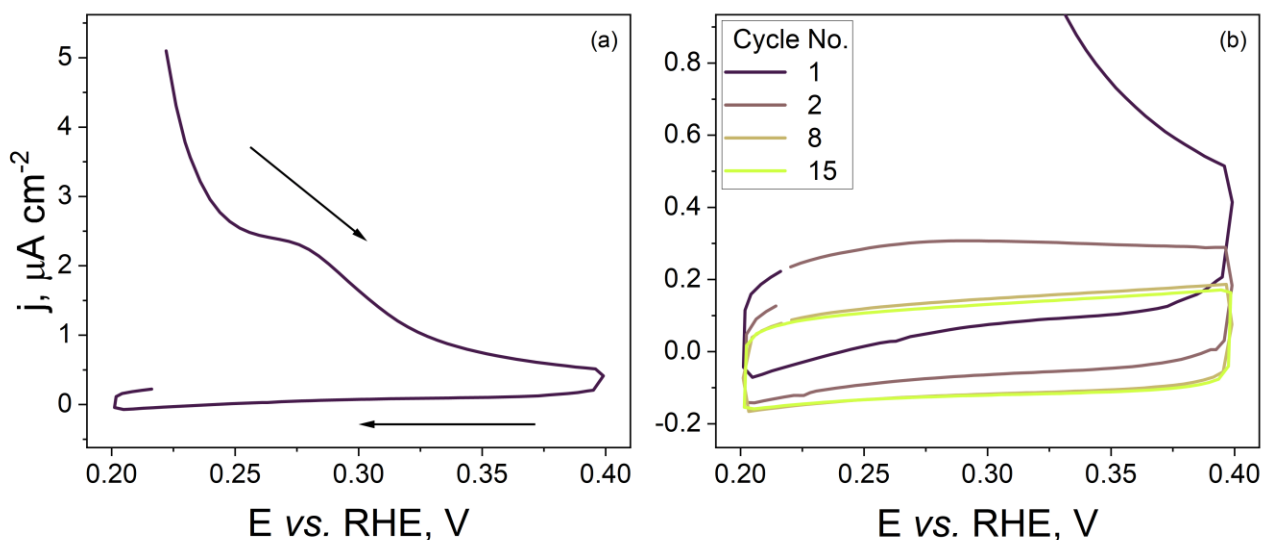
Figure A7. Typical cyclic voltammetry curves for the first SWCNT pre-treatment cycle (a) and comparison for pre-treatment cycle number 1, 2, 8 and 15 (b).
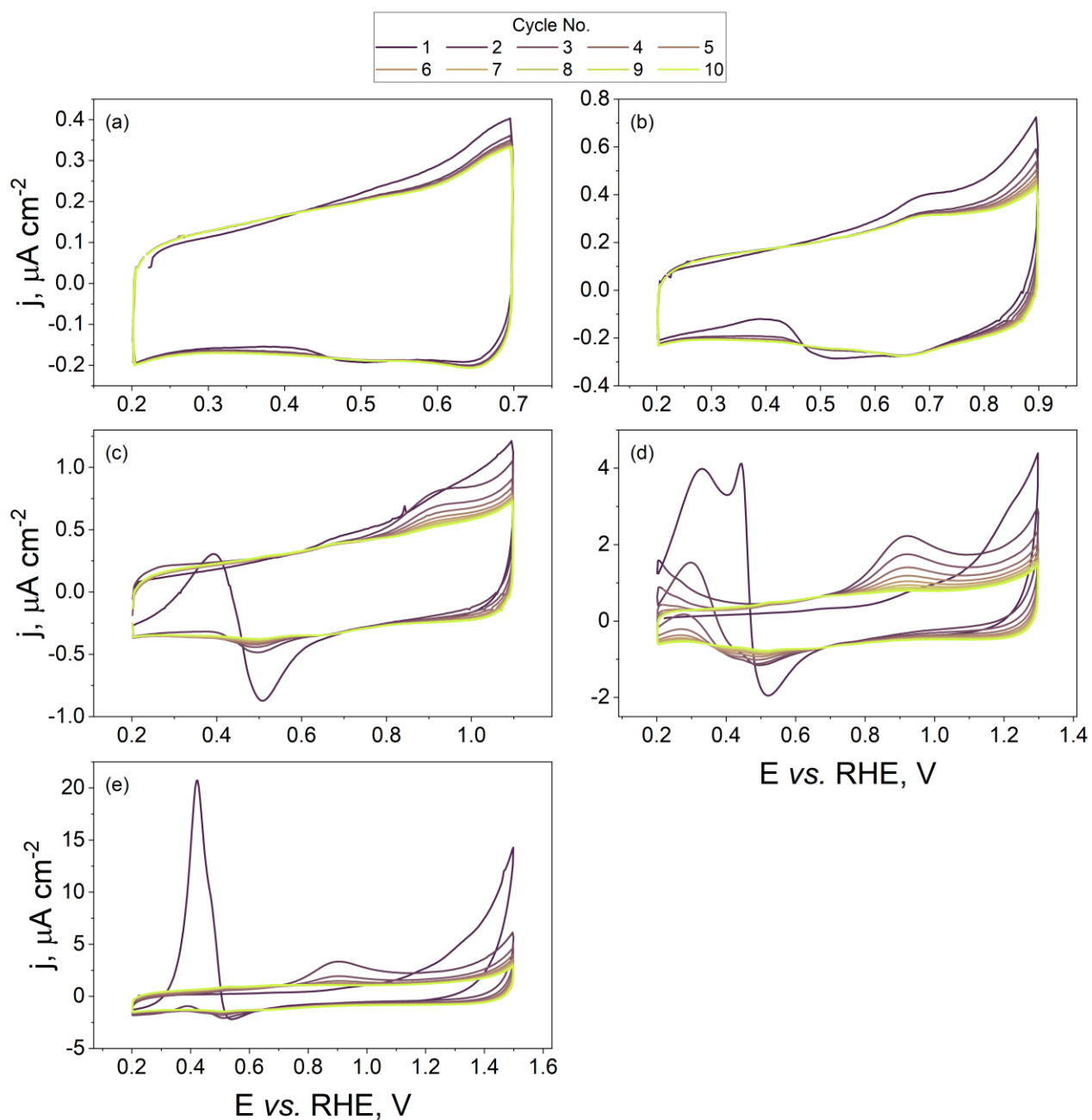
Figure A8. Cyclic voltammetry curves for small number of initial electrochemical treatment cycles (1, 3, 6 and 10) at UVPs from 0.7 to 1.5 V (a-e).
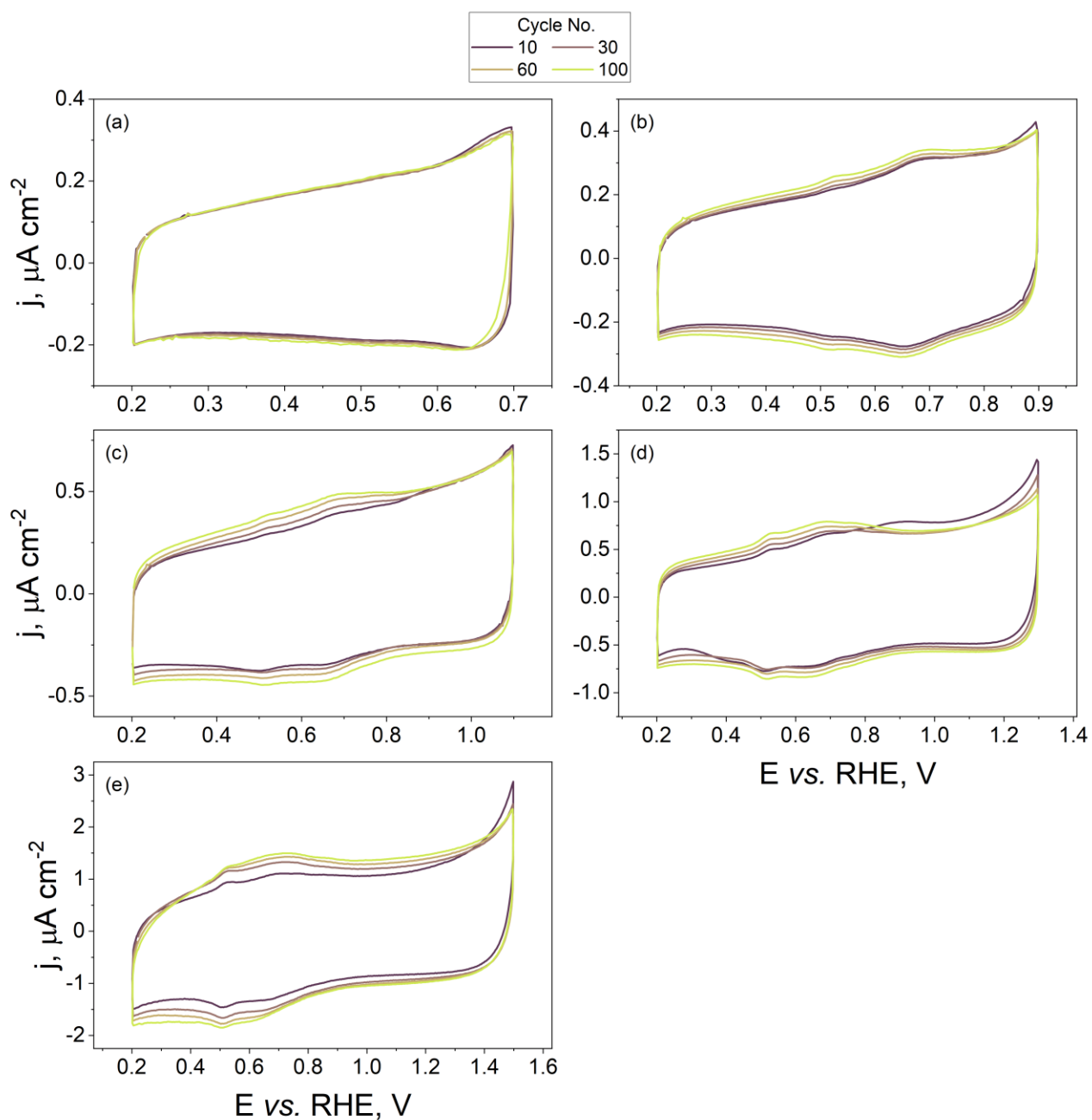
Figure A9. Cyclic voltammetry curves for longer electrochemical treatment (10, 30, 60 and 100 cycles) at UVPs from 0.7 to 1.5 V (a-e).
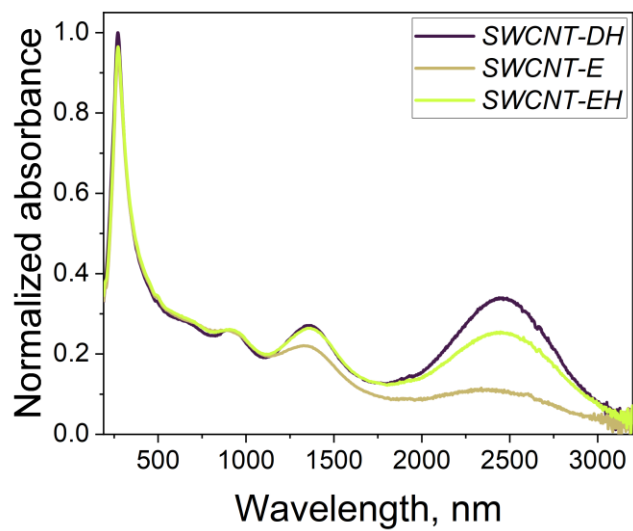
Figure A10. UV-vis-NIR spectra comparison of *SWCNT-DH*, electrochemically treated (*SWCNT-E*) and *SWCNT-EH* samples for film treated at UVP = 1.1 V.
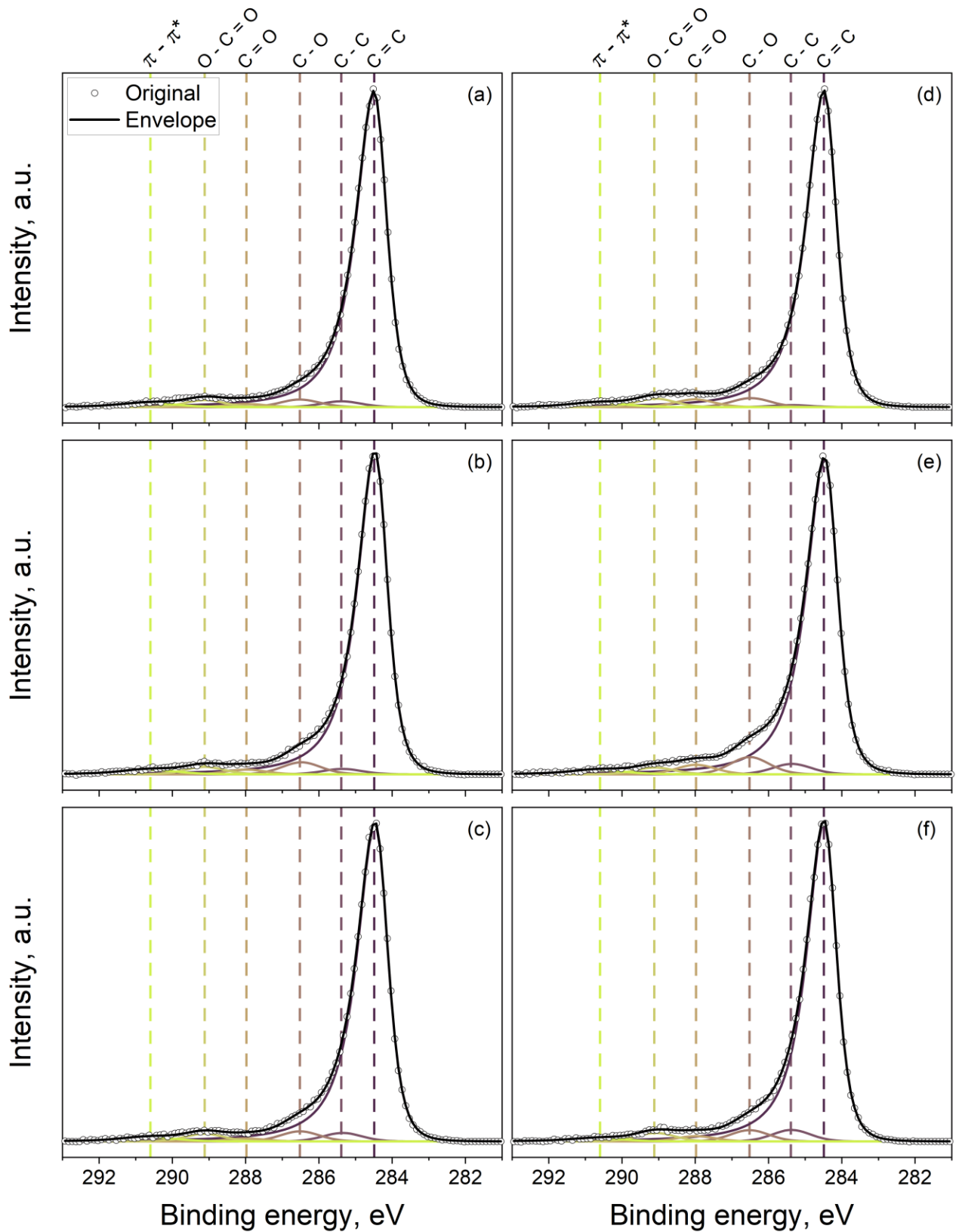
Figure A11. Fitted high-resolution C1s XPS spectra for reference *SWCNT-EH* film (a) in comparison with films treated at UVPs from 0.7 to 1.5 V (b-f).

Table A1. Total oxygen concentration from the survey XPS spectra and concentration of functional groups from C1s fitted spectra for *SWCNT-EH* films compared to the reference film.

UVP *vs.* RHE / V	Reference	0.7	0.9	1.1	1.3	1.5
at.% O	4.7	7.5	7.3	6.5	8.3	5.7
at.% C=C	91.3 (1.4)	89.5 (1.4)	89.8 (1.4)	90.1 (1.4)	86.2 (1.3)	88.1 (1.4)
at.% C-C	1.8 (1.2)	1.6 (1.0)	2.5 (0.9)	0.6 (0.8)	2.9 (1.0)	3.4 (1.0)
at.% C-O	2.3 (0.3)	3.6 (0.3)	3.0 (0.4)	2.7 (0.4)	4.8 (0.3)	3.3 (0.3)
at.% C=O	1.0 (0.3)	1.4 (0.3)	0.8 (0.4)	2.3 (0.2)	2.7 (0.2)	1.5 (0.2)
at.% O-C=O	2.1 (0.2)	2.2 (0.2)	2.2 (0.2)	2.6 (0.2)	1.9 (0.2)	2.5 (0.2)
at.% π-π* satellite	1.62 (0.4)	1.78 (0.5)	1.63 (0.5)	1.73 (0.3)	1.5 (0.4)	1.15 (0.4)
Residual STD	1.209	1.193	1.088	0.963	1.078	1.172
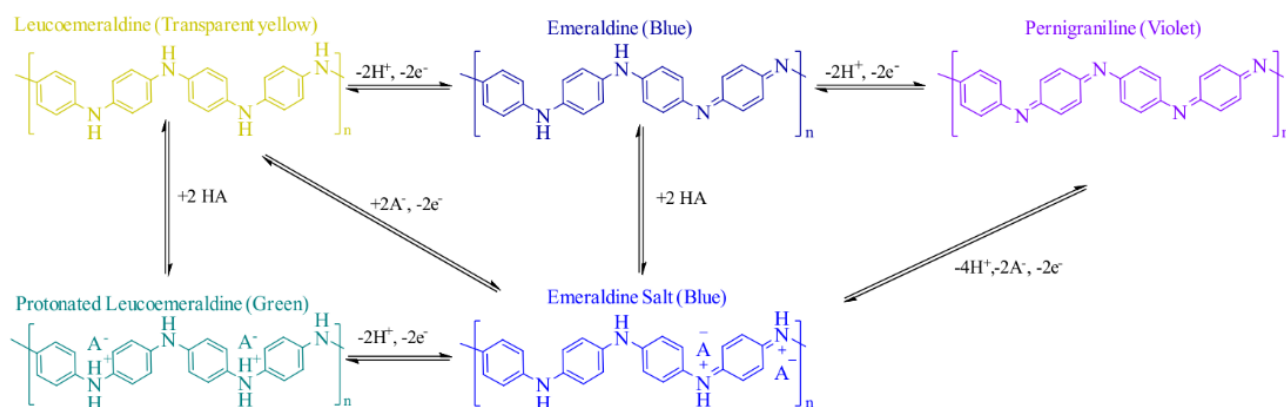
Figure A12. Redox transitions of PANI.
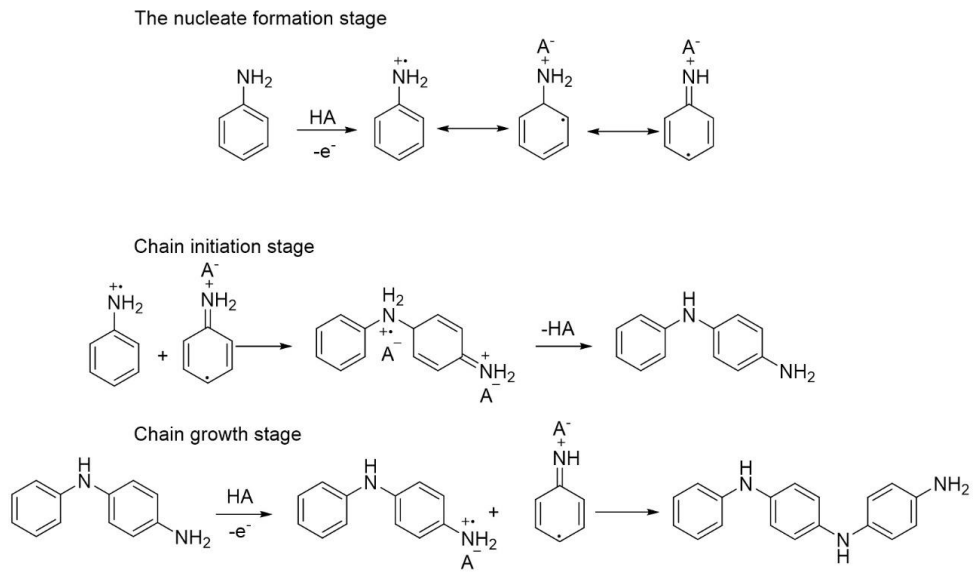
Figure A13. The mechanism of PANI electrochemical polymerization.
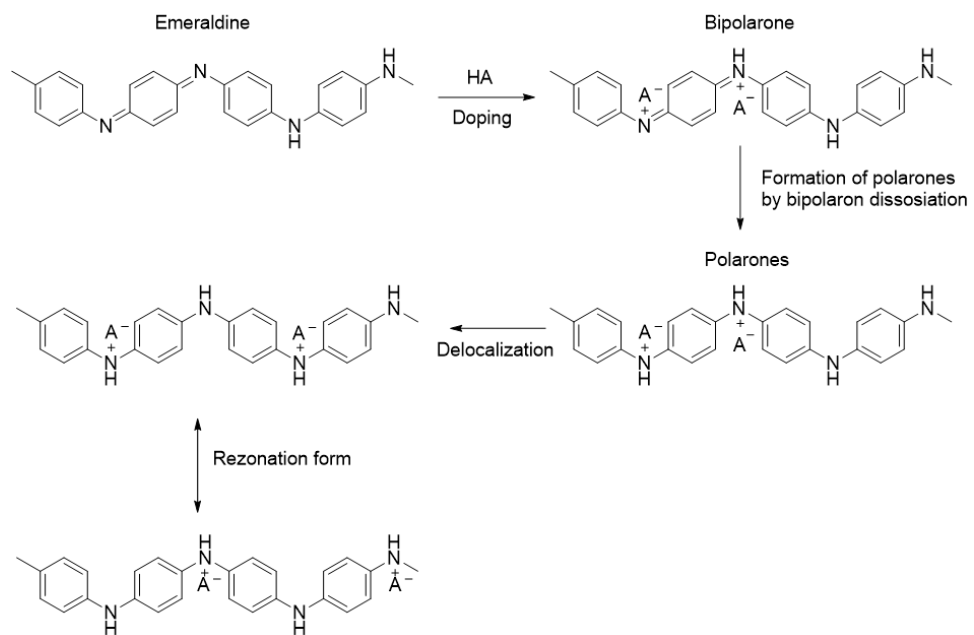
Figure A14. The PANI conductivity mechanism.
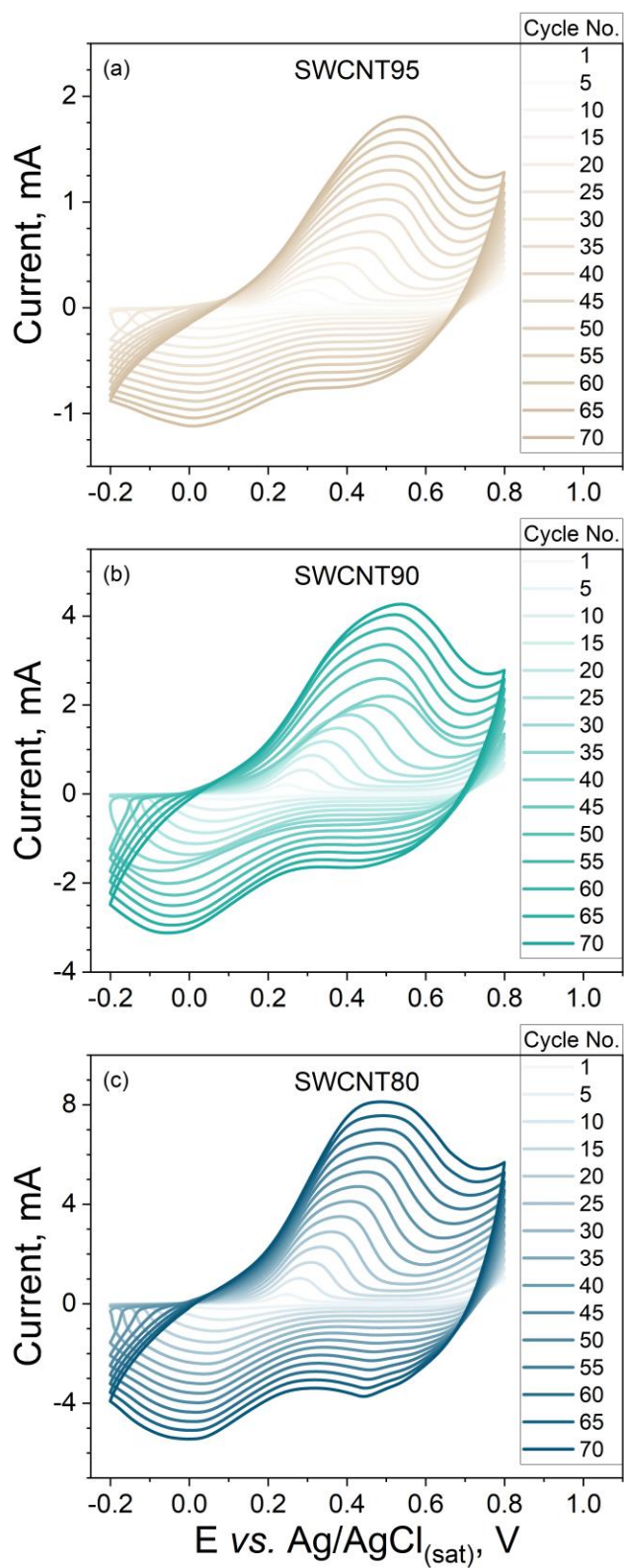
Figure A15. The behavior of CV curves during the electrochemical PANI polycondensation on free-standing films: SWCNT95 (a), SWCNT90 (b), and SWCNT80 (c).
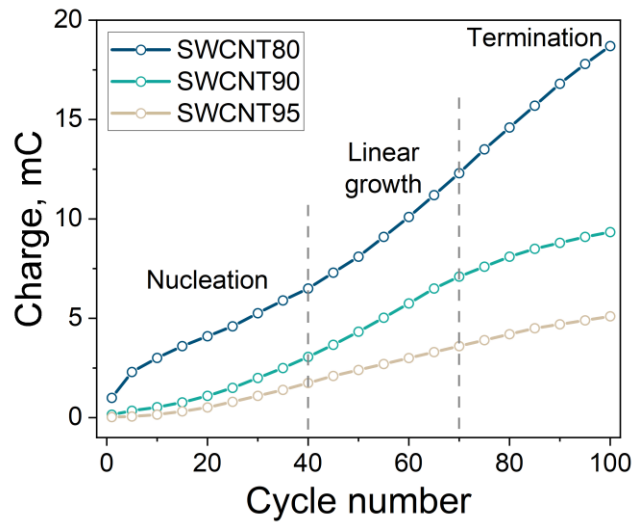
Figure A16. Charge consumed for PANI electrodeposition *versus* cycle number for SWCNT films with transmittance 80, 90, and 95 %.
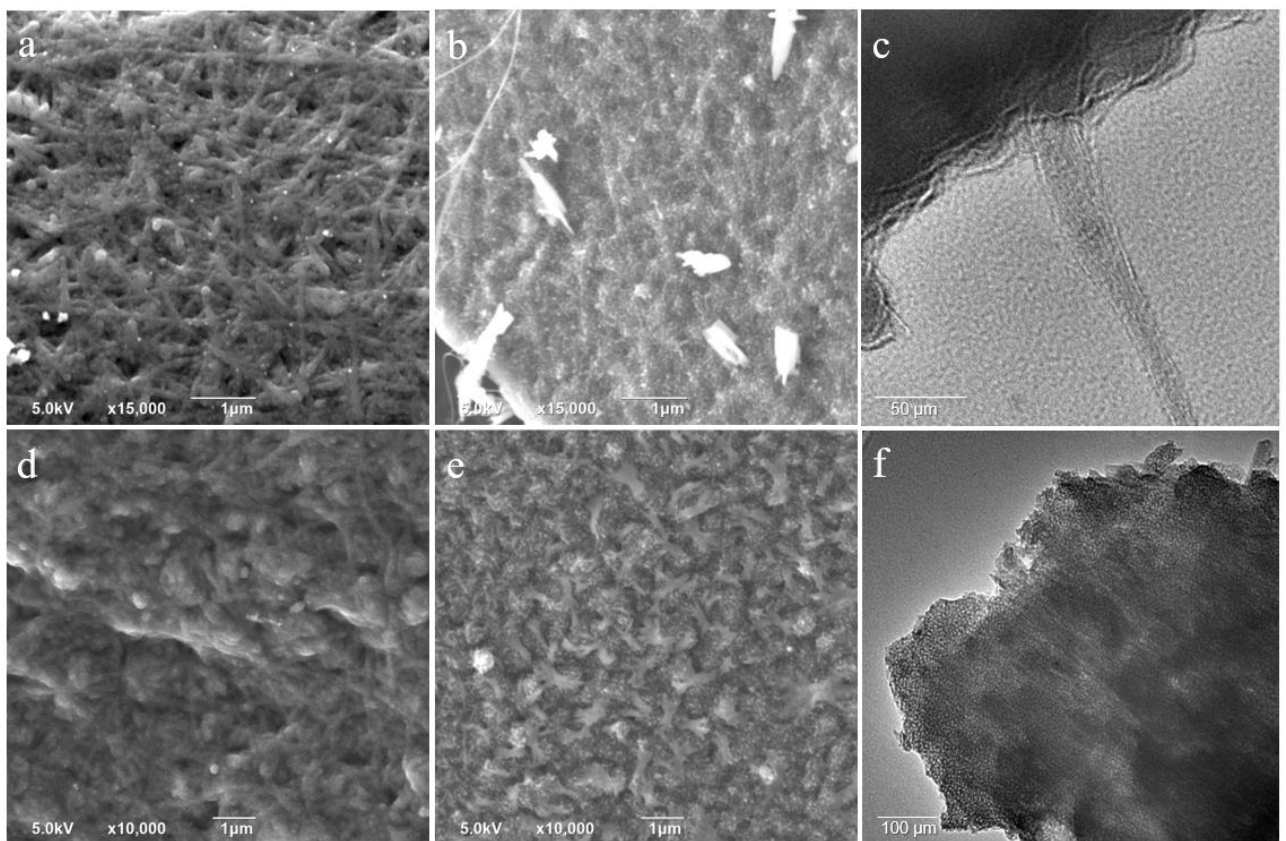
Figure A17. SEM images of SWCNT95/PANI40 (a), SWCNT95/PANI70 (b), SWCNT80/PANI40(d), SWCNT80/PANI70 (e); TEM images of SWCNT95/PANI40 (c,f).
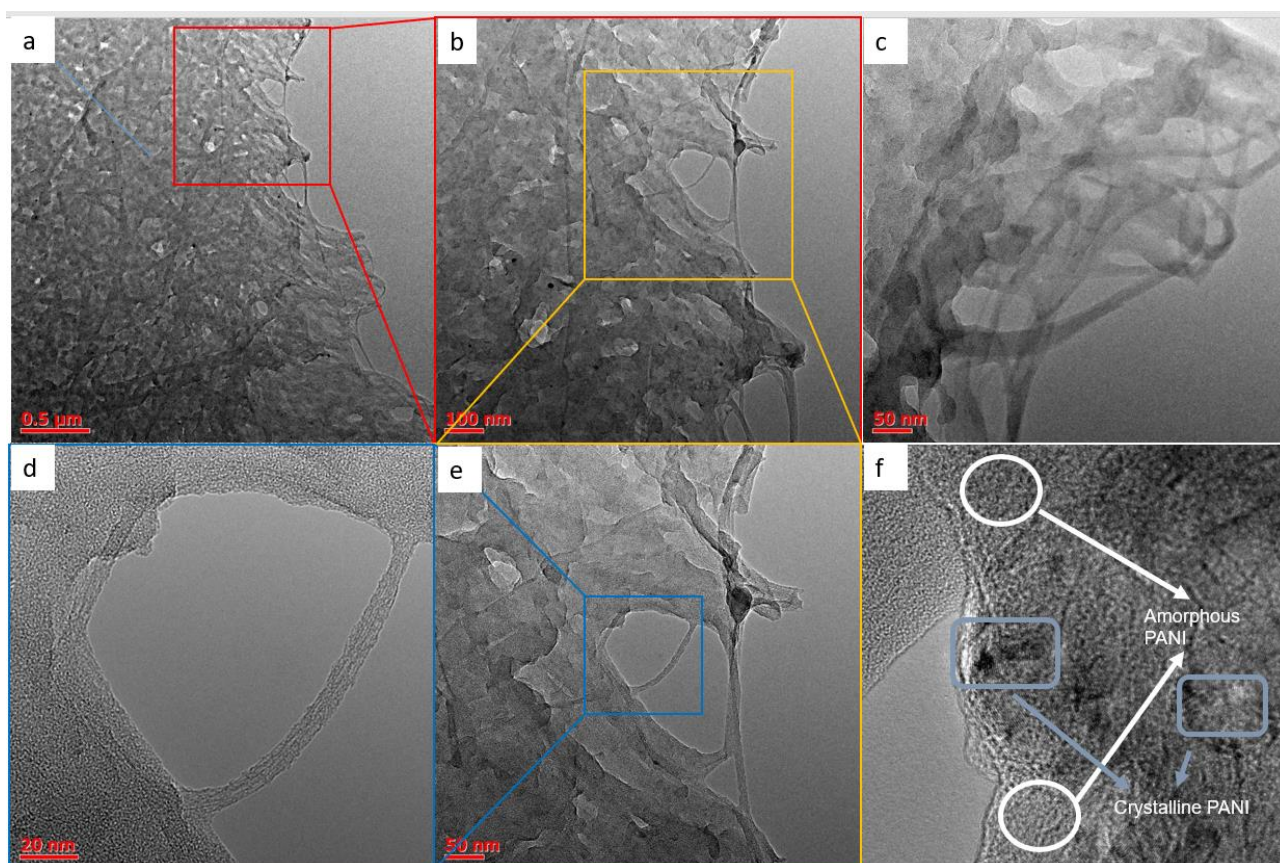
Figure A18. TEM images of SWCNT90/PANI40 composite films with different magnifications (a-e). TEM images of SWCNT95/PANI40 (f).

Table A2. Parameters of G and 2D Raman peaks.

Sample	SWCNT95	SWCNT95/ PANI70	SWCNT90/ PANI70	SWCNT80/ PANI70
Position of G-mode (cm^{-1})	1591	1586	1591	1588
Position of 2D-mode (cm^{-1})	2672	2676	2682	2676
2D-mode maximum intensity	0.11	0.11	0.11	0.10
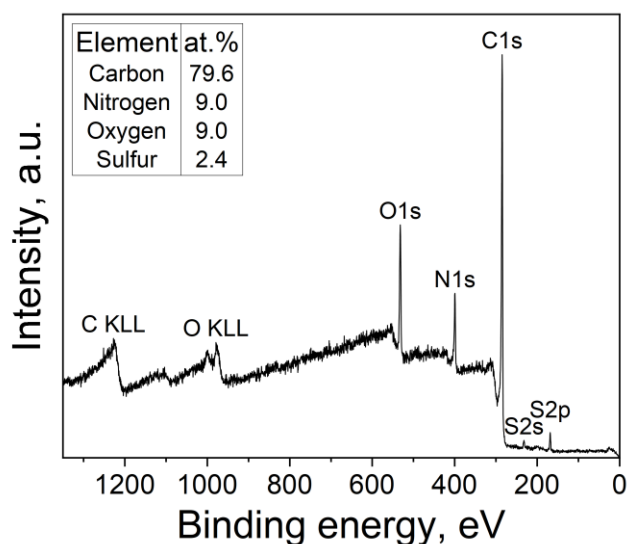
Figure A19. The survey XPS spectrum of the SWCNT95/PANI40 sample in BE range from 1350 to 0 eV.

Table A3. Concentration of different species in SWCNT95/PANI40 sample according to the XPS data.

Line	Species	BE, eV	Concentration, at.%
C1s	C=C	284.4	53.3
C1s	C-C/C-N	285.3	25.3
C1s	C-OH/C-NH$^+$	286.2	13.3
C1s	C=O/C=N	287.3	8.1
C1s	COOH/C=N$^+$	289.0	0.1
N1s	=N-	398.3	14.1
N1s	-NH-	399.5	64.4
N1s	-NH$^+$-	401.1	13.6
N1s	=NH$^+$-	402.7	7.9
O1s	C=O	531.1	39.5
O1s	COOH/SO$_4^{2-}$	532.4	37.4
O1s	C-OH	533.6	18.9
O1s	H$_2$O	535.2	4.2
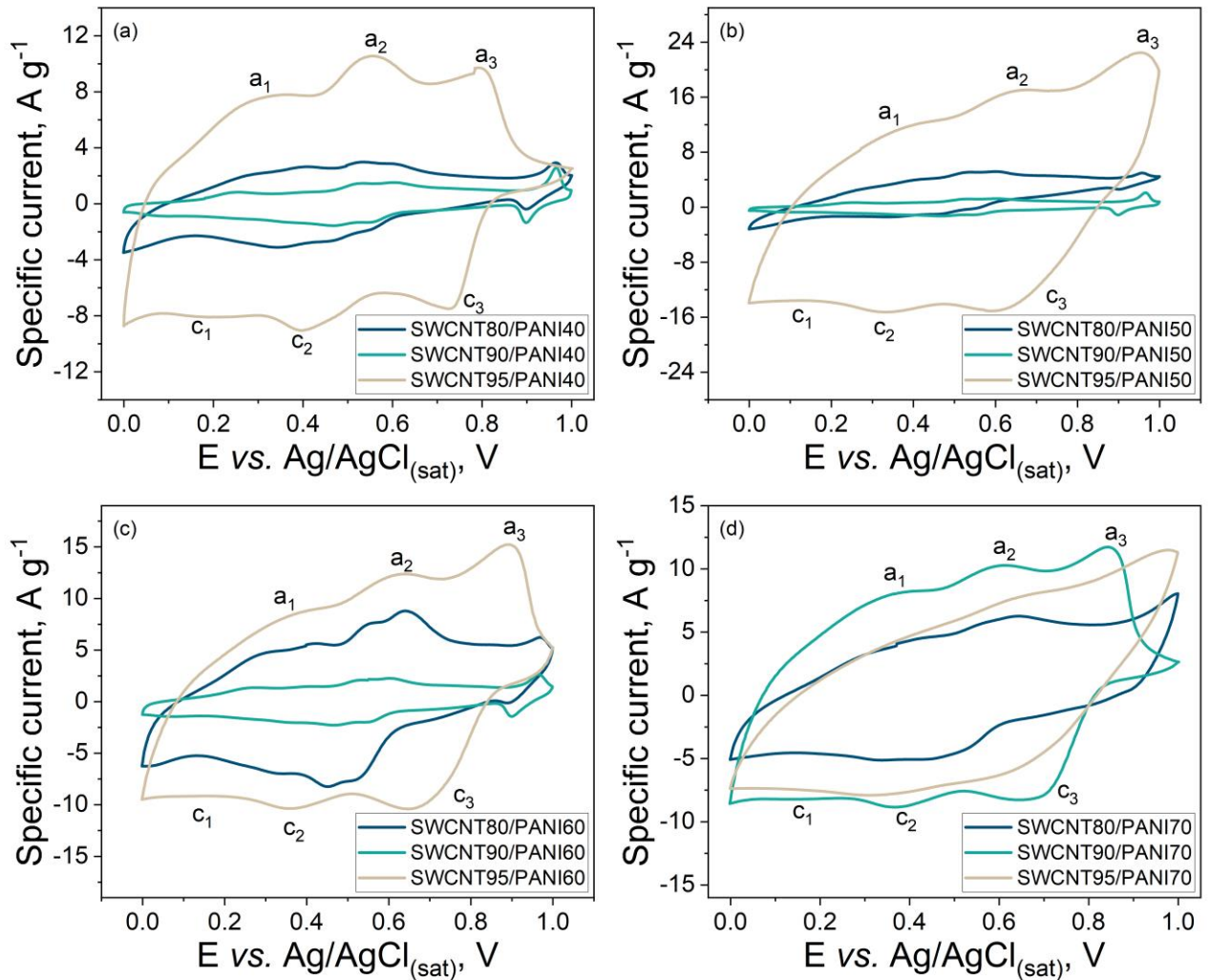
Figure A20. CV curves recorded at 20 mV s^{-1} of samples based on SWCNT95, SWCNT90, and SWCNT80 and PANI deposited during 40 (a), 50 (b), 60 (c) and 70 (d) polymerization cycles.
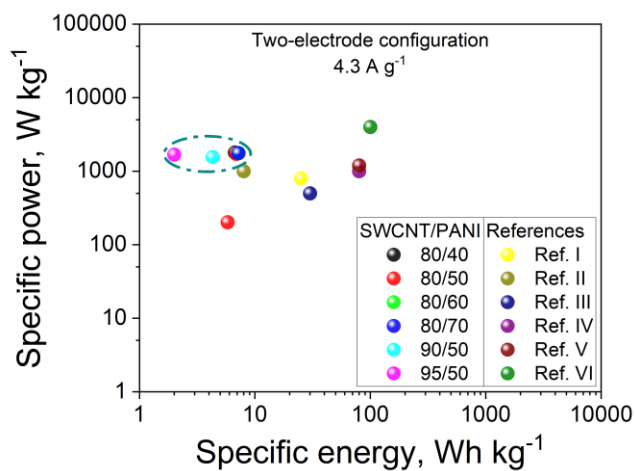
Figure A21. Ragone plot of SWCNT/PANI composites described in thesis in comparison with actual literature sources related to carbon nanostructures/PANI composites (Ref. I [186], Ref. II [187], Ref. III [188], Ref IV [189], Ref. V [190], Ref. VI [191]).
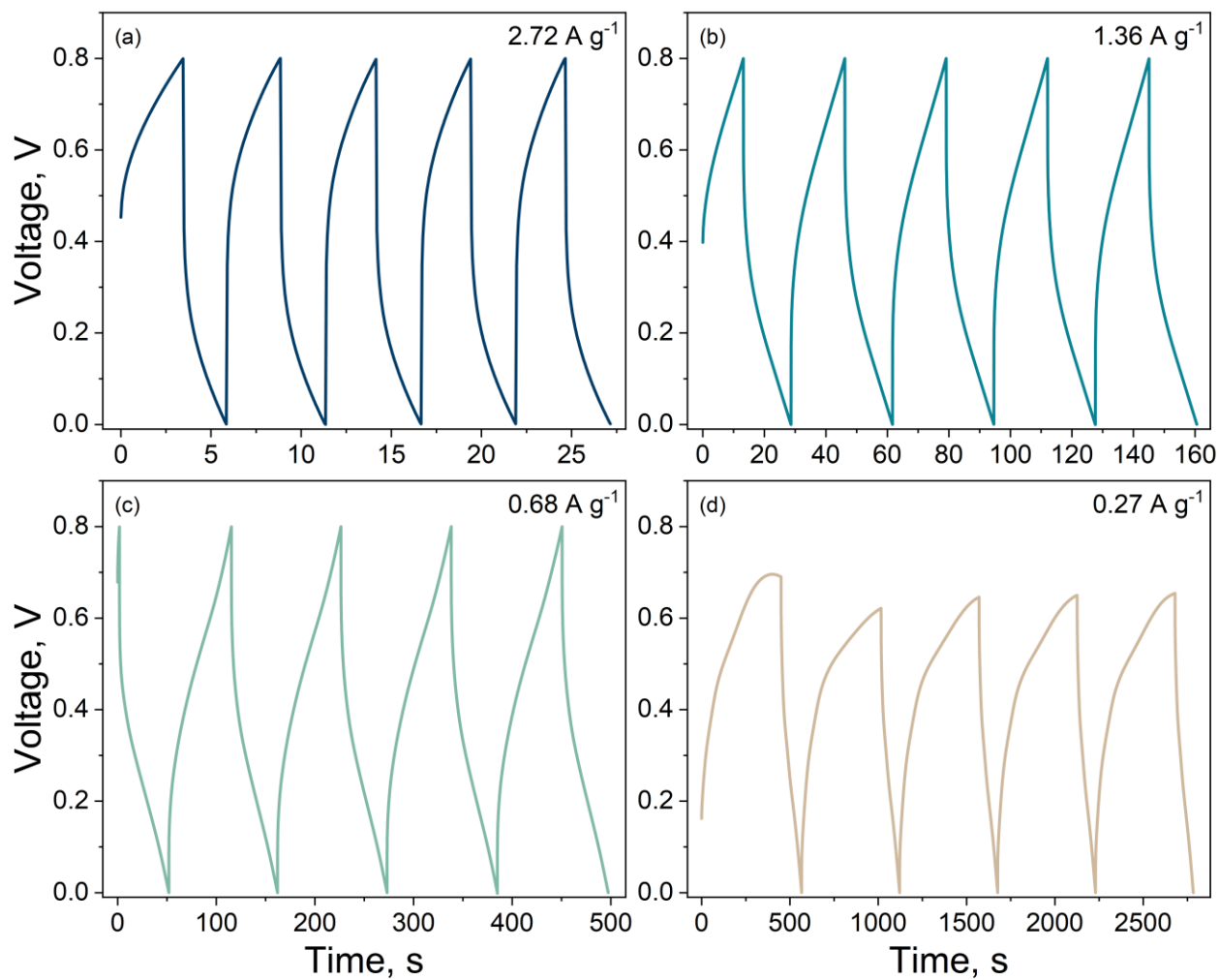
Figure A22. Galvanostatic charge-discharge curves for current densities of 0.27, 0.68, 1.36, and 2.72 A g^{-1} (a-d) for SWCNT90/PANI40 film.
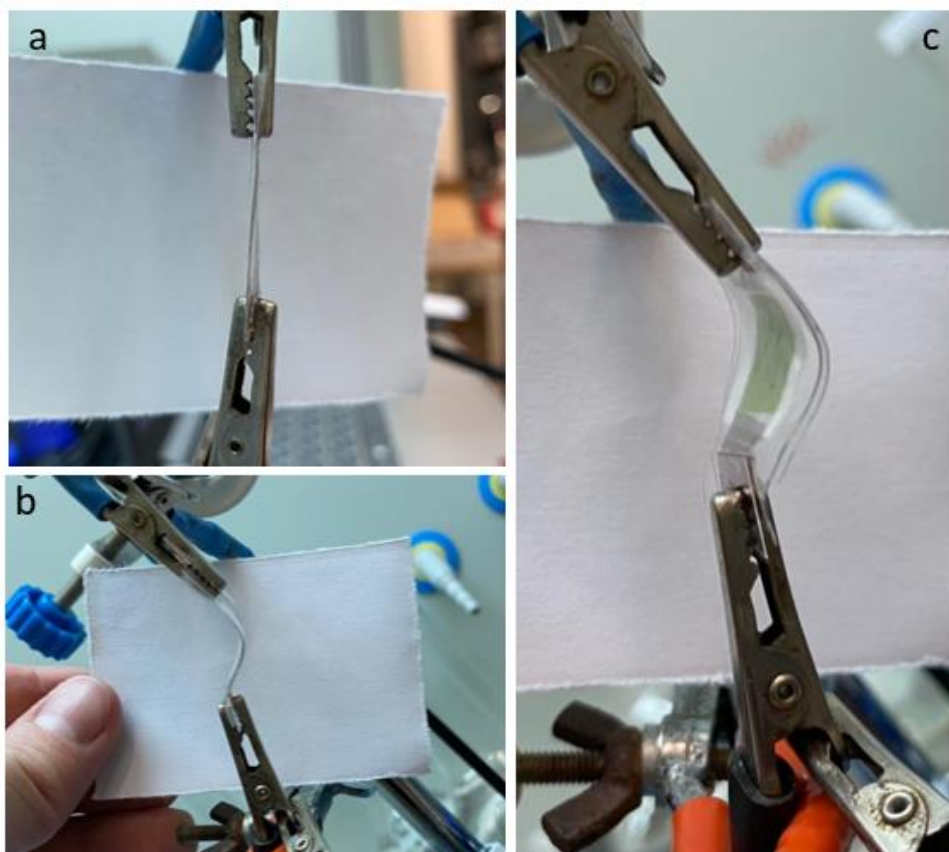
Figure A23. Photographs of flat (a) and bended (b,c) SC free-standing devices made of SWCNT90/PANI40 film.
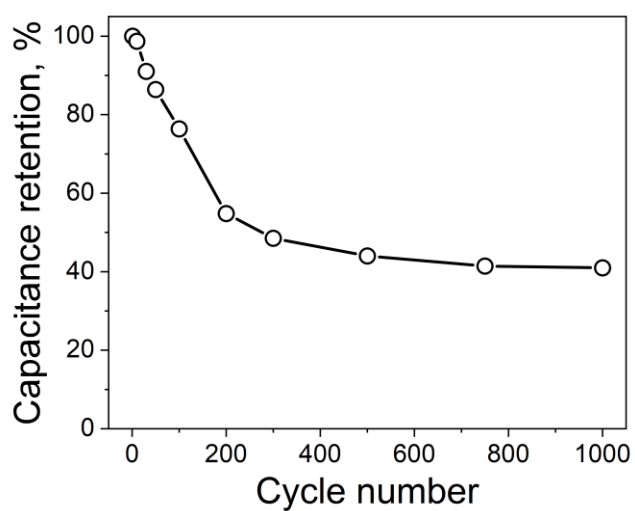
Figure A24. Capacitance retention *versus* the cycle number for the free-standing supercapacitor device measured at 0.34 A g^{-1} made of SWCNT90/PANI40 film.
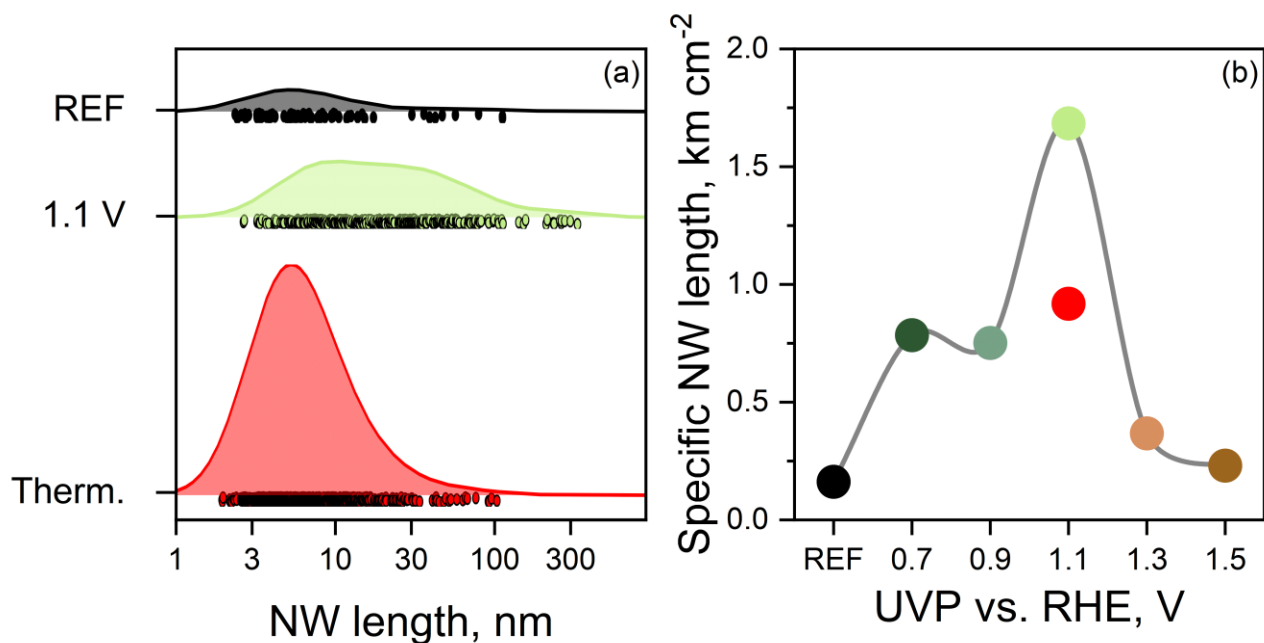
Figure A25. Length distribution of Au nanowires in reference sample, *SWCNT-EH* film treated at UVP = 1.1 V *vs*. RHE and thermally treated at 350 ºC film filled in the HAuCl$_4$ ethanol solution (a). Area under each curve is proportional to the number of NWs. The length of Au nanowires per a unit f-SWCNT film area prepared by means of the electrochemical treatment at different UVPs when compared to the thermally treated at 350 ºC film – red circle (b).

Table A4. Sheet resistance of the SWCNT films heat treated at different temperatures

Temperature, ºC	R_S / Ω sq^{-1}
100	71.0
150	79.3
200	80.4
250	94.2
300	110
350	135
400	143
450	172
500	193